2011

Fabrication of metal matrix composite by semi-solid powder processing

Yufeng Wu
Iowa State University

Fabrication of metal matrix composite by semi-solid powder processing

by

Yufeng Wu

A dissertation submitted to the graduate faculty

in partial fulfillment of the requirements for the degree of

DOCTOR OF PHILOSOPHY

Major: Mechanical Engineering

Program of Study Committee:

Gap-Yong Kim, Major Professor
Alan Russell
Iver Anderson
Pranav Shrotriya
Xinwei Wang

Iowa State University

Ames, Iowa

2011

TABLE OF CONTENTS

LIST OF FIGURES

LIST OF TABLES

ACKNOWLEDGEMENTS

I would like to take this opportunity to express my thanks to those who helped me with various aspects of conducting research and the writing of this thesis. First and foremost, thank Dr. Gap-Yong Kim for his guidance, patience and support throughout this research and the writing of this thesis. I would also like to thank my committee members, Dr. Alan Russell, Dr. Iver Anderson, Dr. Pranav Shrotriya and Dr. Xinwei Wang, for their efforts and contribution to this work. Finally, I would thank my parents, Zhengzhong Wu and Baolian Cheng, and my wife Jing Ren for their invaluable supports and help in my study in the United State.

ABSTRACT

Various metal matrix composites (MMCs) are widely used in the automotive, aerospace and electrical industries due to their capability and flexibility in improving the mechanical, thermal and electrical properties of a component. However, current manufacturing technologies may suffer from insufficient process stability and reliability and inadequate economic efficiency and may not be able to satisfy the increasing demands placed on MMCs. Semi-solid powder processing (SPP), a technology that combines traditional powder metallurgy and semi-solid forming methods, has potential to produce MMCs with low cost and high efficiency. In this work, the analytical study and experimental investigation of SPP on the fabrication of MMCs were explored. An analytical model was developed to understand the deformation mechanism of the powder compact in the semi-solid state. The densification behavior of the Al6061 and SiC powder mixtures was investigated with different liquid fractions and SiC volume fractions. The limits of SPP were analyzed in terms of reinforcement phase loading and its impact on the composite microstructure. To explore adoption of new materials, carbon nanotube (CNT) was investigated as a reinforcing material in aluminum matrix using SPP. The process was successfully modeled for the mono-phase powder (Al6061) compaction and the density and density distribution were predicted. The deformation mechanism at low and high liquid fractions was discussed. In addition, the compaction behavior of the ceramic-metal powder mixture was understood, and the SiC loading limit was identified by parametric study. For the fabrication of CNT reinforced Al6061 composite, the mechanical alloying of Al6061-CNT powders was first investigated. A mathematical model was developed to predict the CNT length change during the

mechanical alloying process. The effects of mechanical alloying time and processing temperature during SPP were studied on the mechanical, microstructural and compositional properties of the Al6061-CNT composites. A shear lag model was applied to predict the mechanical property (hardness) of the composite. This work demonstrated the promising potential of SPP in the fabrication of particle/fiber (nanotube) reinforced MMCs.

CHAPTER 1 INTRODUCTION

1.1 Motivation

Metal matrix composites (MMCs) have been widely studied because of their ability to enhance the mechanical, thermal or electrical properties of the matrix by incorporating micro or nano size fibers or particles. MMCs have been applied in various fields for their flexibility in property customization based on specific requirements (Kaczmar, Pietrzak et al. 2000). As shown in Table 1.1, by adding various fiber and particle materials, the strength of the composites can be significantly improved (by up to 420%) compared with the matrix phase. The specific strength and specific modulus of the materials can reach a value of 650 MPa/(Mg/m^3) and 120 GPa/(Mg/m^3), respectively.

Table 1.1: Ultimate tensile strength and elastic modulus of selected light MMCs (Lindroos and Talvitie 1995)

Matrix	Reinforcement	Vol. fraction (%)	Tensile strength			Elastic modulus		
			Value (MPa)	Improvement (%)	Specific strength (MPa/(Mg/m^3))	Value (GPa)	Improvement (%)	Specific modulus (GPa/(Mg/m^3))
Al2024	boron fiber	60	1500	275	644	270	269	116
Al2024	Al_2O_3	50	450	12.5	135	175	139	53
Al6061	SiC fiber	50	1500	383	507	205	197	69
Al6061	SiC whisker	15	480	55	173	100	45	36
Al6061	SiC particle	15	370	19	133	100	45	36
Mg	graphite fiber	40	560	124	230	230	411	115
Mg	SiC fiber	50	1300	420	520	230	411	93

The MMC market has been growing significantly in the past 10 years because of the extraordinary properties of the MMCs. Fig. 1.1 shows the global consumption of MMCs in different market sectors. An annual consumption growth rate of 5.9% is expected till 2013, and the total consumption will increase from 4.4 million kilograms in 2008 to 5.9 million in 2013. The increasing growth of the MMC market requires sophisticated and advanced technologies to mass produce MMCs at a low cost and with high efficiency. Although there have been more development activities in MMC, insufficient process stability and reliability, and inadequate economic efficiency still challenge the MMC manufacturing industry (Kainer 2006).

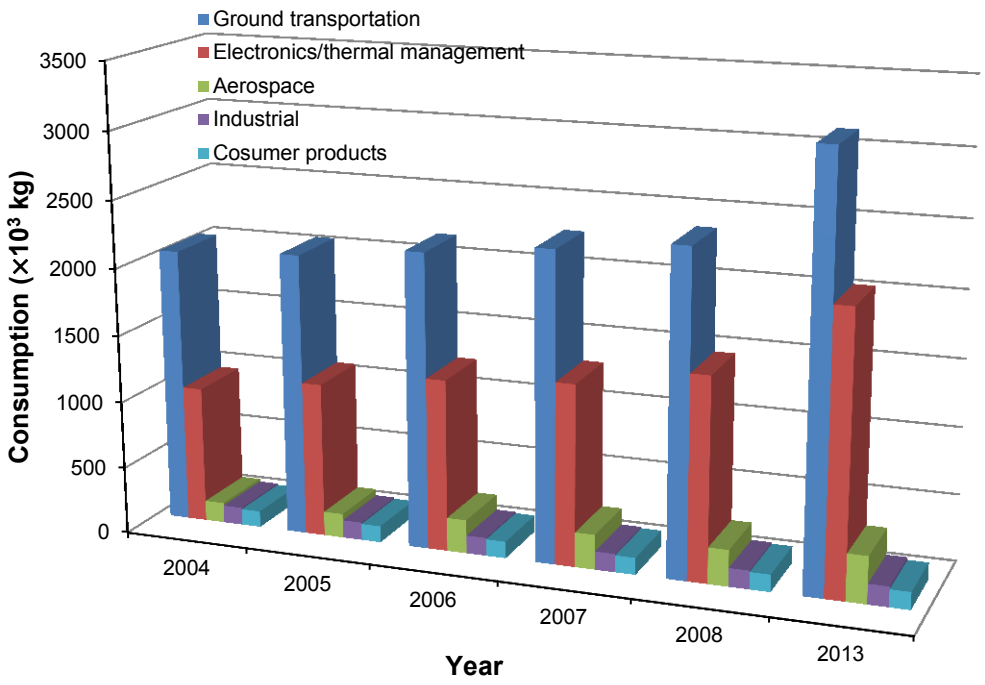

Fig. 1.1: Global MMC consumption outlook by application/segment (2004-2013) (BCC_Research 2009)

Various technologies were developed for the fabrication of MMCs. As shown in Fig. 1.2, the processing technology can be divided into three categories, i.e. solid-state processing, liquid-state processing and vapor-state processing (Montanari, Tagliaferri et al. 2009). Processing MMCs in the liquid-state (i.e. casting and infiltration) was able to achieve high relative density. However, post-processing may be required to reduce distortion and shrinkage of the parts. Solid-state processing of MMC, including HIPing and sintering, is typically capable of controlling composition accurately. Nevertheless, they often suffer from sintering imbalance and require a complex green compact (Kawasaki 1997). One of the major advantages of vapor-state processing is to achieve a well-bonded fiber/particle-matrix interface without generating reactions that may degrade

the final composite properties (Montanari, Tagliaferri et al. 2009). However, deposition processes such as physical vapor deposition process may have drawbacks including low efficiency and high initial cost.

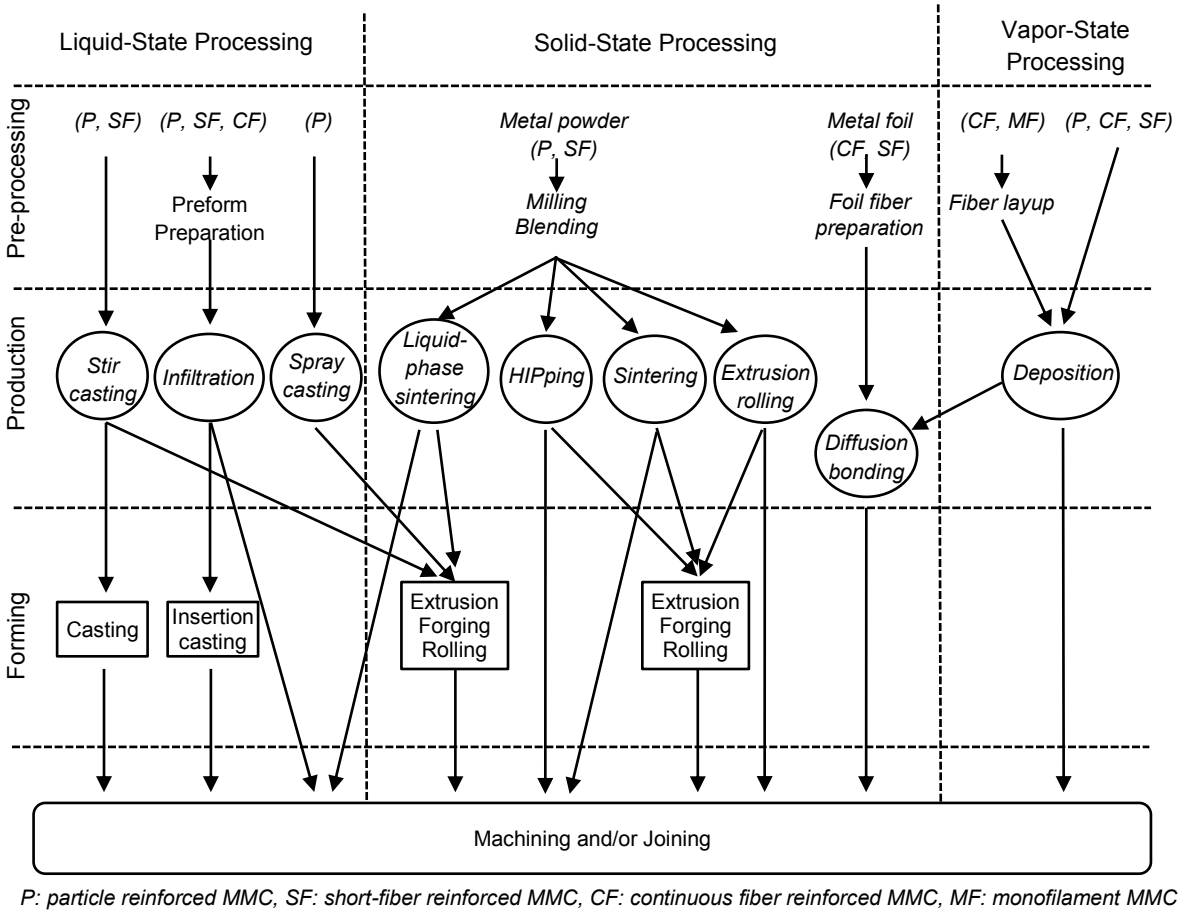

Fig. 1.2: Schematic overview of the production processes about MMCs (Montanari, Tagliaferri et al. 2009)

Semi-solid powder processing (SPP) expands the semi-solid forming by replacing the bulk material with powdered material, which enables exploitation of powder metallurgy. A schematic of the process is depicted in Fig. 1.3. SPP may be divided into

four steps: powder mixing, pre-compaction at room temperature, material heat-up and densification. SPP has been applied to produce net-shaped MMCs with low reinforcement loading (< 30%). Previous work has demonstrated the potential to produce composites with high efficiency, low cost and good compositional control with promising microstructure. However, no work was found in the theoretical analysis of the SPP technology, the compaction behavior of metal-ceramic powder mixtures during SPP, the fabrication of high ceramic loading reinforcement MMCs, or the nanotube reinforced MMCs.

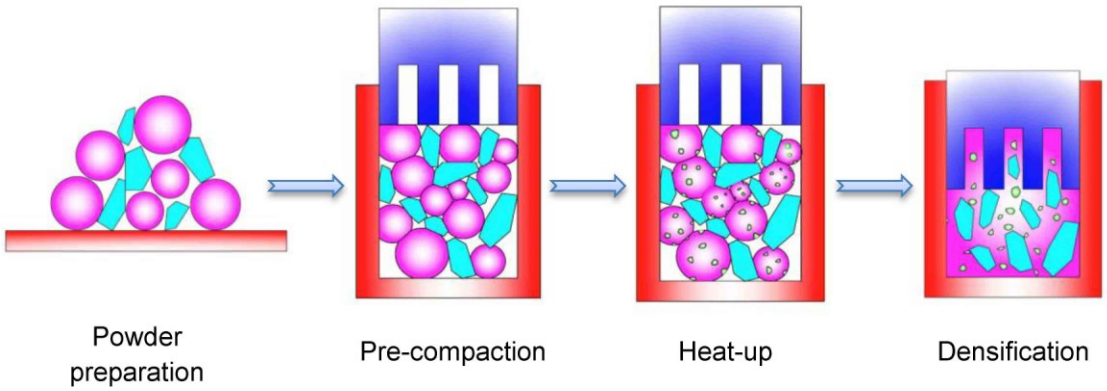

Fig. 1.3: Schematics of the SPP

The motivation of this research is to lay a fundamental foundation that will allow a scientific approach needed to characterize the SPP and to assess the potentials of SPP in the fabrication of MMCs. Most importantly, limited research was found in the analytical study of the powder compaction with the presence of liquid-phase and the knowledge gap in understanding the theoretical basis of SPP needs to be filled. The compaction behavior of the metal-ceramic powder mixture in the semi-solid state is not understood. In

addition, the reinforcement loading limit of the MMCs during SPP was not fully studied and understanding the potential of SPP on the fabrication of particle reinforced MMC are necessary. For the fabrication of CNT reinforced MMCs, the dispersing of CNT was challenging, and mechanical alloying was usually utilized to disperse the CNTs. However, mechanical alloying of metal-CNT powders was not well understood, and the damage to CNT during mechanical alloying needs to be revealed. Also, parametric study of SPP on the metal-CNT composite should be carried out to obtain a more sophisticated knowledge of SPP on the fabrication of nanotube reinforced MMCs.

1.2 Research Framework and Objectives

The goal of the study is to theoretically understand the deformation mechanism of the powders in the semi-solid state and to investigate the potential of SPP in the fabrication of particle and fiber (nanotube) reinforced MMCs. The objectives of the study are the following:

1) Understand the compaction behavior of powder compacts in the semi-solid state and model the relative density and stress responses during SPP for closed-die compaction.

2) Understand the densification behavior of metal and ceramic powder mixtures in the semi-solid state and reveal the effects of ceramic volume fraction and metal liquid fraction on the compaction behavior.

3) Study the compaction behavior of SiC reinforced metal composite, identify the particle reinforcement loading limit during SPP, and examine the mechanical properties and compositions of the high volume SiC loading reinforced Al6061 composite processed by SPP with different parameters.

4) Analyze the mechanical alloying of Al6061-CNT powders for a better understanding of the change of CNT morphology during mechanical alloying.

5) Understand the effects of processing temperature and mechanical alloying time during SPP on the microstructural, mechanical and compositional properties of the Al6061-CNT composite.

The following subsections describe the framework of the work to achieve the above objectives.

1.2.1 Compaction Behavior of Al6061 powder in the semi-solid state

This section focused on the theoretical analysis of the SPP during the closed-die compaction process. Shima-Oyane's model was utilized to study the pressure-density response and density distribution in the compaction direction during the semi-solid powder compaction process with relative low liquid fraction. Al6061 powder compaction experiments in the semi-solid region were carried out to verify the modeling results. The effects of temperature (liquid fraction) on the modeling parameters were analyzed.

1.2.2 Densification behavior of Al6061 and SiC binary powder mixture in semi-solid state

The densification behavior of metal-ceramic powder mixtures in the semi-solid state was examined. Al6061 with various SiC volume fractions (0%-60%) were compacted at temperatures from the 550°C to 660°C (Al6061 liquid fraction from 0%-100%). The effects of SiC volume fraction and Al6061 liquid fraction on the densification behavior of the powder mixture were experimentally investigated.

1.2.3 Fabrication of Al6061 Composite with High SiC Particle Loading by Semi-solid Powder Processing

Aluminum alloys reinforced with SiC particles have been studied extensively for their favorable properties in structural and thermal applications. However, there has been only limited research that investigated the loading limit of a reinforcement phase of a MMC. The objective of this study is to assess the potential of SPP in the fabrication of high volume fraction SiC particle reinforced Al6061 composite. The compaction and synthesis mechanism of the composite by SPP was discussed based on reinforcement phase compaction behavior and processing parameters.

1.2.4 Mechanical Alloying of Carbon Nanotube and Al6061 Powder for Metal-CNT Composite

Mechanical alloying was widely used to break down the CNT agglomeration in the metal matrix. However, due to the challenges in collecting the CNTs for measurement, quantitative study of CNT breakage has been difficult. In this study, the CNTs with Al6061 powder were mechanically alloyed with high energy milling

equipment. A mathematical model has been developed to predict the overall CNT length distribution during mechanical alloying process. The effects of mechanical alloying time and welding and fracturing of particles on the CNT length and length distribution were investigated.

1.2.5 Carbon Nanotube Reinforced Aluminum Composite Fabricated by Semi-solid Powder Processing

High strength and high thermal and electronic conductivities make CNTs an ideal reinforcing material for composites. In metal composites, however, progress has been rather slow due primarily to challenges associated with CNT dispersion and high temperature processing used in the synthesis of metal composites. In this section, carbon nanotube (CNT) reinforced aluminum alloy 6061 (Al6061) composite was synthesized by SPP. The effects of the processing temperature and mechanical alloying time on the powder morphology, microstructure, hardness, flexural strength, fracture surface and composition of the Al6061-CNT composite were investigated. A modified shear lag model was used to predict the strength of Al6061-CNT at different mechanical alloying times.

1.3 Dissertation Organization

The remainder of the dissertation is divided into six chapters. In Chapter 2, the compaction behavior of powders in the semi-solid state was analyzed, and the pressure-density relationship was modeled by extending application of the Shima-Oyane model to

the semi-solid region with relatively low liquid fraction. In Chapter 3, densification behavior of Al6061 and SiC powder mixtures was studied. The effects of SiC fraction and Al6061 liquid fraction on the compaction behavior were examined. In Chapter 4, high volume SiC fraction reinforced Al6061 composites were fabricated by SPP. The effects of process parameters on the microstructures, properties and the compositions of the samples were examined. Chapter 5 investigated the mechanical alloying of Al6061-CNT powders. A mathematical model was developed to predict the CNT length during mechanical alloying. In Chapter 6, CNT reinforced Al6061 composites were processed with SPP. The effects of fabrication temperature and mechanical alloying time on the composite were investigated. A summary and contribution of this research are presented in Chapter 7.

CHAPTER 2 COMPACTION BEHAVIOR OF AL6061 POWDER IN THE SEMI-SOLID STATE

2.1 Introduction

SPP attracted increasing interest in recent years. SPP combines the benefits of the semi-solid forming and powder metallurgy (Steinhoff, Weidig et al. 2004; Kim, Koc et al. 2007; Kim, Ni et al. 2007). The flexibility of powder mixing enables the advantage of tailoring material properties (El Wakil 1992; Luo, Cheng et al. 2006; Wu, Kim et al. 2010b). The unique rheological characteristic of the semi-solid flow allows forming of complex geometries. It can also minimize post processing steps typically required in powder metallurgy routes. SPP has been successfully applied to process alloy systems materials such as Al-Ti (Yasue 2000; Wen 2001) and Al-Mg (Young and Clyne 1986a), and composite materials including Al-SiC (Guo and Tsao 2000; Chen, Yang et al. 2004; Wu 2009; Wu, Kim et al. 2010a; Wu, Kim et al. 2011) and Al-CNT. Wu et al. also demonstrated the effectiveness of semi-solid powder flow in filling the micro-scale features for applications in micro/meso-manufacturing (Wu, Kim et al. 2010b).

Models have been developed to predict and understand the semi-solid forming and powder compaction behavior. In general, the modeling approach for semi-solid forming depends on the amount of solid phrase (or liquid-phase) in the material (Ilegbusi and Ballas 1999). When the solid fraction is high (>0.5), the material can be regarded as a viscoplastic porous medium saturated with liquid (Kim, Koc et al. 2007). At low solid

fractions, the solid-phase is treated as agglomerations within the slurry system, and the degree of agglomeration is then characterized by processing parameters like strain rate (Kumar, Martin et al. 1994). Several constitutive models have been developed to describe the powder compaction process. Drucker-Prager cap model is one of the most widely used powder compaction models (Brewin, Coube et al. 2008). It is capable of providing an accurate prediction of density evolution based on the pressure applied (Lee and Kim 2002). To determine the parameters used in this model, however, a triaxial compression experiment is needed, which is delicate and requires sophisticated equipment (Brewin, Coube et al. 2008). The parameters are likely to vary as the temperature is changed. Fleck et al. (Fleck, Kuhn et al. 1992) developed a yield criterion for powder compacts based on the particle strain energy analysis, enabling a direct application of the constitutive equations to the powder compaction process. Shima and Oyane (Shima and Oyane 1976) proposed a plastic yield criterion for porous metallic structures fabricated by sintering process. This model has been successfully applied to both room (Shima and Oyane 1976) and high temperature powder compaction processes (Kang and Jung 1999). However, no study was found that extended into the semi-solid regime to model the powder compaction in the presence of liquid-phase.

In this work, the compaction behavior of metallic alloy powder in the semi-solid regime was studied. Al6061 powders were compacted at temperatures below the melting point (550°C) to the semi-solid range (645°C). The SPP was modeled for the first time by extending Shima-Oyane's model for the prediction of compaction of powders with a relatively low liquid fraction (<20 vol%). The effects of temperature (or liquid fraction)

on the parameters of the model were analyzed. The friction between the powder and die was modeled to obtain a more accurate density prediction. The predicted overall density and density distribution along the compaction direction were compared with experimental findings. In addition, the powder compaction behavior with high liquid fraction (>20 vol%) was experimentally analyzed.

2.2 Theoretical Background

An alloy material in semi-solid state is partly melted between the solidus and liquidus temperatures, and therefore, both solid and liquid-phases coexist. The liquid fraction of the material can be defined as:

$$f_l = \frac{V_l}{V_s + V_l} \tag{2.1}$$

where, V_s and V_l are the volumes of the solid and liquid-phases, respectively. The relative density of the powder compact D, i.e. the volume fraction of the semi-solid mixture in the powder compact, can be obtained through:

$$D = \frac{V_s + V_l}{V_s + V_l + V_p} \tag{2.2}$$

where, V_p is the volume of the pores.

As shown in Fig. 2.1, the semi-solid skeleton (i.e., the matrix phase consisting of solid and liquid-phases) and the pores bear the load applied to the powder compact. The

stress component acting on the powder compact can be separated into the semi-solid skeleton and the pores as:

$$\sigma_{ij}{}^{t} = \sigma_{ij}{}^{ssm} + \sigma_{ij}{}^{pore} \tag{2.3}$$

where, $\sigma_{ij}{}^{t}$ is the total stress applied to the semi-solid powder compact; $\sigma_{ij}{}^{ssm}$ and $\sigma_{ij}{}^{pore}$ are the stress components taken by the semi-solid skeleton and the pores, respectively;

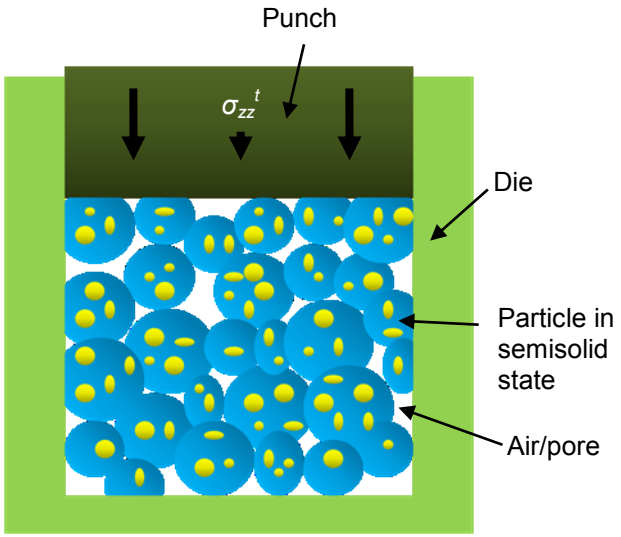

Fig. 2.1: Schematics of die compaction of semi-solid powder

Although the Shima-Oyane yield model was originally developed for sintered porous metals, the model has shown to predict the behavior of cold powder compaction process quite successfully (Lee and Kim 2002). At elevated temperatures when the material becomes mushy, the porous material will behave very similar to interlinked porous structure for which the original Shima-Oyane yield criterion was developed. If the liquid-phase is uniformly distributed in the semi-solid skeleton during the compaction process, one can apply the Shima-Oyane model to evaluate the stress required to deform

the semi-solid matrix phase. In this study, Shima-Oyane yield behavior was assumed for temperatures between 550°C and 630°C as the following:

$$f'\sigma_{eq} = \left\{ \frac{[(\sigma_1 - \sigma_2)^2 + (\sigma_2 - \sigma_3)^2 + (\sigma_1 - \sigma_3)^2]}{2} + \left(\frac{\sigma_m}{f}\right)^2 \right\}^{\frac{1}{2}} \quad (2.4)$$

where, σ_{eq} is the equivalent stress applied to the full density matrix phase; σ_1, σ_2, and σ_3 are principal stresses of the powder compact; and f' is the ratio of the apparent stress applied to the powder compact and the equivalent stress applied to the full density matrix phase. Thus, the yield behavior of the porous compact is described by Eqn. (2.4), i.e. by deviatoric and hydrostatic stresses applied to the porous compact, and parameters f' and f, which are related to the relative density of the porous compact. $\sigma_m=(\sigma_1+\sigma_2+\sigma_3)/3$; $f'=D^n$; $f=1/[a(1-D)^b]$. n, a and b are material-related parameters. The yield surface of Shima-Oyane model is shown in Fig. 2.2. It is observed that when the relative density of the powder compact approaches the full density, the Shima-Oyane yield criterion becomes equivalent to the von-Mises yield criterion.

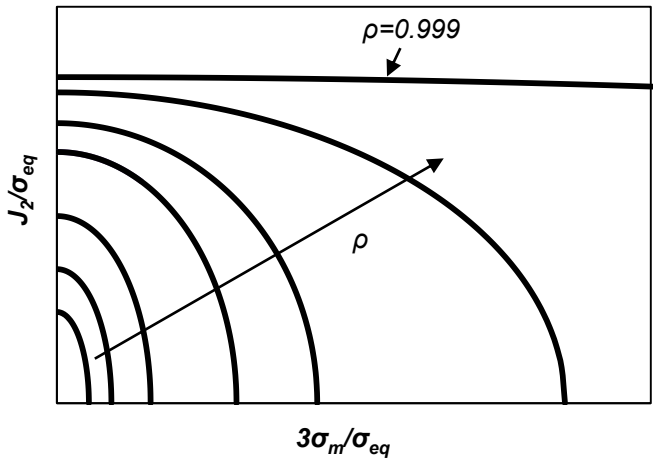

Fig. 2.2: Yield surface of Shima-Oyane model

For the condition of closed-die forging, Shima and Oyane (Shima and Oyane 1976) further simplified Eqn. (2.4) to:

$$\sigma_{zz}^{ssm}/\sigma_{eq} = D^n \left(f^2 + \frac{4}{9}\right)^{\frac{1}{2}} \tag{2.5}$$

$$\dot{\varepsilon_{eq}} = \left[D\left(\frac{4}{9} + f^2\right)\right]^{\frac{1}{2}} \dot{D} \tag{2.6}$$

where σ_{zz}^{ssm} is the normal stress acting on the semi-solid powder compact in the compaction direction; ε_{eq} is the equivalent strain of the matrix material.

The influence of die wall friction is critical to the overall density and the density distribution along the compression axis. As the aspect ratio of compact height to radius (*H/R*) becomes large, the powder–die friction becomes significant and influences the density distribution. The slab equilibrium theory holds when *H/R* is greater than two (Brewin, Coube et al. 2008):

$$d\sigma_{zz}^{ssm}/\sigma_{zz}^{ssm} = \left(\frac{2\mu\alpha}{R}\right) dz \tag{2.7}$$

where, μ is the friction coefficient between the powder compact and the die wall; α is the stress transmission coefficient, where $\alpha=\sigma_{yy}^{ssm}/\sigma_{zz}^{ssm}$ and can be related to Poisson's ratio (v) with $\alpha=v/(1-v)$; and R is the radius of the die. σ_{yy}^{ssm} are normal stresses to the semi-solid powder compact in the y direction. Strain increments in principal directions derived from the plastic potential can be used to express the Poisson's ratio in terms of density by (Shima and Oyane 1976):

$$v = \frac{0.5\left(1 - \frac{2}{9f^2}\right)}{1 + \frac{1}{9f^2}} \tag{2.8}$$

Following a similar procedure suggest by Kang et al. (Kang and Jung 1999), the stress taken by the pore can be calculated as $\sigma_{ij}^{pore}=\delta_{ij}p_g f_g$, where, δ_{ij} is Kronecker delta; p_g is the hydrostatic pressure of pores; and f_g is the volume fraction of the porosity. The hydrostatic pressure within the pores enclosed by the solid-liquid mixture can be estimated from (Svoboda, Riedel et al. 1996):

$$p_g = p_{ex}\frac{f_{g_{cl}}}{f_g}\frac{1 - f_g}{1 - f_{g_{cl}}} - p_{ex} \tag{2.9}$$

where, p_{ex} is the external gas pressure (i.e., the atmospheric pressure); f_{gcl} is the pore close porosity (typically, f_{gcl} is 0.125 (Svoboda, Riedel et al. 1996)).

Therefore, the overall stress required to compress the semi-solid powder compact can be evaluated with Eqn. (2.3), where the stress component acting on the semi-solid matrix phase and pores are calculated by Eqns. (2.5) and (2.9), respectively. The stress distribution along the compaction direction is obtained by Eqn. (2.7).

2.3 Experimental Procedure

Gas atomized Al6061 powder was used for the closed-die compaction to verify the developed analytical approach. The mean size of the Al6061 powder (Valimet, Inc.)

was 13.8 μm. The alloy composition of the Al6061 powder is listed in Table 2.1. The experimental setup for the SPP is shown in Fig. 2.3. The die was fabricated from H13 tool steel and was heat treated to hardness of HRC 50. To lubricate the die and prevent possible reaction between the aluminum and the die material at elevated temperatures, boron nitride (Momentive Performance Materials-Quartz, Inc.) was sprayed on the die wall. The Al6061 powder was pre-compacted at 50 MPa using materials testing system (TestResources Inc, 800LE) at room temperature.

Table 2.1: Chemical composition of Al6061

Element	Al	Mg	Si	Cu	Fe	Cr	Zn	Mn	Ti
Amount (%)	Bal.	1.03	0.52	0.28	0.27	0.09	0.06	0.03	0.01

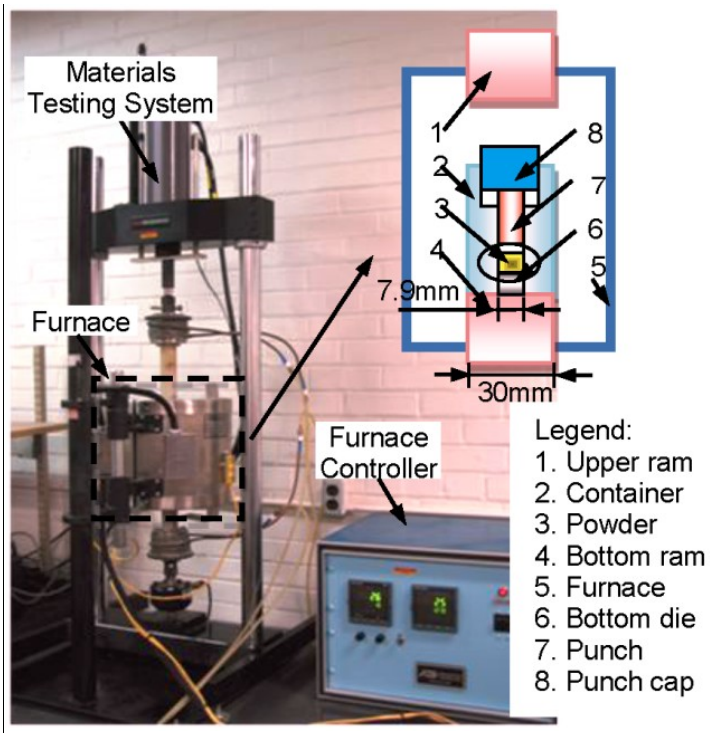

Fig. 2.3: Experimental setup for semi-solid powder processing

At elevated temperatures, pressure was applied for densification of the powder compact. The experimental conditions and model parameters are summarized in Table 2.2. Eight temperature settings ranging from 550°C to 645°C, with liquid fraction in the range of 0–41.8%, were used in the experiments. The liquid fractions at different temperatures were obtained from ThermoCalc and verified with experimental results of differential scanning calorimetry analysis conducted by Kim and Kang et al. (2007). The temperature profiles for the experiments at 600°C settings are shown in Fig. 2.4, and other temperature profiles are similar. After heating the pre-compact to the target temperature, a constant punch velocity of 0.01 mm/s was applied. Maximum pressure applied varied from 15 MPa through 50 MPa to analyze the effect of friction on the relative density distribution according to Eqn. (2.7).

Table 2.2: Experimental settings and parameters

Temperature	Liquid fraction (%) (2007)	Compaction pressure (MPa)	Friction coefficient used in model	Model parameters		
				a	b	n
550°C	0.00	50	0.55	2.1	0.5	2.6
580°C	3.88	50	0.55	2.1	0.5	2.6
600°C	7.30	35	0.55	2.1	0.5	2.6
620°C	12.40	20	0.55	2.6	0.4	2.6
630°C	17.85	20	0.55	2.6	0.4	2.6
638°C	26.22	15	0.55	2.6	0.4	2.6
641°C	31.50	15	0.55	2.6	0.4	2.6
645°C	41.80	15	0.55	2.6	0.4	2.6

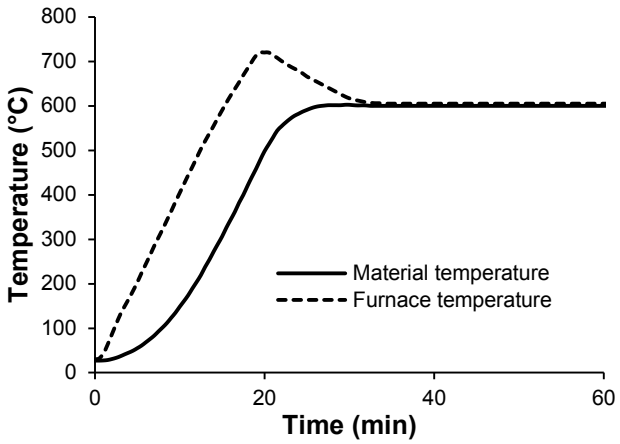

Fig. 2.4: Heating profile used in the experiments at 600°C

The density of the samples was calculated from measured mass and volume. The samples were weighed with a precision balance (Sartorius GD503, accuracy 0.0001g). The volume of the samples was calculated by measuring the diameter and height with a micrometer. Four measurements were taken at different locations of the sample, and the average value was used. Archimedes's method was not used because of the existence of large amount of open pores observed at lower densities. Samples were cut with a diamond saw and polished for optical inspection using a scanning electron microscope (JEOL JSM-606LV). Keller's etchant was used to etch the Al6061 samples for 20 seconds.

2.4 Results

The yield response of Al6061 in the semi-solid state was first discussed. The relative density during SPP was modeled and the results were compared with the experimental measurements for processing temperatures between 550°C and 645°C. Finally, compaction behavior of semi-solid powder and model limits were analyzed.

2.4.1 Estimating Yield of Al6061 in the Semi-solid Region

Lou et al. (2002) carried out compression tests with Al6061 rods in the semi-solid region from 550°C to 610°C. As shown in Fig. 2.5, the solid fraction of Al6061 dramatically decreases after 620°C, and thus, a direct extrapolation of Lou's data will lead to an overestimation of the yield of Al6061 beyond 620°C when a significant amount of liquid-phase is present. On the other hand, the solid-phase of the material will follow the temperature dependency. Therefore, we assumed that the solid-phase yield strength may be extrapolated to obtain the yield of the solid-liquid mixture above 610°C.

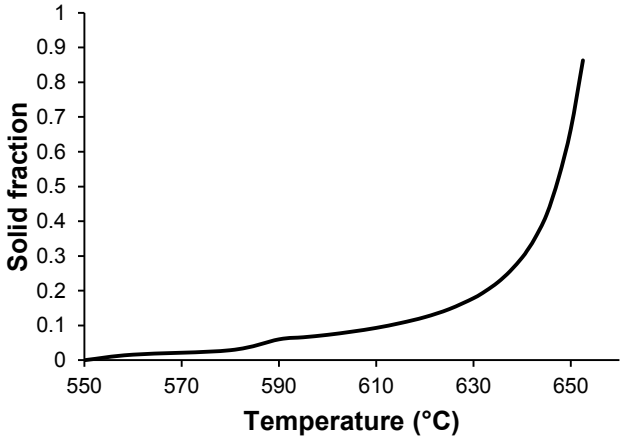

Fig. 2.5: Solid fraction of Al6061 at different temperature (data obtained from ThermoCalc 3.1)

According to Gunasekera et al. (Gunasekera 1993; Gunasekera and Zhou 1997), the yield strength of material in the semi-solid state is related to the solid-phase yield strength through the following equation:

$$\sigma_{y\_semi} = \delta \sigma_{y\_solid} \tag{2.10}$$

where δ is a parameter, function of liquid fraction (f_l) in the form of δ=1-βf_l^k. β=1.26 and k=2/3. The relation agrees well with experimental measurements up to liquid fraction of 0.4. Therefore, the solid-phase strength was calculated from Eqn. (2.10) using Lou's data and extrapolated. The fitted results are presented in Eqn. (2.11). Finally, the yield properties of the semi-solid matrix for any temperature above 550°C, σ_{y_ssm}, can be calculated from Eqns. (2.10) and (2.11). The comparison of fitted results and experimental data from Ref (Lou, Huang et al. 2002) is shown in Fig. 2.6.

$$\sigma_y = 2.9253 \ln \dot{\varepsilon} + 31.031, T = 550℃ \tag{2.11a}$$

$$\sigma_{y\_solid} = 2.0962 \ln \dot{\varepsilon} - 0.0570T + 55.71836, T \geq 570℃ \tag{2.11b}$$

where $\dot{\varepsilon}$ is the strain rate, σ_y is the yield stress (MPa) and T is temperature in the unit of °C.

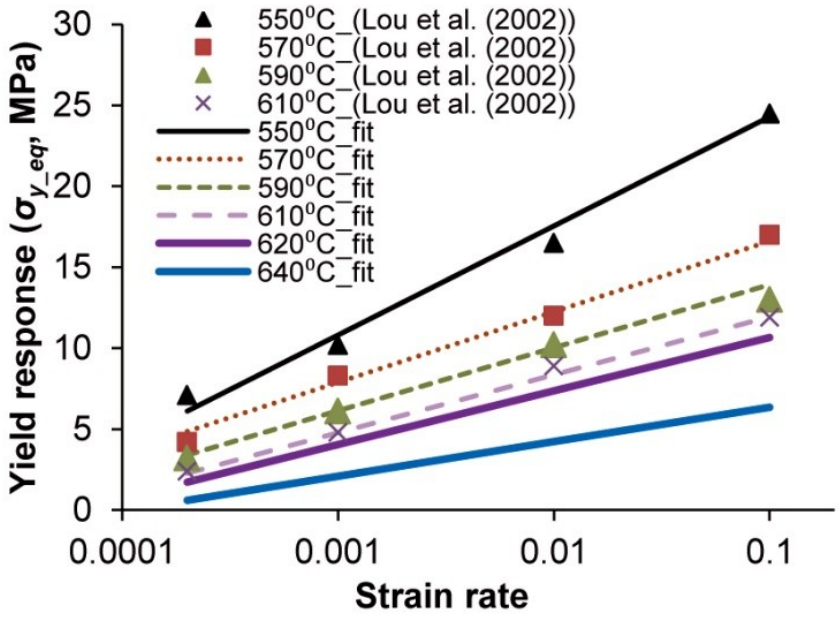

Fig. 2.6: Yield strength (σ_y_ssm) of Al6061 above 550°C.

2.4.2 Liquid-phase Formation in Al6061 Particles in the Semi-solid State

The microstructures and the morphologies of the original Al6061 particles, Al6061 particles heated to 620°C or 641°C and cooled to room temperature are shown in Fig. 2.7. In the back-scatter mode, the white dots (or streak marks) and agglomerations were found to be a combination of Mg (1.3-2 wt.%), Si (1.2-4 wt.%), Fe (4-10 wt.%), Cu (~0.5 wt.%), Cr (~0.5 wt.%) and Al (bal.) according to the EDX results obtained from multiple positions with large white agglomerations. The solidification patterns were shown in Fig. 2.7(a) and (b). The alloy elements were uniformly distributed in the whole particle. After heating up to 620°C and cooling to room temperature, the alloy elements slightly agglomerated (Fig. 2.7(d)). The alloy elements further agglomerated into large white spots as shown in Fig. 2.7(f).

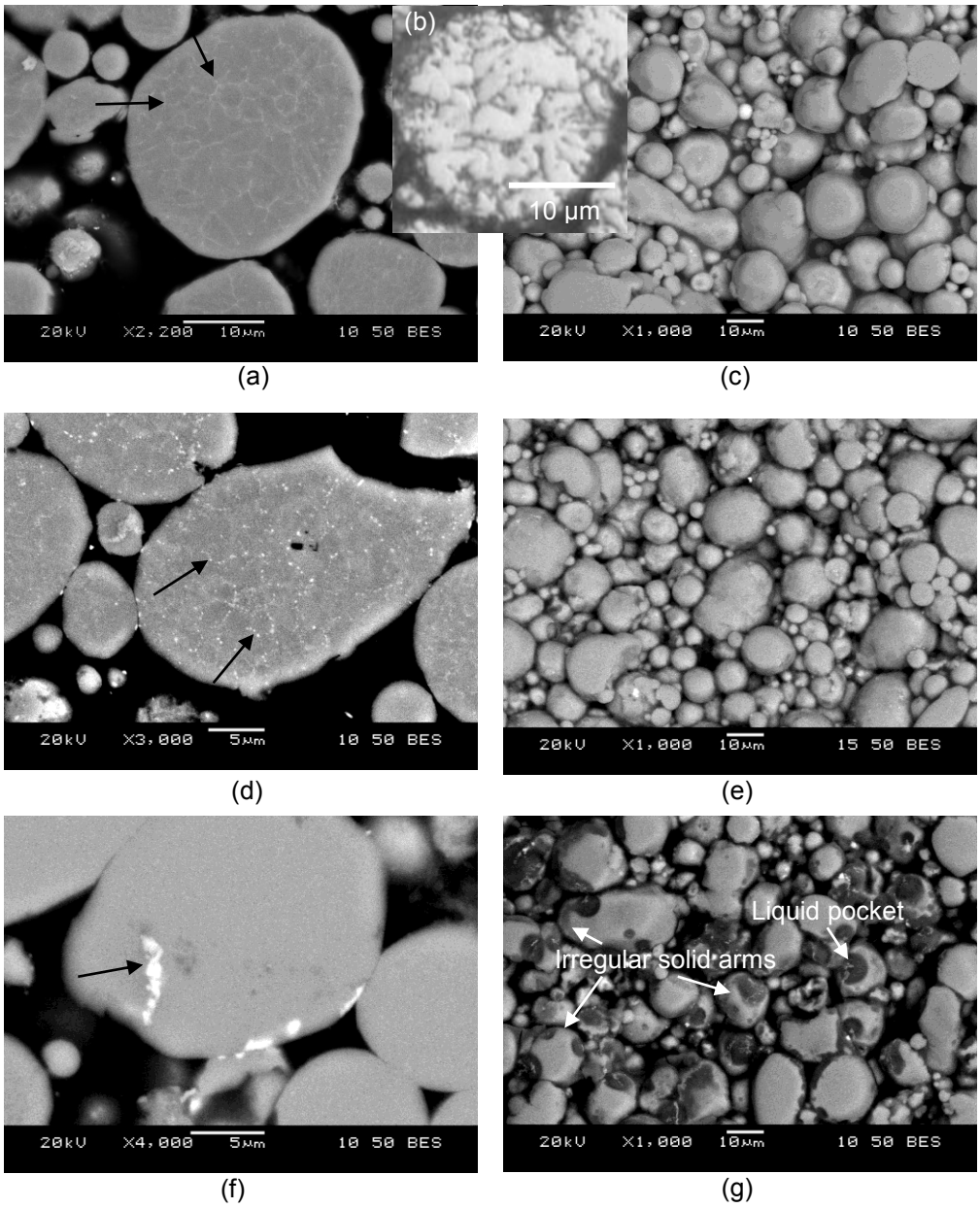

Fig. 2.7: Microscopy images for Al6061 particles. (a) and (c) back-scatter images of original Al6061 particles; (b) optical image of original Al6061 particles (polished and etched); (e) and (f) Al6061 particle heated to 620°C; (g) and (h) Al6061 particle heated to 641°C.

The melting of the particle will most likely occur along solidification patterns. From the Fig. 2.7(a) and (b), the melting may start both inside and on the surface of the

particles at 620°C. When the temperature approached to 641°C, the melting significantly increased at the surface of the Al6061 particle. Liquid pockets formed and resulted in irregular solid arms. This is captured in Fig. 2.7(g) where large number of liquid pockets or channels on the particle surfaces formed at 641°C. These geometries (dark pockets or channels) were not observed at lower temperature (Fig. 2.7(c) and (e)).

2.4.3 Compaction Curve

The prediction of relative density with the model matched the results for temperature ranges from 550°C to 630°C at which the liquid fraction of Al6061 was from 0 to 0.18, as shown in Fig. 2.8. Since the powder was pre-compacted at room temperature at 50 MPa, it would require a finite amount of pressure to initiate the deformation of the powder compact. As shown in Fig. 2.8, Shima-Oyane model was able to capture the initial pressure required to deform the pre-compacted powder in the semi-solid state. The parameters used in the model are listed in Table 2.2.

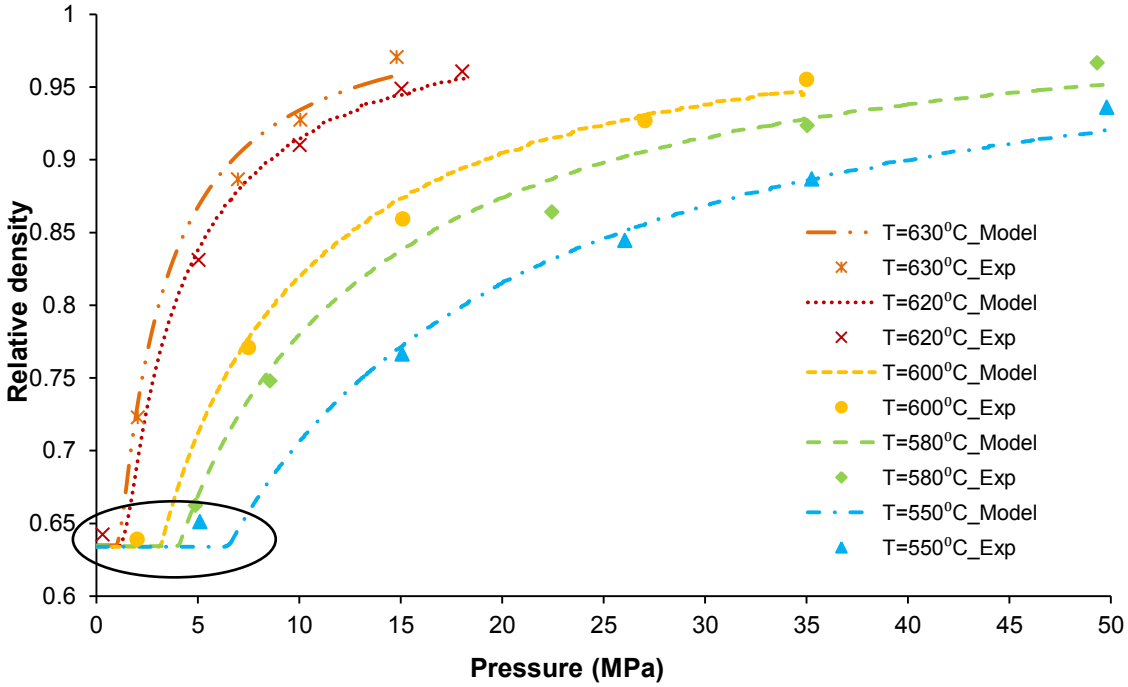

Fig. 2.8: Experimental and modeling results for semi-solid powder compaction from 550°C to 630°C

In the model, the parameters, *a* and *b*, were different for temperatures below and above 600°C. It was speculated that the structural deformation property changed when high amount of liquid-phase was present. When the liquid fraction is low, the liquid material is isolated within the particle during deformation. On the other hand, at higher liquid-phase content, the liquid-phase may form a connected network leading to change in the structural response of the compact. This can be captured by changing the structural parameters, *a* and *b*.

As shown Fig. 2.9, when the pressure (*P*) was normalized by the pressure required to obtain a relative density of 0.95 ($P_{D=0.95}$), the compaction curves collapse into a single curve for temperatures between 550°C and 630°C. This indicated that the overall

deformation mechanism of Al6061 in the semi-solid region at lower liquid fraction was consistent. The relation can be represented with a simple expression:

$$P/P_{D=0.95} = Ae^{B\times D} \tag{2.12}$$

where, the fitted values were A = 5.40×10^{-4} and B = 7.90.

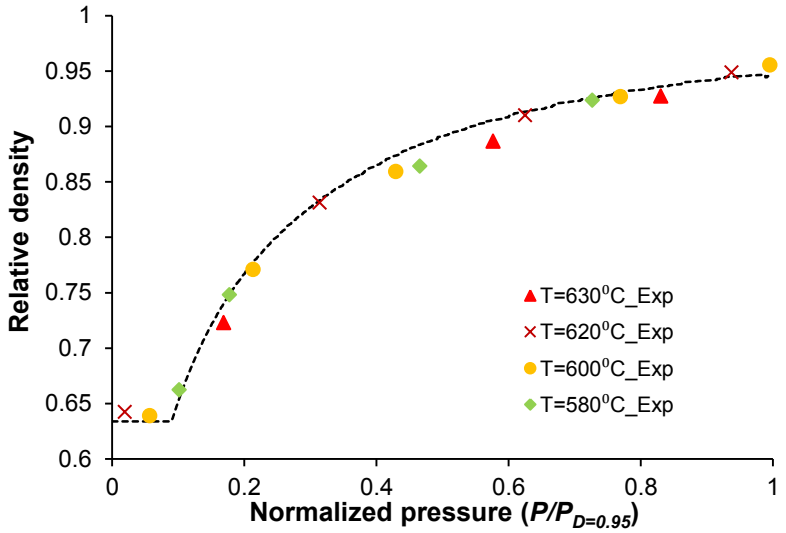

Fig. 2.9: Normalized experimental and modeling results for semi-solid powder compaction

The compaction behavior results between 638°C and 645°C are separately shown in Fig. 2.10. The relative density curve was calculated from the punch displacement data for three different temperatures. To validate the approach, additional five samples were fabricated at varying pressures at 638°C. Their actual densities were measured are shown as black square tick marks.

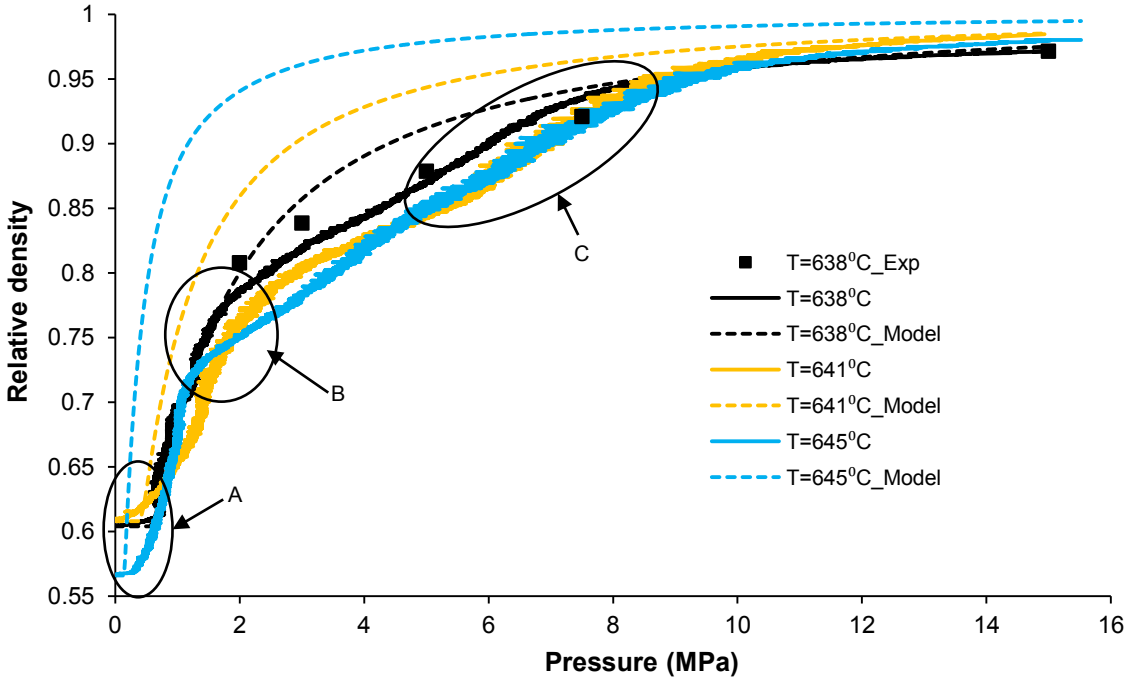

Fig. 2.10: Experimental results for semi-solid powder compaction from 638°C to 645°C.

It was quite obvious that the model failed to predict the density change in these high temperature ranges. As shown in Fig. 2.10, the relative density–compaction pressure curves were similar to each other for temperatures between 638°C to 645°C, although the liquid fraction varied from 26% to 42%. It was noted that the liquid-phase escaped during the compaction process for temperatures above 630°C as summarized in Table 2.3. Excessive amount of liquid material squeezed out during the initial stage of compaction, and the resultant material content (i.e., the liquid fraction in the leftover material) was similar in these three. Consequently, similar pressure–density curves were observed for temperatures between 638°C and 645°C in spite of the significantly different initial liquid content.

Table 2.3: Liquid materials squeezed out during SPP

Temperature	Compaction pressure (MPa)	Liquid squeezed out (g/0.9g)	Original liquid fraction (%)	Liquid fraction in leftover material (%)
550°C-620°C	Varies	0	0	0
630°C	15	0.008	17.85	17.11
638°C	2	0.055	26.22	21.42
	3	0.052		21.70
	5	0.055		21.42
	7.5	0.065		20.40
	15	0.063		20.67
641°C	15	0.112	31.50	21.76
645°C	15	0.165	41.80	28.73

The characteristic of the curve shape was different from those at lower temperatures because of the agglomeration of liquid materials. An apparent change of stress–density response was observed at location A. At high liquid-phase content, irregular solid-phase morphology was formed as shown in Fig. 2.7(g). The interlocking of the irregular solid arms may have result in strengthening of the material causing a sudden change in the densification behavior.

A schematic of powder compaction of Al6061 at low and high liquid fractions is illustrated in Fig. 2.11. The compaction behavior of the powder compact in the semi-solid state can be summarized as the following:

1) When the liquid fraction is below 10%, an isolated liquid-phase formation is observed throughout the particle (see Fig. 2.11(b)). Shima-Oyane model is capable of predicting the compaction behavior in the semi-solid state.
2) When the liquid fraction is between 10% and 20%, some of the liquid-phase within the particle may form a network (Fig. 2.11(c)). The material structural parameters, i.e. *a* and *b*, in the Shima-Oyane model need to be corrected to account for liquid-phase effect on the powder compaction behavior.
3) When the liquid fraction is higher than 20%, the compaction mechanism deviated from that of Shima-Oyane model because of the squeeze out of the liquid-phase and the formation of solid-phase with irregular morphology. The Shima-Oyane model is no longer applicable in this region.

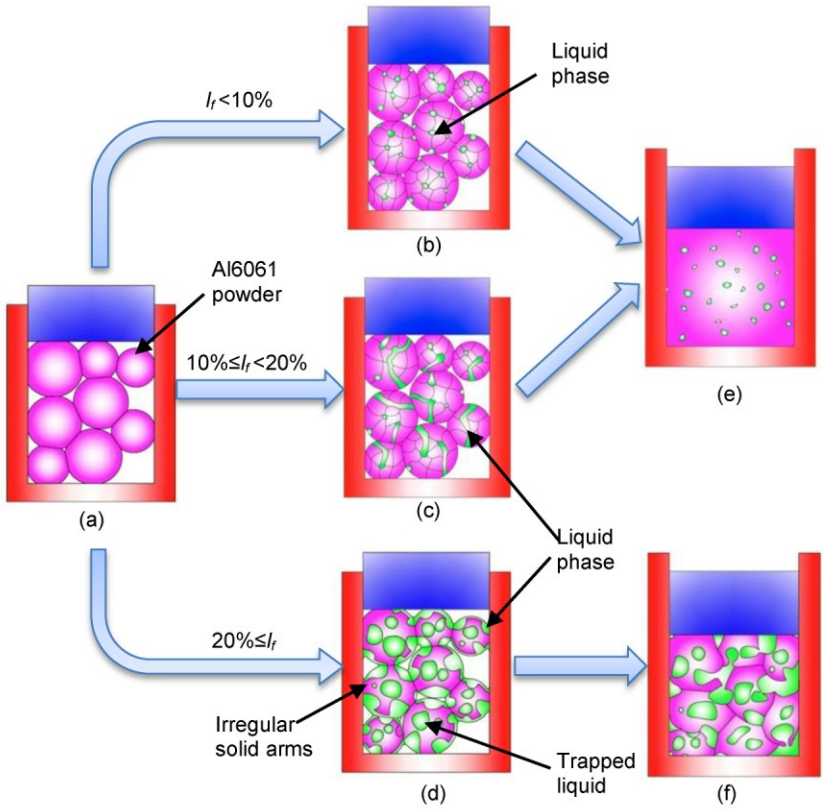

Fig. 2.11: Illustration of various stages in powder compaction of an alloy material in semi-solid regime: (a) powder compact at room temperature; (b)–(d) powder compact at semi-solid state; (d) and (e) densification of the powder compact

2.4.4 Density and Stress Distribution

Relative density distribution at 600°C is presented in Fig. 2.12. The top of the sample was contacting the moving punch, and the bottom of the sample was in contact with the stationary die. As expected, the relative density of the sample decreased from the top of the sample to the bottom. The model predicted the density distribution reasonably well.

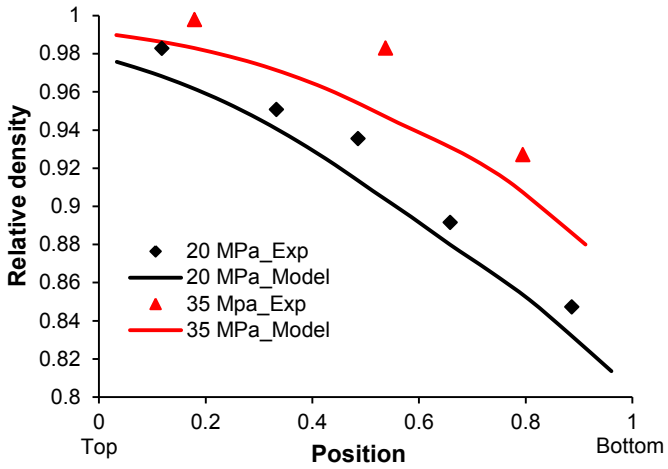

(a)

Fig. 2.12: Relative density distribution within the powder compact fabricated and predicted at 600°C.

The rate change of relative density (dD/dt, where t is time) at different powder compact location during the compaction process at 620°C is shown in Fig. 2.13. Relative density rate showed a contrasting behavior at the top and bottom surfaces as the pressure was applied. In the beginning, the densification immediately started near the top surface where the powder was in contact with the moving punch, while densification is minimal near the bottom of the compact. As the pressure is applied to the powder compact, the densification progressed through the bottom of the compact. In the late stage of the compaction process, the density increasing rate at the bottom was higher than that at the top.

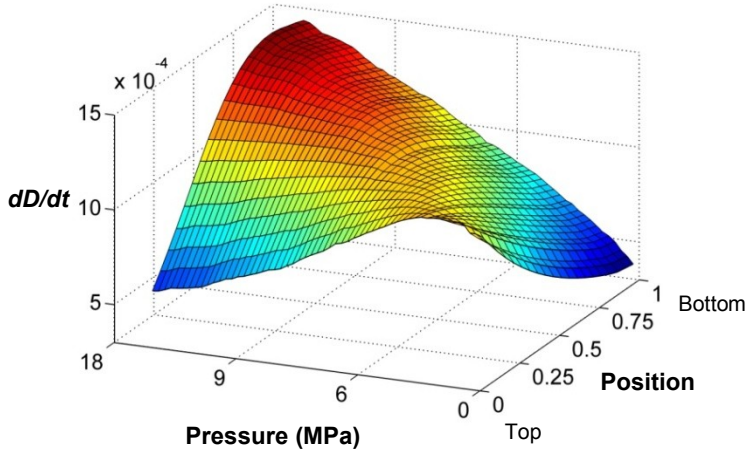

Fig. 2.13: Density changing rate at different position for different compaction pressure at 620°C.

2.5 Conclusion

The compaction behavior of Al6061 powder in the semi-solid temperature range with liquid content up to 42% was studied. The Shima-Oyane model was successful at capturing the compaction behavior of semi-solid powder when the liquid fraction was relative low (<20%). When liquid fraction was above 10%, the material structural response changed, which resulted in adjusting of the material structural parameters, *a* and *b*. As the liquid content increased to higher than 20%, the model prediction deviated from the experimental measurements. Microstructural analysis showed that the liquid-phase was no longer uniformly distributed within the particle, but rather agglomerated into liquid pockets. Liquid-phase squeeze out and interlocking of irregular solid-phase may have resulted in changes in the compaction behavior. It was also discovered that all the normalized pressure–relative density curves in temperature ranges between 580°C

and 620°C merged into a single curve and can be expressed with a simple exponential expression. The effects of die wall–powder friction on the relative density distribution along the compaction direction were also successfully predicted by the model.

CHAPTER 3 DENSIFICATION BEHAVIOR OF AL6061 AND SIC BINARY POWDER MIXTURE IN SEMI-SOLID STATE

3.1 Introduction

Semi-solid powder processing (SPP) combines the benefits of the semi-solid forming and powder metallurgy (Steinhoff, Weidig et al. 2004; Kim, Koc et al. 2007; Kim, Ni et al. 2007). It allows the flexibility of mixing various powders for tailored composite properties (El Wakil 1992; Luo, Cheng et al. 2006; Wu, Kim et al. 2010b) and minimizes post processing steps typically required in powder metallurgy routes. Fully densified composites and components can be fabricated with relatively low pressure. Composite materials including Al-SiC (Guo and Tsao 2000; Chen, Yang et al. 2004; Wu 2009; Wu, Kim et al. 2010a; Wu, Kim et al. 2011) and Al-CNT (Wu and Kim 2011a) have been successfully fabricated by semi-solid powder processing, which have demonstrated a promising potential of SPP as a viable metal matrix composite manufacturing process.

The compaction of powder mixtures has been investigated for decades. Lange *et al.* (Lange, Atteraas et al. 1991) investigated cold compaction of aluminum and steel particles and speculated that the steel formed local network when the volume fraction was larger than 20 vol%. Hafizpour *et al.* (Hafizpour 2008) examined the compaction behavior of Al+SiC powder mixtures with variation of SiC particle size by Heckel equation (Denny 2002), Panelli equation (Panelli and Ambrozio Filho 2001), and

Cooper-Eaton equation (Cooper and Eaton 1962). The results showed that the compaction pressure increased as the particle size of SiC decreased. Compaction of powder mixture with up to 60% hard phase reinforcement was also investigated, and mechanical properties of the pressed parts were studied (Martin, Lame et al. 2000). Theoretical models were proposed by Storakers et al. (Storåkers, Fleck et al. 1999), Bouvard (Bouvard 1993), and Kim *et al.* (Kim, Cho et al. 2000) to predict the compaction behavior of powder mixtures at room temperature. However, little research was found on the compaction behavior of powder mixtures at elevated temperatures involving liquid-phase, i.e., semi-solid or mushy state.

In Storakers's model, a reinforcement factor K_R was proposed to describe the increase of stress required to compact the powder mixture containing hard and soft particles compared with that required for the monolithic soft phase particles at room temperature (Storåkers, Fleck et al. 1999). Assuming that the powder mixture and the monolithic powder are subjected to the same strain history, ε_{ij}, the macroscopic stress in the powder mixture, σ_{ij}^{C}, is related to the macroscopic stress of the monolithic soft powder, σ_{ij}^{m}. For a closed-die compaction the following relationship can be established according to Storakers (1999):

$$\sigma_{zz}^{C} = K_R \sigma_{zz}^{m} \tag{3.1}$$

$$\varepsilon_{zz} = 1 - \frac{D_0}{D} \tag{3.2}$$

where D_0 and D are the initial relative density and relative density of the powder compact, respectively; and z is the compaction direction. If the hard phase is assumed rigid compare with the soft phase, K_R is only a function of the hard phase volume fraction and initial powder mixture and soft phase densities as the following:

$$K_R = \frac{{D_0^C}^2}{D_0^{m2}} \frac{1}{1 - f_h^2} \tag{3.3}$$

where D_0^C and D_0^m are the initial density of the powder mixture compact and monolithic soft phase powder compact, respectively. The hard phase volume fraction can be calculated by:

$$f_h = \frac{V_h}{V_h + V_s} \tag{3.4}$$

where V_h and V_s are the volumes of the hard phase and soft phase materials, respectively. Eqn. (3.3), however, is only applicable when particle size distribution is small and hard phase volume fraction is smaller than 30% as explained in the work by (Sridhar and Fleck 2000) for Al+SiC powder mixture. The percolation of hard phase particles was not considered.

In this work, the compaction behavior of Al6061 and SiC powder mixtures in the semi-solid state was investigated. Al6061 with various SiC volume fractions (0%-60%) were compacted at temperatures involving Al6061 solid-phase (550°C), semi-solid range (550°C-650°C), and complete liquid-phase (660°C). The effects of SiC volume fraction

and Al6061 liquid fraction on the densification behavior of the powder mixture were experimentally investigated.

3.2 Experimental procedure

Al6061 powder (Valimet, Inc.) and SiC particles (AEE Inc.) were used to study the compaction of powder mixture in the semi-solid state. The composition of Al6061 particle is listed in Table 3.1, and the size of the Al6061 and SiC particles are summarized in Table 3.2. Al6061 and SiC particles were mixed by SPEX 8000M mixer/miller for one hour at 1200 rpm.

Table 3.1: Chemical composition of Al6061 (Valimet, Inc.)

Element	Cr	Cu	Fe	Mg	Mn	Si	Ti	Zn	Al
Amount (%)	0.09	0.28	0.27	1.03	0.03	0.52	0.01	0.06	Bal.

Table 3.2: Powder size and distribution of Al6061 and SiC powders

Powder type	Powder Size (μm)	Size Distribution (μm)		
		d_{90}	d_{50}	d_{10}
Al6061	5-23	22.97	13.82	5.67
SiC	10			

The experimental setup for the SPP is shown in Fig. 3.1. The die was fabricated from H13 tool steel and was heat treated to hardness of HRC 50. Boron nitride (Momentive Performance Materials-Quartz, Inc.) was sprayed on the wall to lubricate the die and prevent possible reaction between the aluminum and the die material at elevated temperatures. The powders were heated to target temperatures ranging from 550°C to 670°C in a tubular furnace (Applied Test System Inc). The liquid fractions of Al6061 (f_L) at different temperatures are shown in Fig. 3.2. The data were obtained from ThermoCalc and verified with experimental results of differential scanning calorimetry analysis conducted by Kim and Kang *et al.* (2007). The temperature profiles for the experiments at 600°C settings are shown in Fig. 3.3, and other temperature profiles are alike. Pressure was applied after the powders achieved the target temperature using materials testing system (TestResources Inc, 800LE). The detailed experimental settings are listed in Table 3.3.

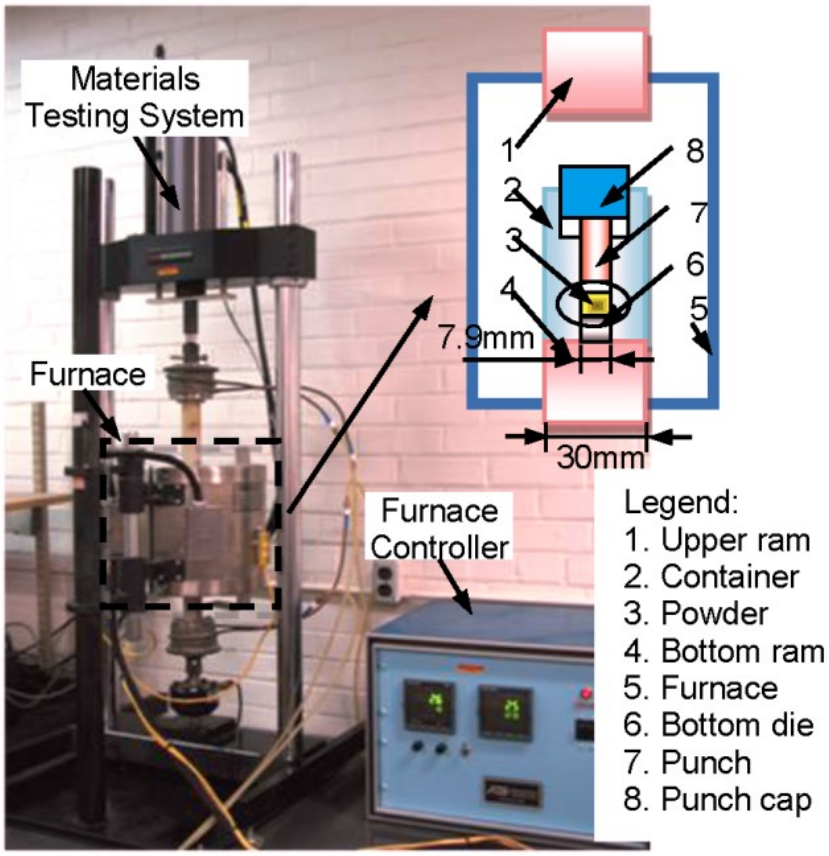

Fig. 3.1: Experimental setup for semi-solid powder processing

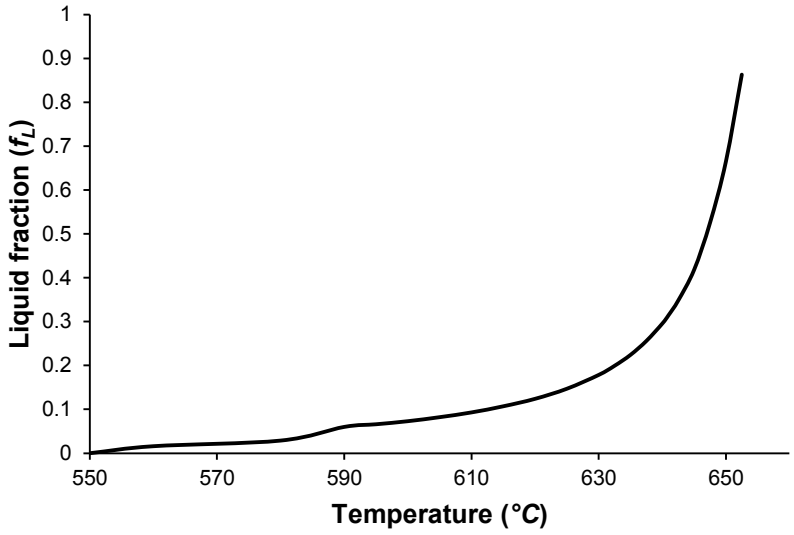

Fig. 3.2: Liquid fraction of Al6061 (f_L) at different temperature

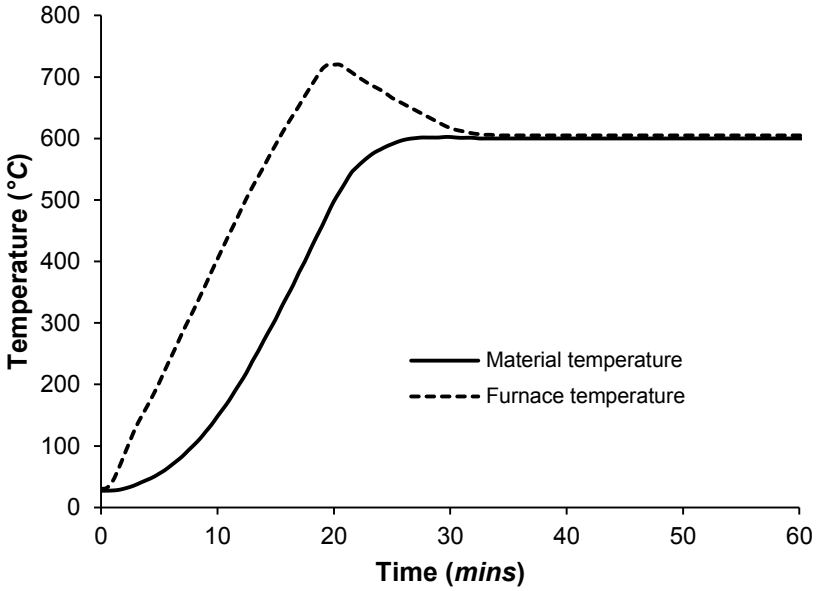

Fig. 3.3: Heating profile used in the experiments at 600°C

Table 3.3: Experimental settings

Experiment number	Temperature (°C)	Liquid fraction in Al6061 (%) (2007)	SiC vol. fraction (%)	Overall liquid fraction (%)	Compaction pressure (MPa)
1	550	0.00	0	0.00	150
2	580	3.88	0	3.88	150
3	600	7.30	0	7.30	150
4	620	12.40	0	12.40	75
5	630	17.85	0	17.85	75
6	638	26.22	0	26.22	35
7	550	0.00	10	0	150
8	580	3.88	10	3.49	150
9	600	7.30	10	6.57	150
10	620	12.40	10	11.16	100
11	630	17.85	10	16.07	100
12	638	26.22	10	23.60	50
13	645	41.80	10	37.62	35
14	550	0.00	20	0	150
15	580	3.88	20	3.10	150
16	600	7.30	20	5.84	150
17	620	12.40	20	9.92	150

Table 3.3: Experimental settings (continued)

Experiment number	Temperature (°C)	Liquid fraction in Al6061 (%) (2007)	SiC vol. fraction (%)	Overall liquid fraction (%)	Compaction pressure (MPa)
18	630	17.85	20	14.28	150
19	638	26.22	20	21.00	100
20	550	0.00	40	0	150
21	580	3.88	40	2.32	150
22	620	12.40	40	7.44	150
23	638	26.22	40	15.73	150
24	550	0.00	50	0	150
25	580	3.88	50	1.94	150
26	620	12.40	50	6.20	150
27	630	17.85	50	8.93	150
28	638	26.22	50	13.11	150
29	645	41.80	50	20.90	150
30	648	56.30	50	28.15	150
31	651	73.50	50	36.75	150
32	660	100	50	50.00	150
33	550	0.00	60	0	150
34	580	3.88	60	1.55	150
35	620	12.40	60	4.96	150
36	638	26.22	60	10.48	150

The density of the samples was calculated from measured mass and volume. The samples were weighed on a precision balance (Sartorius GD503, accuracy 0.0001g). The volume of the samples was calculated by measuring the diameter and height with a micrometer. Four measurements were taken at different locations of the sample, and the average value was used. Archimedes's method was not used because of the existence of large amount of open pores observed at lower densities.

3.3 Results

The initial density of the powder mixture was first examined. Compaction curves of the powder mixture with different Al6061 liquid fraction and SiC volume fraction was discussed. The reinforcement factor K_R was obtained for different SiC volume fractions with different Al6061 liquid fraction. Liquid factor K_L was proposed and investigated for the compaction of powder mixtures at different liquid fractions.

3.3.1 Initial density of the powder mixture

The initial density of the powder mixture is shown in Fig. 3.4. The initial density of the powder mixture is important for the calculation of K_R and was estimated through the compaction curves and the density of the final parts. The results show that the initial density of the powder mixture decreased as the SiC volume fraction increased. A linear relation can be used to describe the initial relative density of powder mixture with different SiC volume fractions:

$$D_0 = -0.2233 f_{SiC} + 0.5434 \tag{3.5}$$

where f_{sic} is the volume fraction of SiC powder as calculated by Eqn. (3.4). $D_0^m = 0.5434$ when f_{SiC}=0.

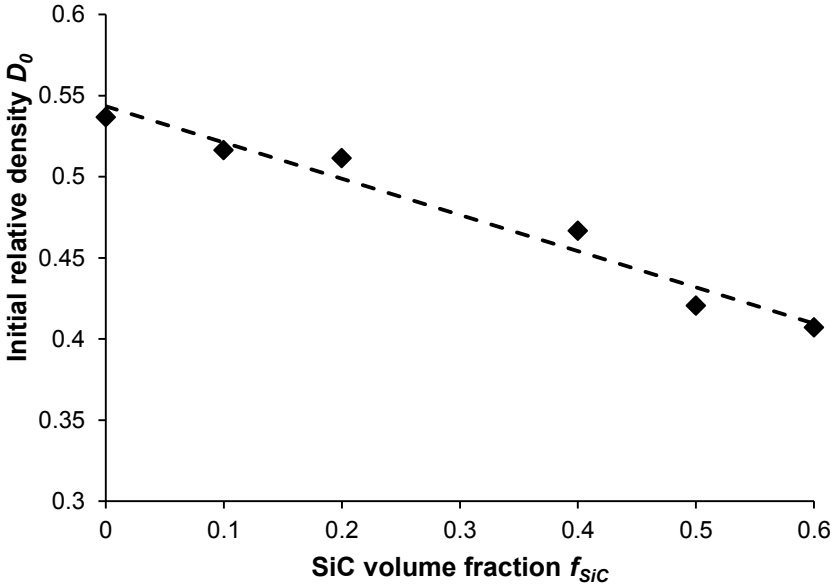

Fig. 3.4: Initial density of the powder mixture with different SiC volume fraction

3.3.2 Compaction curves

The compaction curves for the Al6061-SiC with different SiC volume fraction and temperature are shown in Fig. 3.5. Apparently, higher pressure was required for the compaction of powder mixture with lower temperature and higher SiC volume fraction. When the volume fraction of SiC increased, the compaction pressure increased significantly because of the percolation of SiC particles (Fig. 3.5(b)).

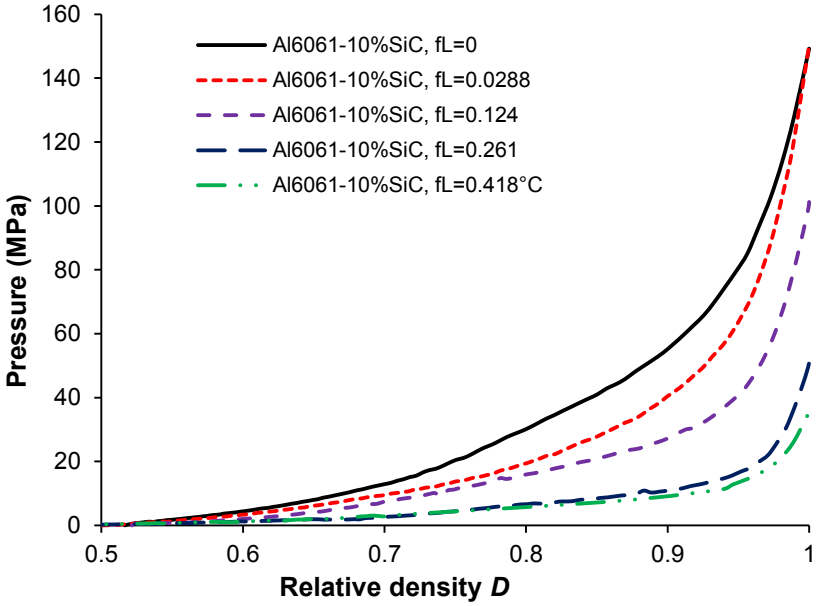

(a)

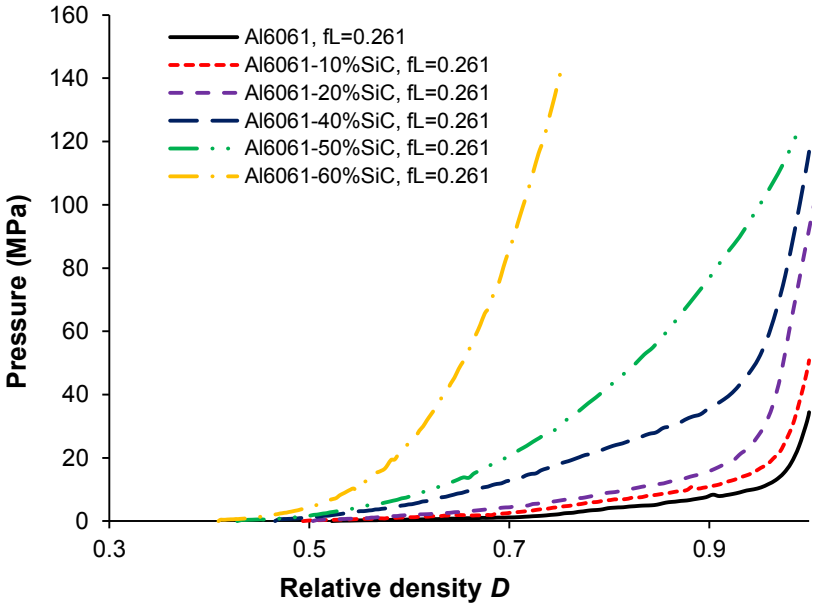

(b)

Fig. 3.5: Compaction curves for (a) Al6061-10 vol% SiC at different liquid fraction and (b) Al6061-SiC at f_L=0.261 with different SiC volume fraction

3.3.3 Reinforcement factor K_R

The effect of SiC volume fraction and liquid fraction was investigated by analyzing the evolution of K_R computed by Eqn. (3.1) from the experiments. As shown in Fig. 3.6(a), within the region of f_L <10% or f_L >10%, K_R values were similar when SiC fraction is fixed and smaller than 30%. The K_R values for f_L>10% were higher than those for f_L<10%. This is possibly because the connectivity of liquid-phase in the Al6061 particles changed as the liquid fraction increased. When the liquid fraction in Al6061 is low (<10%), the liquid-phase is enclosed in the Al6061 particles. At higher liquid fraction (>10%), the liquid-phase interconnected and may flow freely within the powder compact (Wu and Kim 2011b).

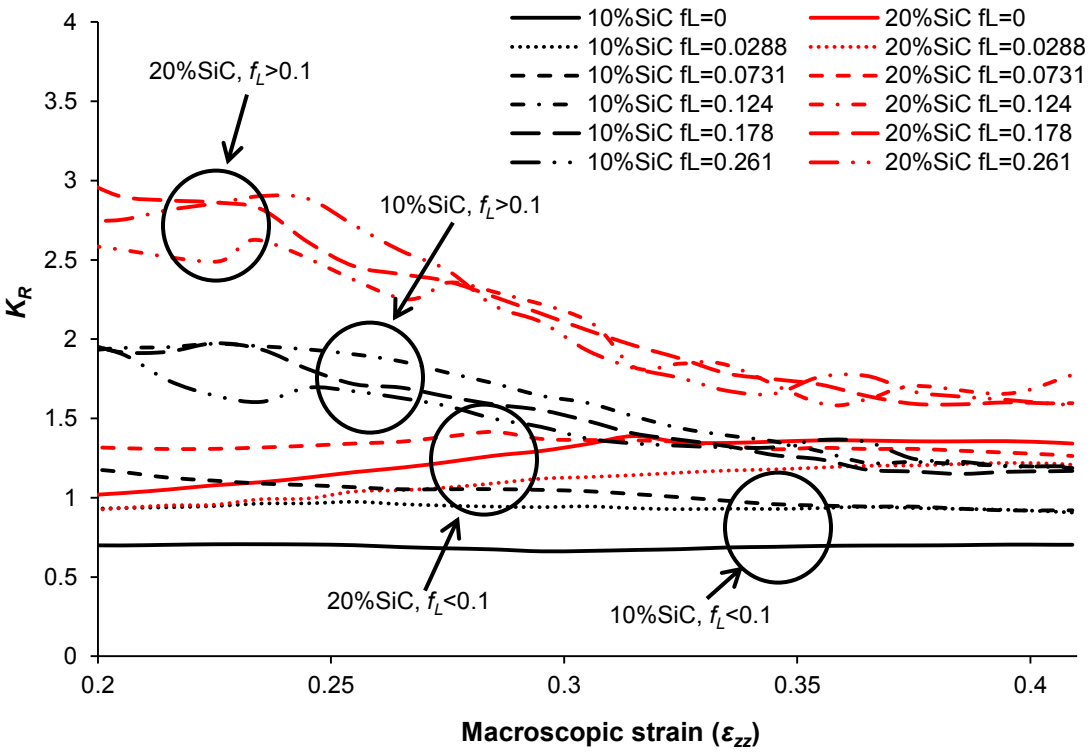

(a)

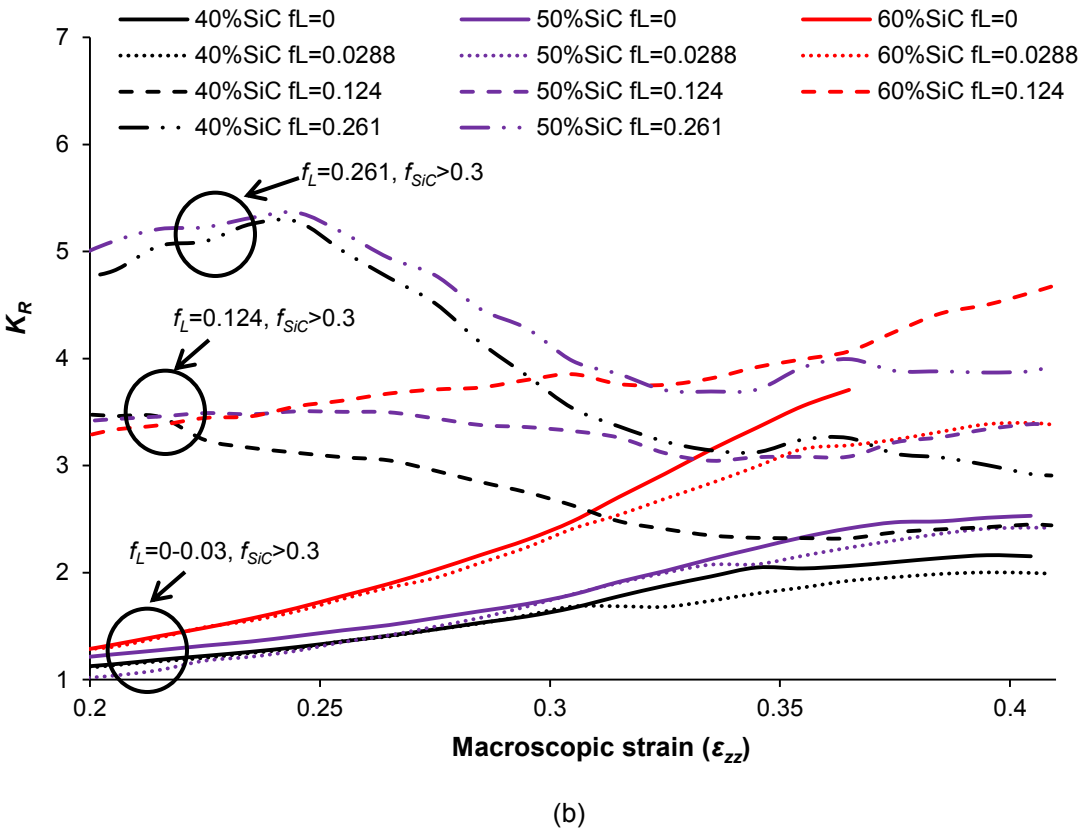

(b)

Fig. 3.6: K_R values with different Al6061 liquid fraction with (a) <30%SiC and (b)>30%SiC

When the SiC fraction is higher than 30%, the starting K_R value was determined by the liquid fraction, i.e., the higher the liquid content the higher the initial K_R (Fig. 3.6(b)). At low liquid fraction (f_L<10%), the K_R values increased as the powder mixture underwent compaction. As the liquid fraction increased, the K_R values showed more fluctuation with less increasing behavior. The fluctuation of the K_R for high liquid-phase content (f_L=0.261) related to liquid-phase squeeze out phenomenon observed by (Wu and Kim 2011b).

The effect of SiC volume fraction on K_R values can also be observed from Fig. 3.6. Higher SiC volume typically resulted in higher K_R values (Fig. 3.6(a) and Fig. 3.6(b) at

higher strain). Distinct K_R curves were observed for SiC fraction below and above 30% (compare Fig. 3.6(a) and Fig. 3.6(b)). For powder mixture with low SiC content, the reinforcing particles were isolated by the Al6061 powders, and therefore, the deformation of Al6061 particles dominated the compaction behavior (Storåkers, Fleck et al. 1999). As the SiC volume fraction is increased above 30%, the strengthening effect from the SiC particles became more significant with increasing strain. As the densification of the powder mixture progresses, the SiC particles started to interact and the percolation of SiC particles is increased, which significantly increases the compaction.

3.3.4 Liquid factor K_L

The normalized compaction curves with 10vol.% and 60vol.%SiC at different liquid fractions are shown in Fig. 3.7. The curves were normalized by the compaction pressure at relative density of 0.95 and 0.68 for 10vol.% and 60vol.% SiC volume fraction, respectively. The compaction curves collapse into a single curve for all Al6061 liquid fractions. This indicated that when the SiC volume fraction was the same, the compaction behaviors of the powder mixture with various Al6061 liquid fractions were similar.

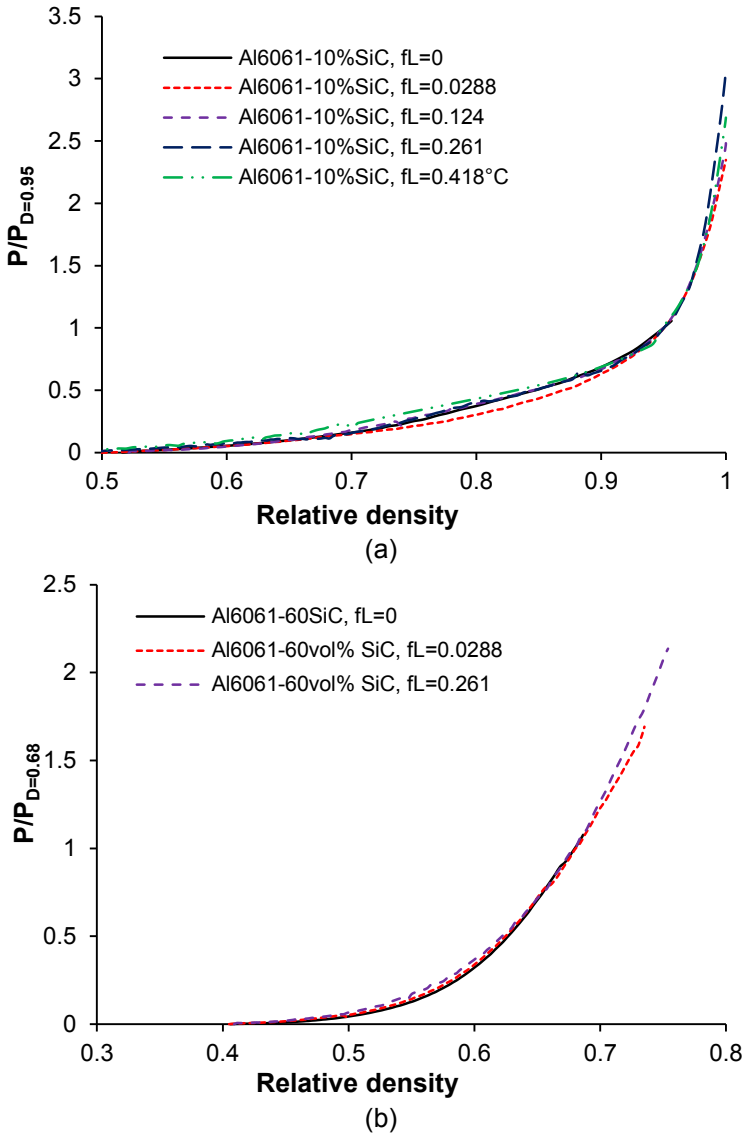

Fig. 3.7: Compaction curves for (a) Al6061-10 vol% SiC at different temperature and (b) Al6061-SiC at 638°C with different SiC volume fraction

A factor K_L can be defined as the ratio of the compaction pressure for the two powder mixtures containing the same amount of SiC subjected to the same strain history but with different Al6061 liquid fraction, f_L and f_{L0} (at T and T_0).

$$K_L = \frac{\sigma^C_{zz,f_{SiC},f_L}}{\sigma^C_{zz,f_{SiC},f_{L0}}} \tag{3.6}$$

where $\sigma^C_{zz,f_{SiC},f_L}$ is the compaction pressure required to compact the Al6061-SiC powder mixture with f_{SiC} volume fraction of SiC with Al6061 liquid fraction of f_L. The computed K_L values for f_L=0.0288-0.261 (T=580°C–638°C) with f_{L0}=0 (T_0=550°C) are shown in Fig. 3.8. The variation of K_L at different density is limited and an average can be calculated.

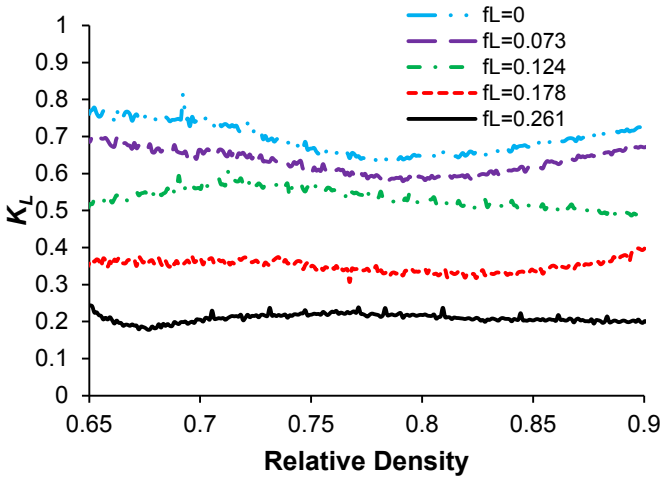

Fig. 3.8: K_L vs. relative density for powder mixture compacted with different liquid fraction with 10vol% SiC; f_{L0}=0

Choosing f_{L0} = 0 as the denominator, sets of K_L can be obtained for each SiC volume fraction powder mixtures as shown in Fig. 3.9. Although the SiC volume fraction was different (from 0% to 50%), the values of K_L were similar when the liquid fraction of Al6061 was the same. The value of the K_L decreased as the liquid fraction increased due to the decrease of the material strength as the temperature and liquid fraction increased. When the SiC volume fraction is high at 60%, the K_L value did not decrease with increasing liquid fraction. One possible explanation is the formation of the

skeleton structure by the SiC particles, which provided significant resistance during the compaction. Exponential expression was used to fit the experimental data using Eqn. (3.7) to calculate K_L:

$$K_L = e^{-5.66(f_L - f_{L0})}, \qquad f_{L0}, f_L < 0.3, 0 < f_{SiC} \leq 50\% \tag{3.7}$$

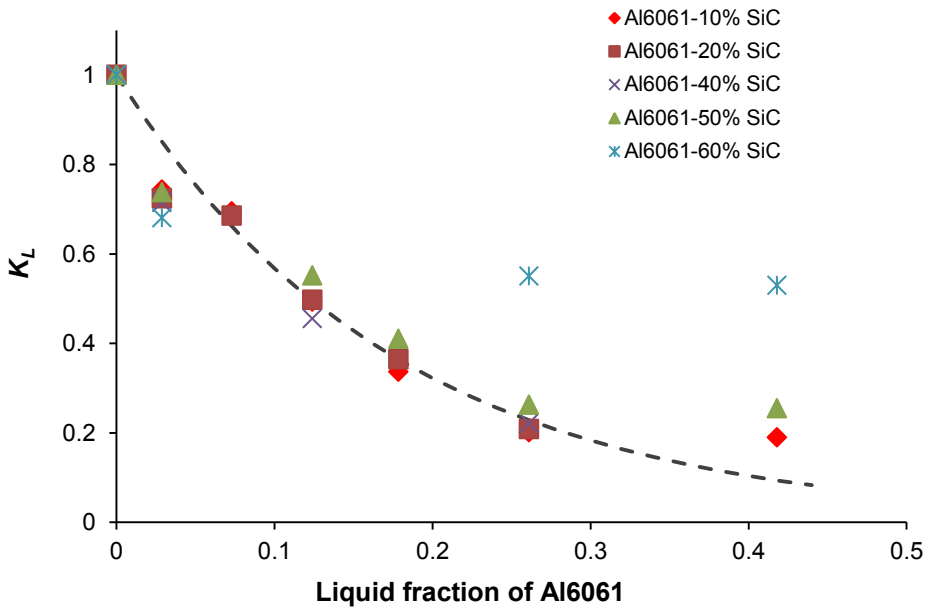

Fig. 3.9: K_L values at different Al6061 liquid fraction for various SiC volume fraction

3.3.5 Compaction of the powder mixture at high liquid fraction region

The relative density of the Al6061-50vol.%SiC composites compacted with different Al6061 liquid fraction is shown in Fig. 3.10. The compaction pressures for all the experiments were 150 MPa. When the liquid fraction in Al6061 was below 50%, the final relative density of the composites increased as the liquid fraction of Al6061 increased. The addition of liquid significantly assisted the densification of the powder

mixture, and near full density can be obtained. However, lower densities were obtained when the liquid fraction of Al6061 was larger than 50%. A large amount of liquid was squeezed out during the compaction.

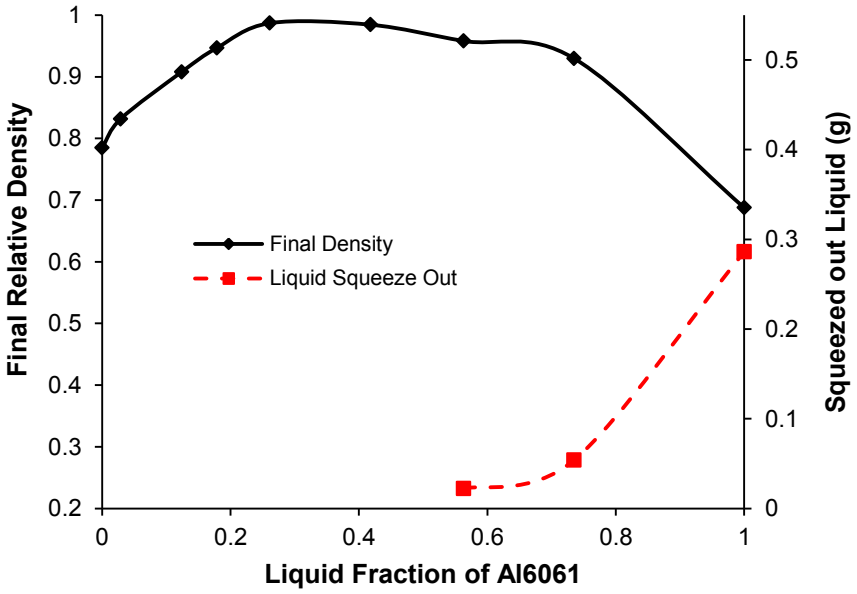

Fig. 3.10: Relative density of the Al6061-50vol.%SiC composite and liquid squeezing out amount during compaction. Compaction pressure was 150 MPa for all compactions.

Fabrication of high volume fraction SiC reinforced metal composites by compacting powders in the semi-solid state has advantages compared with casting, infiltration and powder metallurgy routes. High composite density can be obtained with relative low pressure at relative low temperature by compacting powder mixture in the semi-solid state. Pressureless infiltration was restricted by a limited infiltration distance, and relative high porosity was obtained (e.g. 7% for Al-60SiC (Candan, Ahlatci et al. 2001)). High density can be obtained by squeeze casting process (to 99% for Al-(50-60)SiC (Lee, Jeon et al. 2000; Lee and Hong 2003); however, multistep processing

(preform preparation and infiltration) and high temperature were required. For hot pressing and sintering process, long high temperature holding time and ceramic particle percolation will result in relative high material porosity and manufacturing cost (Watari 1997; Lin 1999).

3.4 Conclusion

The compaction behavior of Al6061-SiC powder mixture with 0-60vol.% reinforcement involving Al6061 liquid-phase was investigated. The temperature ranged from 550°C to 660°C where the liquid fraction of Al6061 ranged from 0 to 100%. The effects of the Al6061 liquid fraction and SiC volume fraction on the compaction behavior were investigated. The reinforcement factor K_R was significantly affected by the Al6061 liquid fraction and the SiC volume fraction. When the SiC volume fraction was low (<30%), the reinforcement factor K_R was similar across all liquid fraction range, while K_R was higher when f_L was greater than 10%. When the SiC volume fraction is high (>30%), the Al6061 liquid fraction determined the starting value of K_R. The liquid factor K_L decreased as the liquid fraction of Al6061 increased up to 30%. The variation of K_L for different SiC volume fraction at the same liquid content was small, and therefore, the K_L can be expressed with a simple equation only function of on the liquid fraction of Al6061.

CHAPTER 4 FABRICATION OF AL6061 COMPOSITE WITH HIGH SIC PARTICLE LOADING BY SEMI-SOLID POWDER PROCESSING

4.1 Introduction

SPP combines the advantages of powder metallurgy and semi-solid forming (Spencer, Mehrabian et al. 1972; Backman 1977; Kumar, Martin et al. 1993; Lee 1997; Steinhoff, Weidig et al. 2004; Kim, Koc et al. 2007; Kim, Ni et al. 2007). In contrast to traditional bulk semi-solid forming, the process enables the mixing of various powders for improved properties and eliminates post-processing steps required for powder metallurgy routes. A summary of various processing routes of SPP investigated by other researchers is shown in Fig. 4.1 (Young and Clyne 1986a; Young and Clyne 1986b; El Wakil 1992; Zu and Luo 2001; Hamilton, Zhu et al. 2003; Chen, Yang et al. 2004; Chen, Yang et al. 2005b; Chen, Yang et al. 2005a; Luo, Cheng et al. 2005; Luo, Cheng et al. 2006). In general, four basic steps are involved in SPP: powder preparation, powder precompaction, heating and semi-solid forming. SPP has been applied to produce net-shaped MMCs with low reinforcement loading (<30%). Previous work has demonstrated the potential to produce composites with high efficiency, low cost and good compositional control with promising microstructures (Yasue 2000; Wen 2001; Wildgoose, Banks et al. 2006; Wu, Kim et al. 2010b).

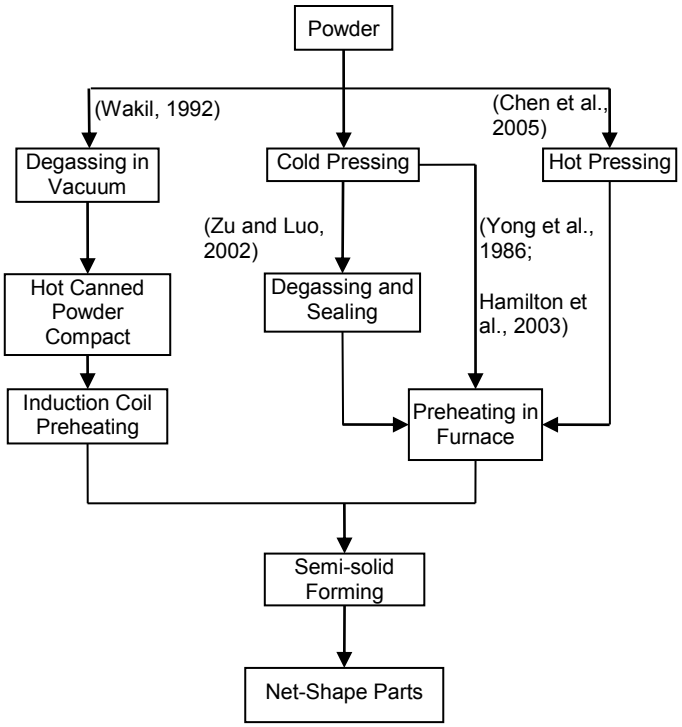

Fig. 4.1: Various processing routes of semi-solid powder processing

Although it has been more than 20 years since the introduction of SPP, no in-depth research has been conducted concerning high reinforcement loading conditions above 45 vol.%. Metals reinforced with high reinforcement loading are very attractive due to the modified properties such as high modulus and strength, low coefficient of thermal expansion, and improved thermal conductivity (Ibrahim, Mohamed et al. 1991; Fan 1998; Miserez, Muller et al. 2004). Methods including infiltration (Kouzeli, Weber et al. 2001; Prater 2006; Zhang, Qu et al. 2008), casting (Qin, Chen et al. 1999; Jeong, Seo et al. 2005; Pham, Yoon et al. 2007), and powder metallurgy (Cerit, Karamis et al. 2008) have been investigated to fabricate MMC reinforced with high ceramic loadings. Several limitations were discussed as to the fabrication of high ceramic loading MMCs, such as difficulty in compositional control in casting, sintering balance (Kawasaki 1997)

and ceramic powder percolation (Watari 1997; Lin 1999) in powder metallurgy, and closed and half closed pore problems in infiltration casting (Corbin 1999; Pech-Canul 2002; Pech-Canul, Parras-Medecigo et al. 2002; Cho, Choi et al. 2004; Song, Park et al. 2007).

In this study, a matrix phase of Al6061 reinforced by silicon carbide (SiC) particles was used to understand the synthesis of composites with reinforcement loadings above 45 vol.% by SPP. Theoretical SiC loading limit of the SPP has been proposed and discussed. In addition, effects of processing parameters, which include SiC loading, applied pressure and matrix-reinforcement particle size, on microstructure and hardness have been studied.

4.2 Experimental Procedures

The Al6061 powders and SiC particles were prepared by blending in a powder mixer (SPEX 8000M) for eight minutes. The chemical composition of Al6061 powders obtained from Valimet Inc. is shown in Table 4.1. The size and distribution of Al6061 and SiC particles (AEE Inc.) are summarized in Table 4.2. The experimental setup for heating and compression is shown in Fig. 4.2. The die and powders were heated in the furnace (Applied Test System Inc), while the load and movement of upper ram were controlled and measured by the materials testing system (TestResources Inc, 800LE). After weighing and pouring the blended powder mixture, the die set was placed in the furnace. Once the material was heated to 640 °C, the upper ram moved down at a

designed velocity and compressed the semi-solid powder compact. Experimental conditions are summarized in Table 4.3.

Table 4.1: Chemical composition of Al6061 (Valimet, Inc.)

Element	Cr	Cu	Fe	Mg	Mn	Si	Ti	Zn	Al
Amount (%)	0.09	0.28	0.27	1.03	0.03	0.52	0.01	0.06	Bal.

Table 4.2: Powder size and distribution of Al6061 and SiC powders

Powder type	Powder Size (μm)	Size Distribution (μm)		
		d_{90}	d_{50}	d_{10}
Al6061(L)	44 - 105	99.77	66.06	44.65
Al6061(S)	5-23	22.97	13.82	5.67
SiC(L)	65			
SiC(S)	10			

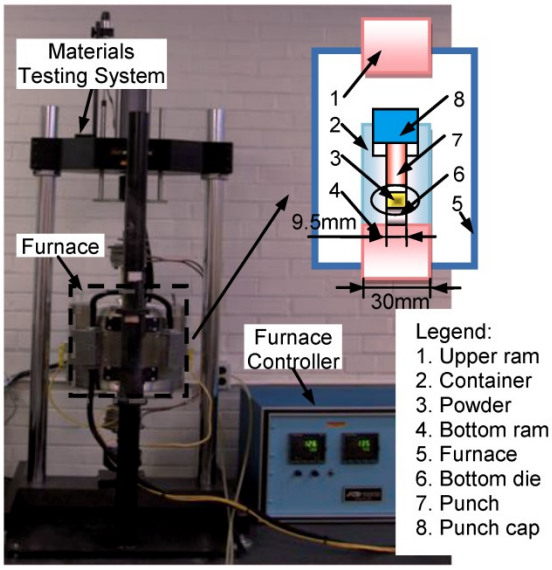

Fig. 4.2: Experiment setup for semi-solid powder forming

Table 4.3: Experiment settings

Parameter	Settings
Forming Pressure (MPa)	50, 100
Pressure Holding Time (s)	30
SiC Loading (vol%)	45.8, 55.9, 66.3
Punch Velocity (mm/s)	0.065
Operating Temperature (°C)	640
Liquid Fraction of Al6061	0.3
Powder Size	Listed in Table 4.2

Experiments were performed to understand the effects of matrix and reinforcement particle size, reinforcement loading, and applied pressure on the microstructure and mechanical properties (see Table 4.4). Runs No. 16–18 were

performed to test the compaction curve of Al6061-only and SiC-only particles at elevated temperatures. The microstructures of the samples were observed with an optical microscope (Zeiss, Axiovert 200M) and scanning electron microscope (JEOL JSM-606LV). Hardnesses of samples were measured by LECO LM247AT Micro Hardness Tester after appropriate polishing procedure. A Siemens D-500 X-ray diffraction system was used to obtain the X-ray diffraction pattern of the powder and composite samples.

Table 4.4: Experiment array and results

Run No.	SiC vol%	SiC size (μm)	Al6061 size (μm)	P (MPa)	Hardness (HV)	Density (g/cm^3)	Theoretical Density (g/cm^3)	Relative Density
1	45.8	65	14	50	151	2.74	2.93	0.935
2	55.9	65	14	50	95	2.79	2.98	0.937
3	66.3	65	14	50	95	2.67	3.03	0.879
4	45.8	65	14	100	150	2.92	2.93	0.998
5	55.9	65	14	100	146	2.85	2.98	0.958
6	66.3	65	14	100	127	2.72	3.03	0.896
7	45.8	12.5	14	50	153	2.73	2.93	0.932
8	55.9	12.5	14	50	86	2.61	2.98	0.874
9	66.3	12.5	14	50	42	2.44	3.03	0.803
10	45.8	12.5	14	100	176	2.78	2.93	0.969
11	55.9	12.5	14	100	155	2.71	2.98	0.898
12	66.3	12.5	14	100	67	2.42	3.03	0.833
13	45.8	12.5	66	100	157	2.84	2.93	0.950
14	55.9	12.5	66	100	135	2.68	2.98	0.909
15	66.3	12.5	66	100	47	2.53	3.03	0.797
16	0	0	66	50	47	2.74	2.71	
17	100	12.5						
18	100	65						

A separate experiment was performed to verify the actual temperature of the powder inside the die assembly during the forming process. To reduce the overall heating time, the heating curve as shown in Fig. 4.3 was used. The powder inside the die reached target temperature of 640 °C after 60 minutes of heating, and all the experiments were conducted 65 minutes after the start of heating.

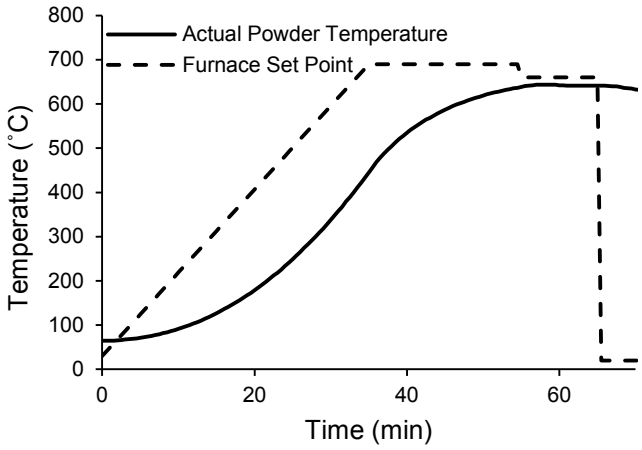

Fig. 4.3: Heating curve used in the experiment

4.3 Results and Discussion

The compaction curves of SPP are analyzed to understand the synthesis mechanism of Al6061-SiC composite and the SiC loading limit. Then, effects of processing parameters on the composite microstructure, hardness and fracture surface are discussed. In addition, presence of aluminum carbide (Al_4C_3) is checked with X-ray diffraction analysis.

4.3.1 SiC Loading Limit

A schematic of particle evolution during compaction of relatively soft matrix phase (Al6061) and hard reinforcement phase (SiC) is shown in Fig. 4.4. The powders are first loosely stacked in the die (Fig. 4.4(a)). As the pressure is applied in the semi-solid temperature range of the matrix, the blended powder is gradually compacted as observed in the initial compaction curve of Fig. 4.5. As the pressure is further increased, the SiC particles rearrange and form a structural network for high loading conditions (Fig. 4.4(b)). Soft matrix phase and hard SiC particles break and abruptly rearrange. This phenomenon is observed by the discontinuous change or disruption in the loading curves shown in Fig. 4.5. The disruption during the compaction is delayed in powders with higher SiC loading conditions. Depending on the amount of metal matrix, a dense structure as shown in Fig. 4.4(c)-Area (A), or porous structure as represented by Area-(B) can be formed. If there is enough matrix material to fill the pore structure formed by the hard SiC structure, a dense structure may be formed; otherwise, porous composite structure will be obtained.

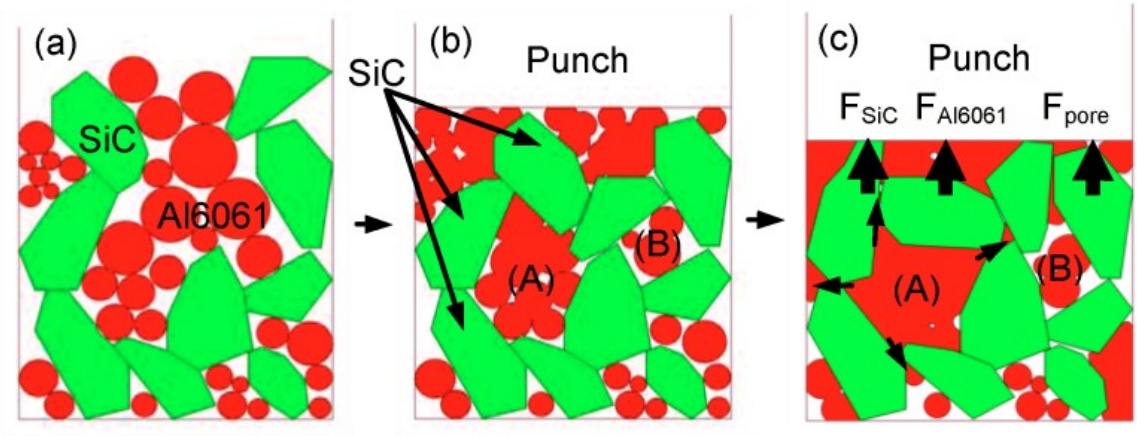

Fig. 4.4: Al6061-SiC compaction mechanism

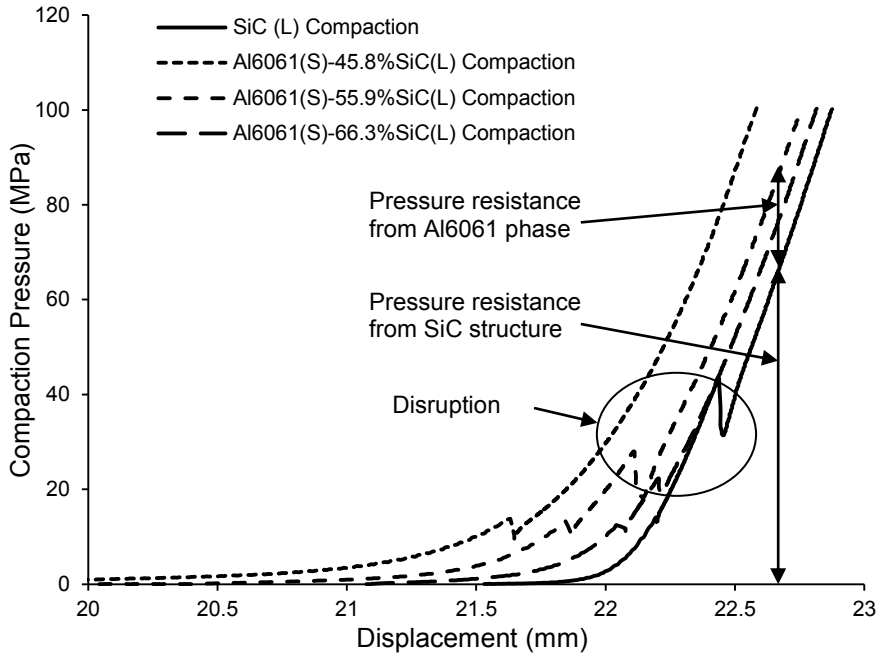

Fig. 4.5: Compaction curves of Al6061-SiC and SiC-only powders at 640 ˚C

As represented in Fig. 4.4(c) and in Eqn. (4.1), three sources, i.e. reinforcement phase, matrix phase and pores, contribute towards the total force acting on the punch. Since the force from pore is negligible, Eqn. (4.1) can be simplified to Eqn. (4.2), which shows the contributing pressure terms from each phase. At elevated temperatures in

semi-solid regime, most of the load will be undertaken by the hard reinforcement phase since the matrix phase is in the mushy state.

$$F_T = F_{SiC} + F_{Al6061} + F_{pore} \tag{4.1}$$

$$P_T = P_{SiC}\frac{A_{SiC}}{A_T} + P_{Al6061}\frac{A_{Al6061}}{A_T}, \quad where\ A_T = A_{SiC} + A_{Al6061} + A_{pore} \tag{4.2}$$

F_T, P_T and A_T are the total compression force, total pressure and total area, respectively; F_{SiC}, F_{Al6061} and F_{pore} are the force undertaken by SiC phase, Al6061 phase and pores, respectively; P_{SiC} and P_{Al6061} are the pressure contribution from SiC phase and Al6061 phase, respectively. A_{SiC}, A_{Al6061} and A_{pore} are the contact area between the punch and each phase.

To understand the pressure contribution from each phase, a separate experiment with SiC(L)-only compaction curve was compared with that of Al6061-SiC(L) in Fig. 4.5. All the curves had the same SiC mass loading. Taking the Al6061-55.9% SiC(L) and SiC-only compaction curves as an example, the SiC(L)-only compaction curve represents the fractional amount of pressure applied by the hard SiC phase, while the difference between the two curves is the pressure contribution from the soft matrix phase at a given punch displacement. As the SiC loading increased, less loading support from Al6061 phase was observed during the compaction. This is observed by merging of the compaction curves of higher SiC loaded powders to that of the SiC-only powder in Fig. 4.5. For a given total pressure, one can assume that the limit of SiC loading occurs when there is no pressure contribution from the Al6061 phase. In other words, SiC-only loading represents an ideal condition where there is no pressure contribution from the

matrix phase and the matrix phase is only filling the cavity created by the SiC structure. Therefore, the maximum SiC loading volume applicable for the Al6061 composite can be obtained from SiC-only curve in Fig. 4.5 by calculating the density at given displacement. The resulting maximum loading curves for large and small SiC particles are shown in Fig. 4.6 and summarized in Table 4.5. It is interesting to note that one can achieve higher SiC loading with larger SiC particle sizes for a given pressure. At 100 MPa, over 50 vol.% loading of SiC can be achieved theoretically.

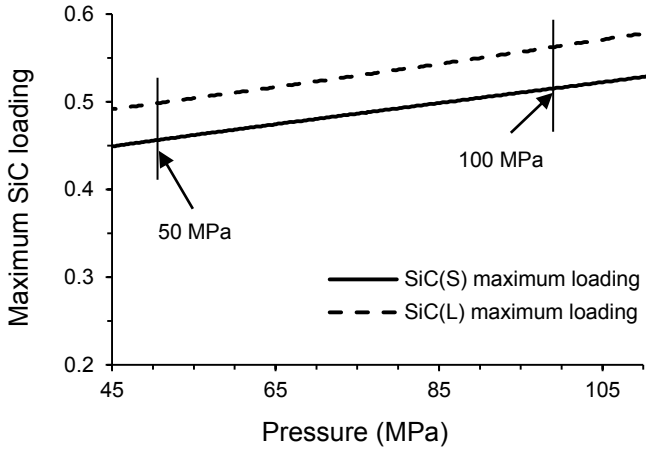

Fig. 4.6: Maximum SiC vol% loading versus compaction pressure for SiC particle sizes of 10 and 65 μm.

Table 4.5: Maximum SiC loading at selected pressure settings

Condition		Maximum SiC loading
Pressure (MPa)	SiC Size (μm)	vol%
50	12.5	45
	65	49
100	12.5	51
	65	58

4.3.2 Microstructure

The relative particle size of the matrix and reinforcement phases had significant influence on the obtained microstructures. Microstructure images of composites with loading conditions of 45.8 and 66.3 vol.% SiC are shown in Fig. 4.7. The composite with 45.8% SiC loading at higher pressure setting showed well-densified microstructures (Fig. 4.7(a), (b) and (c)), while pores were observed for samples fabricated with 66.3% SiC loading (Fig. 4.7(d), (e) and (f)). A more uniform distribution of SiC was achieved when larger SiC powder was used (Fig. 4.7(a) and (b)). When the Al6061 size is much larger than the SiC particle, locally agglomerated Al6061 was observed (Fig. 4.7(c)). This can be explained by the initial Al6061 and SiC particle distribution from the blending procedure before compaction. As shown in Fig. 4.8(a), when the 10 μm SiC particles were blended with similar size Al6061 particles (14 μm), the blending resulted in a homogeneous mixture. Similarly, when smaller matrix phase particles (Al6061, 14 μm) were blended with larger SiC particles (65 μm), a well-densified microstructure was obtained. On the other hand, when 10 μm SiC particles were used, which was substantially smaller than Al6061 particles, the SiC particles agglomerated and surrounded the larger Al6061 powders (see Fig. 4.8(c)). With insufficient amount of pressure, this resulted in large liquid Al6061 area (Fig. 4.7(c)) or microstructures with poor bonding containing large pores (Fig. 4.7(f)). This also resulted in higher SiC fractions in the rest of region like Area-(B) in Fig. 4.7(c) and caused the formation of pores in these areas. Consequently, samples with lower relative density and inferior structural integrity are likely to result from such conditions. This explains higher relative

density obtained for the samples with smaller Al6061 particles under the same pressure, SiC size and reinforcement loading (see Table 4.4).

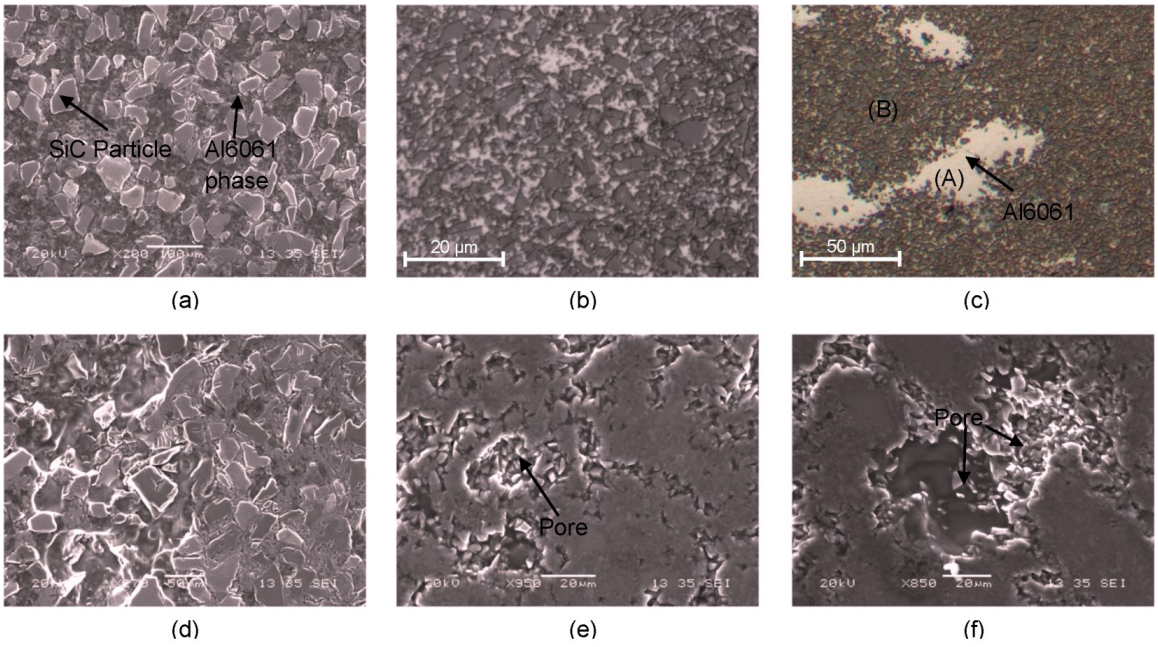

Fig. 4.7: Microstructure images of composites with 45.8 and 66.3 vol% SiC. Experimental conditions are: (a) 100 MPa, Al6061(S)-45.8% SiC(L); (b) 100 MPa, Al6061(S)-45.8% SiC(S); (c) 100 MPa, Al60061(L)- 45.8% SiC(S); (d) 50 MPa, Al6061(S)-66.3% SiC(L); (e) 50 MPa, Al6061(S)- 66.3% SiC(S); and (f) 100 MPa, Al6061(L)- 66.3% SiC(S). Note that (b) and (c) are optical images; (a), (d),(e) and (f) are SEM images.

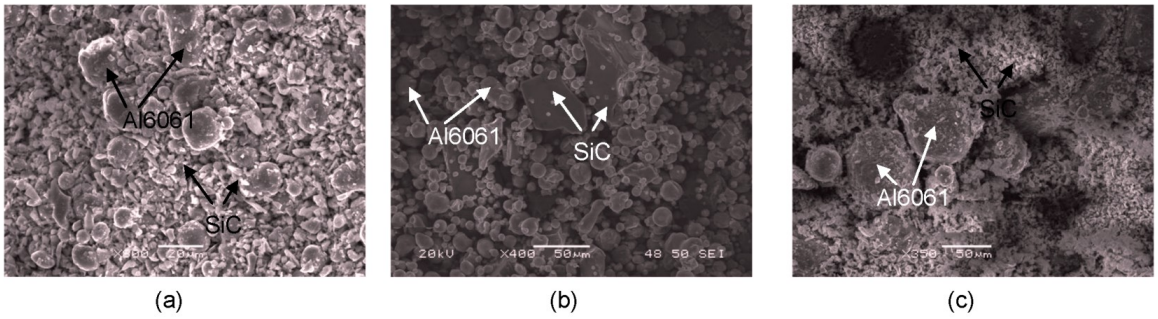

Fig. 4.8: Distribution of Al6061 and SiC (45.8%) powders after blending: (a) Al6061(S) with SiC(S); (b) Al6061(S) with SiC(L); and (c) Al6061(L) with SiC(S)

There were also other irregularities and non-uniform structures observed in the composite. At 640 ˚C, about 30% of Al6061 is in the liquid-phase (Jeng and Chen 1997; Kim, Kang et al. 2007). Therefore, due to the solidification shrinkage—the density of liquid Al is lower than that of the solid Al—micro-cracks were observed in the composites that had large SiC particles. Since the SiC structure is much stronger, cracks formed when the sample cooled (see Fig. 4.9(a)). When the SiC size was smaller, no shrinkage cracks were observed (see Fig. 4.9(b)). It seemed that the smaller SiC particles were able to adjust to the shrinkage during the solidification.

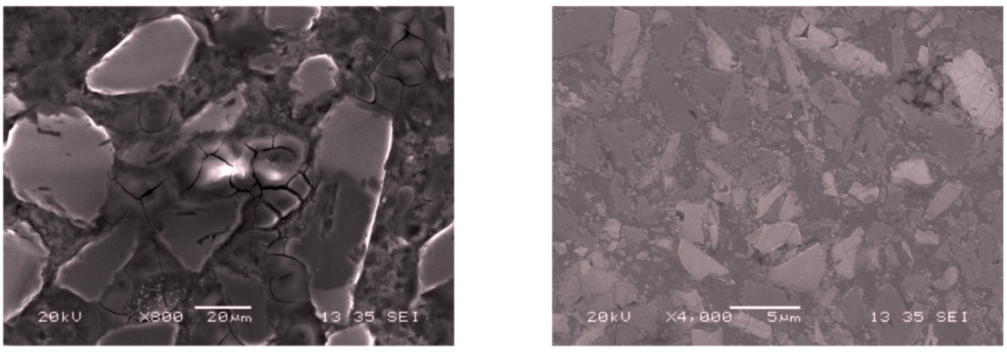

(a) (b)

Fig. 4.9: SEM images showing the polished composite surface: (a) Al6061(S)-45.8% SiC (L), 100 MPa; (b) Al6061(S)-45.8% SiC (S), 100 MPa;

4.3.3 Hardness

The micro-hardness test results are shown in Fig. 4.10. As shown in Fig. 4.10 (a), the Al6061 showed relatively high hardness when the samples were reinforced with 45.8 vol% SiC. Moreover, it was observed that all the samples reinforced with small SiC(S) particles resulted in higher hardness than those reinforced with large SiC(L). In the ceramic reinforced MMCs, the reinforcement effect on the mechanical properties of the

composite is influenced by the reinforcement phase geometry, the bonding strength between the matrix and reinforcement phases, and the total contact area between the phases (Ramakrishnan 1996; Chawla, Jones et al. 1998; Qin, Chen et al. 1999). When SiC particle size is smaller, the contacting area between the ceramic and matrix phases is much larger, which provides better strengthening effect. In addition, the small SiC particles were able to penetrate into the Al6061 particle, creating fresh contact between the Al6061 and SiC phase. Therefore, higher hardness was obtained for composites reinforced with smaller SiC particles when compared with composites with larger SiC particles having the same loading.

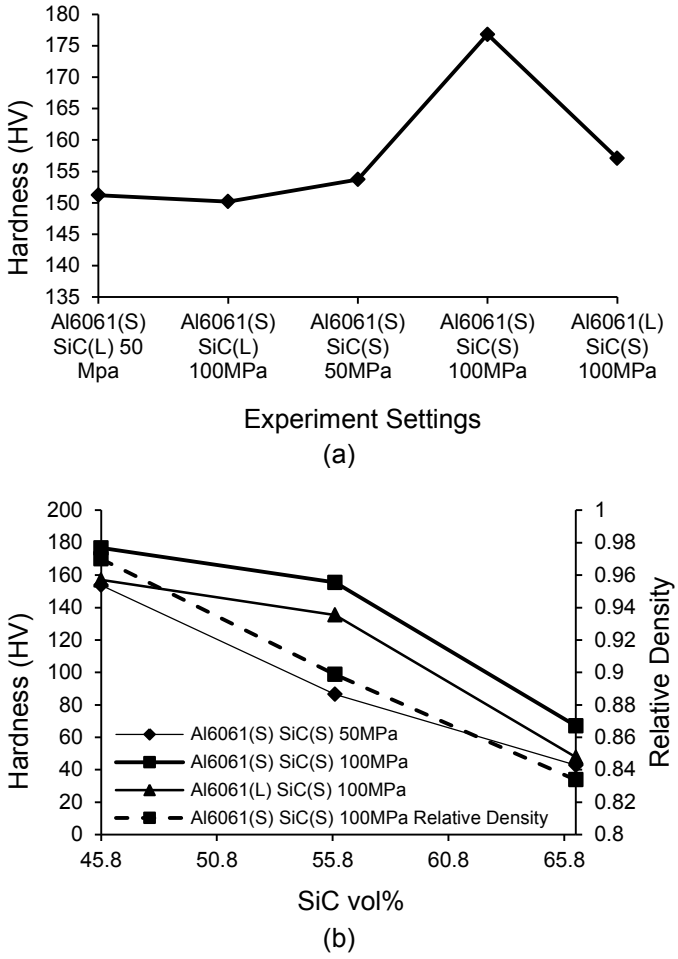

Fig. 4.10: Microhardness test results: (a) Hardness of sample with 45.8 vol.% SiC; and (b) comparison of hardness at different process settings

In Fig. 4.10(b), increase in the hardness was observed when higher pressure was applied. This is simply due to the higher relative density obtained with higher pressure. Although the reinforcement loading increased, the hardness of the composite decreased. Since 55.9 and 66.3% loadings were beyond the maximum loading limit of the composite with small SiC(S) particles, decrease in the relative density, which indicated significant pore formation, was observed. Because of the non-uniformly distributed SiC and Al6061 (see Fig. 4.7(c)), the samples fabricated with small SiC and large Al6061 powders have lower hardness compared with those of small SiC and small Al6061. In addition, The

non-uniform distribution of SiC and Al6061 phase causes the local hardness variation in the composite. The local hardness was measured at Al6061-concentrated area (e.g. Fig. 4.7(c)-Area (A)) and SiC-agglomerated area (e.g. Fig. 4.7(c)-Area (B)) in the samples made from large Al6061 and small SiC particles. As shown in Table 4.6, the hardness of the Al6061-concentrated area and SiC-agglomerated area was significantly different. When the SiC loading was low (45.8%), the hardness of the SiC-agglomerated area (182.0 HV) was nearly twice as that of the Al6061-concentrated area (95.1 HV). However, when the SiC loading was high (66.3%), the hardness of the SiC-concentrated area was only 38.4 HV, which was even lower than the Al6061-concentrated area. The agglomeration of SiC particles and insufficient amount of matrix phase resulted in poor bonding in these regions.

Table 4.6: Local hardness measurement of the composite made from Al60061(L)-SiC(S)

SiC Loading	Al6061 Area (HV)	SiC Area (HV)
45.8%	95.1	182.0
55.9%	100.3	149.2
66.3%	69.7	38.4

4.3.4 Fracture Surface

The SEM images of the fracture surfaces are shown in Fig. 4.11. Samples with lower SiC loading showed a good bonding between the SiC and Al6061 (see Fig. 4.11(a), (b) and (c)). In Fig. 4.11(b), no obvious boundary between SiC and Al6061 matrix can be found. It was speculated that the fracture occurred within the matrix phase rather than

the interface. However, when the SiC loading increased, there was not enough Al6061 phase to completely fill the porous network formed by the SiC phase (see Fig. 4.11(e) and (f)). Therefore, the bonding between SiC and Al6061 became weaker as the SiC increased beyond the maximum loading limit. In addition, the fracture surface of the composite made from small SiC and large Al6061 particles exhibited distinct characteristic due to the non-uniform distribution of the SiC phase. As shown in Fig. 4.11(c) and (f), the Al6061 areas showed ductile fracture surface, while the SiC-agglomerated areas had less ductility.

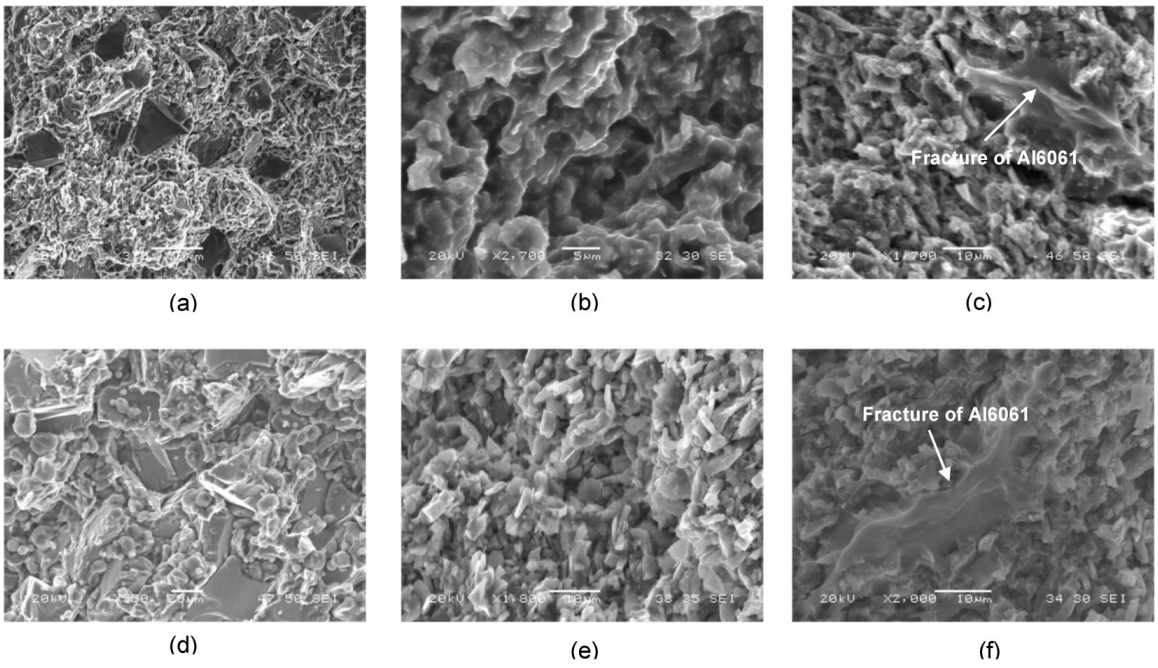

Fig. 4.11: SEM images of fracture surfaces of Al6061-SiC composite. Experiment conditions are: (a) 100 MPa, Al6061(S)-45.8% SiC(L); (b) 100 MPa, Al6061(S)-45.8% SiC(S); (c) 100 MPa, Al60061 (L)-45.8% SiC(S); (d) 50 MPa, Al6061(S)- 66.3% SiC(L); (e) 50 MPa, Al6061(S)- 66.3% SiC(S); and (f) 100 MPa, Al6061(L)- 66.3% SiC(S);

4.3.5 Formation of Al_4C_3

SiC particles may react with liquid aluminum at high temperatures and form Al_4C_3 via the reaction pathway in Eqn. (4.3) (Lee 1997; Fan 1998; Tham, Gupta et al. 2001). Due to the brittleness of Al_4C_3, its formation can significantly affect the interfacial bonding strength between the Al6061 matrix and SiC reinforcement. Therefore, the formation of aluminum carbide should be avoided during the fabrication process. X-ray diffraction (XRD) measurements were conducted on blended Al6061 and SiC powders (Fig. 4.12(a)) and fabricated Al6061-SiC composites (Fig. 4.12(b)). As shown in Fig. 4.12(b), only peaks induced by Al and SiC were found, which corresponds to the XRD pattern obtained from the blended Al6061-SiC powders (Fig. 4.12(a)). No obvious peaks for Si and Al_4C_3 (noted by the arrows in Fig. 4.12 (b)) were observed. One of the reasons is that the temperature applied during the SPP is relatively low compared with casting, which requires complete melting of the matrix phase. If Al_4C_3 is at all present, the amount is smaller than what can be measured by conventional XRD method (approximately 5 vol.%).

$$4Al(l)+3SiC(s)\text{-- } Al_4C_3(s)+3Si(s) \tag{4.3}$$

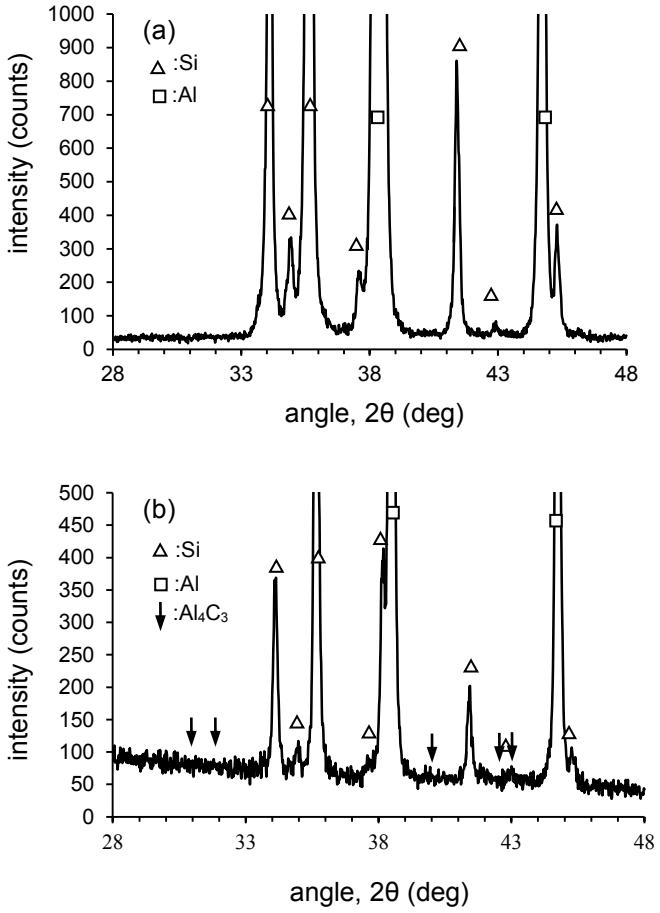

Fig. 4.12: X-ray diffraction spectra of (a) blended Al6061 and SiC powders, and (b) Al6061-SiC composite (Al6061(L)-45.8% SiC(S), 50 MPa). The arrows indicate peaks for Si and Al_4C_3 if they existed.

4.4 Conclusion

In this study, SPP was used to fabricate Al6061 composite reinforced with high volume loading of SiC particles. The compaction and synthesis mechanism of Al6061-SiC composite was discussed, and the SiC loading limit was analyzed. The effects of the reinforcement particle size, matrix particle size, reinforcement loading volume and pressure on the microstructure and mechanical properties were investigated.

SPP of Al6061 composite for high loading SiC conditions had the following characteristics. Since the compaction occurs in the semi-solid temperatures of the matrix phase, the compaction pressure was mainly undertaken by the SiC skeleton structure. Therefore, disruption of the powder structure was observed during the compaction. As the compression progressed, the partially melted Al6061 phase filled the pores created by the SiC structure. Moreover, a methodology was introduced to estimate the maximum loading limit of SiC particles in Al6061 composite from SiC-only compaction tests. Higher SiC loading limit was obtained for larger SiC particles and higher compaction pressure. The relative size of the initial Al6061 and SiC particles had significant effect on the microstructure, hardness and fracture surface of the composite. It required higher pressure to compact the composite containing smaller SiC particles, which reduce the SiC loading limit for a given pressure. In addition, non-uniform microstructure was obtained when the reinforcement particles were smaller than those of the matrix phase. This resulted in local variations in hardness and fracture surfaces. On the other hand, dense composite with smaller SiC particles resulted in higher hardness and uniform microstructures free of micro-cracks.

In this study, we have laid out a theoretical platform that can aid further understanding of SPP for high reinforcement loading conditions. Moreover, the composite structures obtained near the maximum loading limit demonstrated the feasibility of using SPP for the fabrication of high ceramic loading composites. As processing in the semi-solid regime combines the advantages of powder metallurgy and

forming, the process may provide new fabrication routes for near net-shape samples with locally tailored microstructures.

CHAPTER 5 MECHANICAL ALLOYING OF CARBON NANOTUBE AND AL6061 POWDER FOR METAL-CNT COMPOSITE

5.1 Nomenclature

a	weight fraction of the agglomerated CNTs	
A_b	average nominal area of a single particle	m^2
$A_{b,t}$	total nominal area of all particles	m^2
A_e	net area embedded during mechanical alloying	m^2
A_f	area exposed due to fracturing	m^2
A_w	area embedded due to welding	m^2
A_s	exposed surface area of all the particles	m^2
d	weight fraction of the dispersed CNTs	
f_e	weight fraction of the total embedded CNTs	
$f_{e,d}$	weight fraction of the embedded CNTs that are dispersed	
f_s	weight fraction of the total surface CNTs	
$f_{s,d}$	weight fraction of the surface CNTs that are dispersed	
g	normal distribution function of the CNT length	
G	cumulative distribution function of the CNT length	
h_c	thickness of powder coating the milling balls	m
I_b	ball impaction frequency	1/s
k	factor = $\Delta A_f / \Delta A_w$	
l	CNT length	μm

l_{all}	average overall CNT length	μm
l_e	fraction of effective impact during ball milling	
m	average number of impacts required for a particle to be struck once	
n_f	number of particles fractured in a short time period, Δt	
n_t	total number of particles during mechanical alloying	
n_w	number of particles welded in a short time period, Δt	
$n_{\Delta t}$	$= n_f + n_w$	
R_b	radius of the milling ball	m
t	time	s
v	ball impacting velocity	m/s
W_a	weight of agglomerated CNTs	g
W_d	weight of dispersed CNTs	g
W_e	weight of embedded CNTs	g
$W_{e,d}$	weight of embedded CNTs that are dispersed	g
W_s	weight of surface CNTs	g
$W_{s,d}$	weight of surface CNTs that are dispersed	g
W_t	weight of all CNTs	g
α	a factor = $A_s /(A_s+A_e)$	
$\dot{}$	change rate of parameter	
γ	a factor = $A_{b,t} / A_s$	
Δ	the change of parameter	
Γ	the frequency of effective impact	1/s

μ	the mean of the normal distribution of CNT length	μm
τ	average time required to effectively impact all the particles	s
ρ_b	the density of the milling ball	kg/m^3
ρ_p	the density of the powder	kg/m^3
σ^2	the variance of the normal distribution of CNT length	
$\phi(l,t)$	overall CNT length distribution at time *t*	
$\phi_s(l,t)$	surface CNT length distribution at time *t*	
$\phi_{s,d}(l,t)$	surface dispersed CNT length distribution at time *t*	
$\phi_e(l,t)$	embedded CNT length distribution at time *t*	

5.2 Introduction

The extraordinary properties of CNTs make them a potentially promising reinforcement material for polymers and metals (Zhong, Cong et al. 2003). In the fabrication of metal-CNT composites, dispersing the CNTs in the metallic matrix phase has been one of the critical challenges (Noguchi, Magario et al. 2004; He, Zhao et al. 2007). One of the most widely used approaches has been mechanical alloying, which has been shown to effectively disperse the CNTs in various metal-CNT composites (Liao, Tan et al. ; Esawi and Morsi 2007; Morsi and Esawi 2007; Poirier, Gauvin et al. 2009; Wang, Choi et al. 2009). The resultant composites were reinforced by both the CNTs and the refinement of grains (Bakshi, Lahiri et al. 2010). However, the high energy input during the mechanical alloying process often breaks the CNTs and introduces defects in them (Bakshi, Lahiri et al. 2010). Sometimes the defect sites facilitate reactions between

the CNTs and the metallic phase, enhancing their bonding characteristics (Perez-Bustamante, Gomez-Esparz et al. 2009; Poirier, Gauvin et al. 2009). On the other hand, shortening CNTs by breakage may diminish the effectiveness of adding CNTs as a reinforcement phase. Studies on CNT breakage during mechanical alloying reported findings ranging from minimal breakage (Deng, Zhang et al. 2007; Esawi and Morsi 2007) to severe damage (Zhou, Zhang et al. 2007; Poirier, Gauvin et al. 2009). Due to the challenges in extracting and measuring the nanoscale dimensions of CNTs, no quantitative study on CNT breakage during mechanical alloying has been reported.

In this study, Al6061 powder and 1.0 wt.% CNTs were mechanically alloyed to analyze the CNT breakage. The CNTs on the particle surface were collected, and the CNT length and distribution were measured for different mechanical alloying durations. Because of the difficulty in collecting the CNTs embedded inside the particles, a mathematical model was developed to predict the overall CNT length and distribution during the mechanical alloying process.

5.3 Experimental Procedure

Al6061 particles (Valimet Inc.) and multi-walled CNTs from NanoLab® were used. The Al6061 particle and CNT information are summarized in Table 5.1. Two 12.7 mm diameter zirconia balls and the mixture of 2.97 g of Al6061 powder and 0.03 g of CNTs were placed in a 60 ml zirconia jar for mechanical alloying. The powders were mechanically alloyed in a high-energy SPEX 8000M mixer at a rotational speed of 1200

rpm for 3, 10, 20, 30, 40 and 60 mins, respectively. After the powders were mechanically alloyed, 40 ml of alcohol (99.9%) was introduced, and the powder-alcohol mixture was ultrasonicated for one hour. The CNTs detached from the Al6061 particle surface and floated in the alcohol solution. Several drops of the CNT-alcohol solution were separated and diluted until the CNTs dispersed under ultrasonic vibration. One or two droplets of the diluted alcohol-CNT solution were placed on an aluminum foil and dried naturally. The CNTs dispersed uniformly on the aluminum foil, and the morphology of the CNTs was analyzed. For the synthesis of Al6061-CNT composite, a semi-solid powder processing technique was employed. The composite was formed at 640ºC at which temperature the liquid fraction of Al6061 was about 30% (Kim, Kang et al. 2007). A pressure of 50 MPa was held for 30 minutes for consolidation of the composite. The detailed processing conditions can be found in the next Chapter. The morphology of the mechanically alloyed powders, the CNTs on the aluminum foil, and the microstructures of the composites were examined by scanning electron microscopy (JEOL JSM-606LV) and optical microscopy (Zeiss, Axiovert 200M). The lengths of CNTs were measured with software ImageJ by estimating the curves as segmented lines.

Table 5.1: Particle size and distribution of Al6061 and SiC powders

Constituent	Size (μm)	Size Distribution (μm)		
		d_{90}	d_{50}	d_{10}
Al6061	5-23	22.97	13.82	5.67
Multi-walled CNT	20-50 nm in diameter, 5 μm in length			

5.4 Theoretical Analysis

A mathematical model was developed to predict the overall CNT length during the alloying process. The overall CNT length was obtained by considering the effects of particle welding and fracturing on the CNT length evolution process. With the collected experimental data, including the surface CNT length and length distribution, particle surface area, and embedded area, the overall CNT length can be predicted. A schematic of the ball milling process for CNT and metallic powder is illustrated in Fig. 5.1. Five assumptions have been postulated as the following:

(i) Only the dispersed CNTs can be embedded during the mechanical alloying process. Agglomerated CNTs will prevent the bonding between the metal particles (Wang, Choi et al. 2009). Therefore, it is unlikely that the agglomerated CNTs can be embedded, or it will be released soon after embedding.

(ii) The length distribution of the dispersed CNTs on particle surface ($\Phi_{s,d}$) is assumed to be similar to that of all the CNTs (dispersed and agglomerated) on the particle surface (Φ_s). It is difficult to experimentally measure the length distribution of dispersed CNTs separately from that of all the CNT on the particle surface. Theoretically, the CNTs on the surface, dispersed or agglomerated, experience the same amount of energy input from mechanical alloying in given amount of time. Thus, the length reductions are assumed to be similar to all CNTs on the surface:

$$\Phi_{s,d}(t) = \Phi_s(t) \tag{5.1}$$

(iii) The exposed CNTs and embedded CNTs are uniformly distributed on the surface area and embedded area, respectively.

(iv) The particles are uniformly deformed during the mechanical alloying process.

(v) During a single welding or fracturing event, only two particles are involved—a single particle is fractured into two, and two particles are welded into a single particle.

The details will be discussed in the subsequent sections.

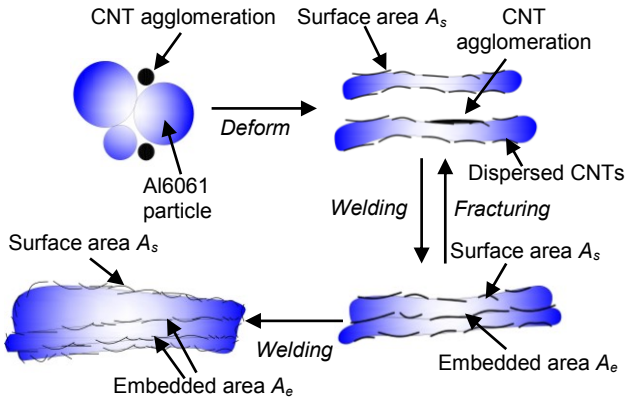

Fig. 5.1: Schematics of particles in mechanical alloying process.

5.4.1 Dispersion of CNTs

The fraction of agglomerated CNTs over all the CNTs in the composite is defined as a:

$$a = \frac{W_a}{W_t} \tag{5.2}$$

where W_a and W_t are the weights of agglomerated CNTs and all CNTs in the composite, respectively. Then, the dispersion, d, is defined as:

$$d = 1 - a = \frac{W_d}{W_t} \tag{5.3}$$

where W_d is the weight of dispersed CNTs. In other words, as long as the CNTs do not form an agglomeration, they are regarded as dispersed CNTs. d varies between 0 and 1, where $d = 0$ means all the CNTs are agglomerated, and $d = 1$ means all the CNTs have been dispersed.

W_s is the weight of CNTs on the particle surface; thus, the fraction of surface CNTs to the total CNT weight is $f_s(t) = W_s/W_t$. Similarly, fractions of embedded CNTs are defined as $f_e(t)$, while the dispersed fraction of embedded CNTs is defined as $f_{e,d}(t)$. Therefore, the total CNT fractions become one:

$$f_e(t) + f_s(t) = 1 \tag{5.4}$$

According to Assumption (i), at any time, *t*, all the embedded CNTs are dispersed, i.e., $f_e(t) = f_{e,d}(t)$. We can also define the fraction of dispersed CNTs on the particle surface as $f_{s,d}(t)$, following the prior definition of CNT dispersion, *d*:

$$d(t) = f_{s,d}(t) + f_{e,d}(t) = f_{s,d}(t) + f_e(t) \tag{5.5}$$

5.4.2 Welding and Fracturing of Particles with CNTs

During the mechanical alloying process, fracturing and welding continuously take place. Welding of particles will increase the embedded area, while fracturing will expose some of the embedded area. The surface area, A_s, is defined as the exposed area of the particles. The surface area that was embedded during mechanical alloying is defined as embedded area, A_e (see Fig. 5.1). Considering a short time period, Δt, the change of

embedded surface area due to welding is $\Delta A_w(t)$, and the exposed surface area due to fracturing is $\Delta A_f(t)$. Then, the net change of embedded area can be calculated as:

$$\Delta A_e(t) = \Delta A_w(t) - \Delta A_f(t) \tag{5.6}$$

A positive $\Delta A_e(t)$ means that particles are becoming larger due to overall welding, and a negative value suggests that the fracturing of particles is dominating.

A flow chart summarizing the overall CNT length calculation procedure is shown in Fig. 5.2. With Assumption (iii), the change of embedded CNT weight in a short time period Δt can be obtained by:

$$\Delta W_e(t) = W_{s,d}(t)\frac{\Delta A_w(t)}{A_s(t)} - W_e(t)\frac{\Delta A_f(t)}{A_e(t)} \tag{5.7}$$

where $W_{s,d}(t)$ is the weight of dispersed CNTs on the particle surfaces. The first term in the right hand side of Eqn. (5.7) is the contribution from the dispersed CNTs from the surface, and the second term is the loss of the CNTs from fracturing. Consequently, the fraction change of embedded CNTs that are dispersed can be presented in the following form:

$$\Delta f_e(t) = \frac{\Delta W_e(t)}{W_t} = \frac{\Delta A_w(t)}{A_s(t)} f_{s,d}(t) - \frac{\Delta A_f(t)}{A_e(t)} f_e(t) \tag{5.8}$$

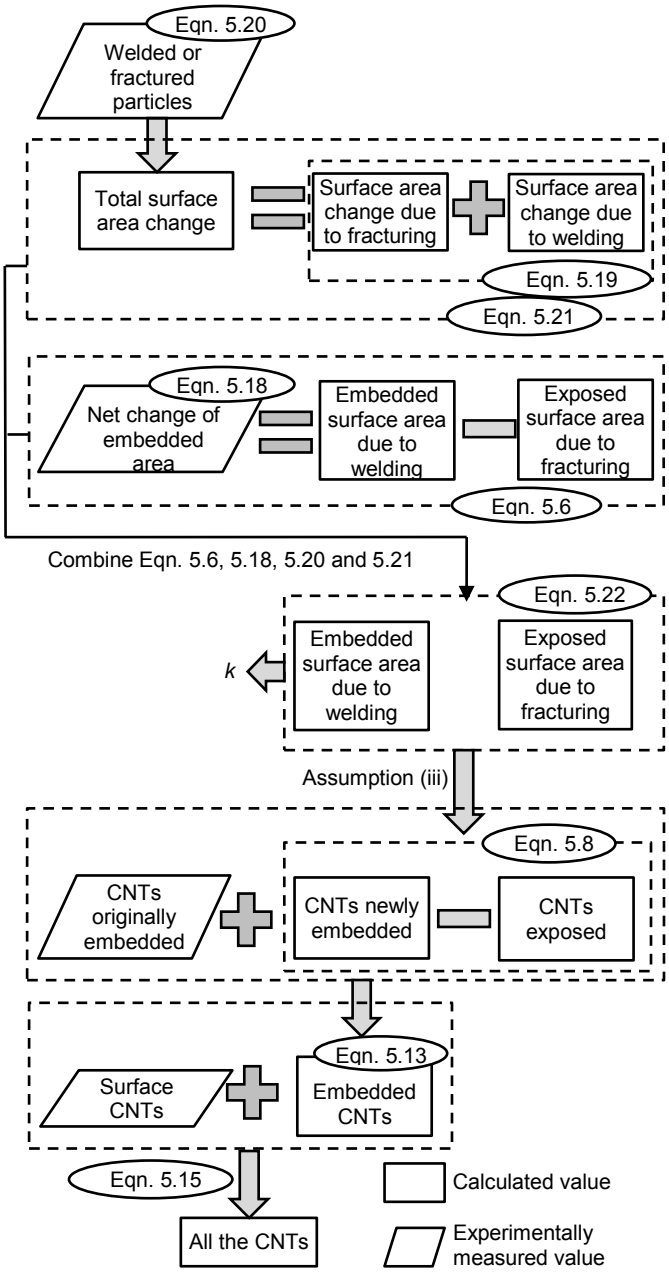

Fig. 5.2: Flow chart for mathematical calculation of CNT length

Statistically, given two probability density functions $p_1(x)$ and $p_2(x)$ and weights w_1 and w_2 such that $w_1>0$, $w_2>0$ and $w_1+ w_2=1$, the mixture distribution of $p_1(x)$ and $p_2(x)$, $f(x)$, can be calculated as (Everitt and Hand 1981):

$$f(x) = w_1 p_1(x) + w_2 p_2(x) \tag{5.9}$$

Therefore, the embedded CNT length distribution at $t+\Delta t$ can be represented by the mixture distribution of CNTs newly welded from the surface and leftover CNTs originally embedded inside the particle. The weights were calculated through the amount of newly welded CNTs from the surface (i.e. $\Delta A_w(t) f_{s,d}(t)/A_s(t)$) and leftover CNTs originally embedded inside the particle (i.e. $f_e(t)-\Delta A_f(t) f_e(t)/A_e(t)$). Thus, with Eqn. (5.1) we have:

$$\begin{aligned}\phi_e(t+\Delta t) = & \frac{\frac{\Delta A_w(t)}{A_s(t)} f_{s,d}(t)}{f_e(t) + \frac{\Delta A_w(t)}{A_s(t)} f_{s,d}(t) - \frac{\Delta A_f(t)}{A_e(t)} f_e(t)} \phi_s(t) \\ & + \frac{f_e(t) - \frac{\Delta A_f(t)}{A_e(t)} f_e(t)}{f_e(t) + \frac{\Delta A_w(t)}{A_s(t)} f_{s,d}(t) - \frac{\Delta A_f(t)}{A_e(t)} f_e(t)} \phi_e(t)\end{aligned} \tag{5.10}$$

As summarized in section 4.3, $\Delta A_e(t)$ can be determined:

$$\Delta A_e(t) = \frac{\alpha(t) - \alpha(t+\Delta t)}{\alpha(t)} A_s(t) \tag{5.11}$$

where $\alpha(t) = A_s(t)/(A_s(t) + A_e(t))$.

A factor k is introduced to simplify Eqn. (5.8) and is defined as:

$$k = \frac{\Delta A_f(t)}{\Delta A_w(t)} \tag{5.12}$$

Based on Eqns. (5.4), (5.6), (5.8), (5.11) and (5.12), the rate of $f_e(t)$ can be derived as the following:

$$\frac{df_e(t)}{dt} = \left(f_{e,d}(t) - d\right)\frac{1}{1-k}\frac{\frac{d\alpha(t)}{dt}}{\alpha(t)} + f_e(t)\frac{k}{1-k}\frac{\frac{d\alpha(t)}{dt}}{1-\alpha(t)} \tag{5.13}$$

Also, combining Eqn. (5.8) and (5.10), we can obtain:

$$\begin{aligned}\frac{d\left(\phi_e(t)f_e(t)\right)}{dt} &= \left(f_{e,d}(t) - d\right)\left(\frac{1}{1-k}\right)\frac{\frac{d\alpha(t)}{dt}}{\alpha(t)}\phi_s(l,t) \\ &+ \phi_e(t)f_e(t)\frac{k}{1-k}\frac{\frac{d\alpha(t)}{dt}}{1-\alpha(t)}\end{aligned} \tag{5.14}$$

The overall CNTs length distribution can be calculated with the following equation:

$$\phi(l,t) = \left(1 - f_e(t)\right)\phi_s(l,t) + f_e(t)\phi_e(l,t) \tag{5.15}$$

where $\phi(l,t)$, $\phi_s(l,t)$ and $\phi_e(l,t)$ are the overall CNT length distribution, surface CNT length distribution, and embedded CNT length distribution at time *t*, respectively.

5.4.3 Deformation of Particles

The particles continue to deform during the mechanical alloying, and therefore, the change of embedded area, $\Delta A_e(t)$, in a short time, Δt, is not equal to the surface area change, $A_s(t+\Delta t) - A_s(t)$. The simplified welding and fracturing mechanisms are shown in Fig. 5.3. In Fig. 5.3(a)–(c), the particle evolution process is manually divided into two steps: deforming (Fig. 5.3(b)) and welding (Fig. 5.3(c)). In Fig. 5.3(a), a surface area, $\Delta A_e{}^{(a)}$, will be embedded at time *t*. Because of the deformation from ball milling, this surface area changes to $\Delta A_e{}^{(b)}$ in Fig. 5.3(b), which is embedded during the welding process at time *t*+*Δt* (in Fig. 5.3(c)).

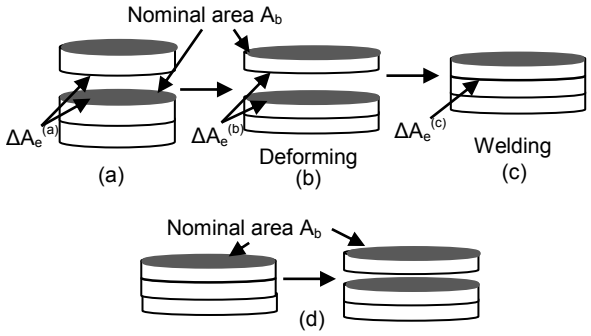

Fig. 5.3: Schematics of: (a)-(c) welding and (d) fracturing of particles; the dark area indicated the nominal area of the particles.

Comparing Fig. 5.3(b) and (c):

$$\frac{\Delta A_e{}^{(b)}}{A_e{}^{(b)} + A_s{}^{(b)}} = \frac{A_s{}^{(b)} - A_s{}^{(c)}}{A_e{}^{(c)} + A_s{}^{(c)}} \tag{5.16}$$

From Fig. 5.3(a) and (b), the following relationship can be obtained with assumption (iv):

$$\frac{A_s{}^{(a)}}{A_e{}^{(a)} + A_s{}^{(a)}} = \frac{A_s{}^{(b)}}{A_e{}^{(b)} + A_s{}^{(b)}} \tag{5.17a}$$

$$\frac{\Delta A_e{}^{(a)}}{A_e{}^{(a)} + A_s{}^{(a)}} = \frac{\Delta A_e{}^{(b)}}{A_e{}^{(b)} + A_s{}^{(b)}} \tag{5.17b}$$

Combining Eqn. (5.16) and (5.17):

$$\Delta A_e(t) = \frac{\alpha(t) - \alpha(t + \Delta t)}{\alpha(t)} A_s(t) \tag{5.18}$$

where $\alpha(t) = A_s(t)/\big(A_e(t) + A_s(t)\big)$.

5.4.4 Determination of *k*

k in Eqn. (5.12) is the ratio of the welded area and fractured area during mechanical alloying. The flow char to mathematically determine *k* was shown in Fig. 5.2. First, a rule between the welding/fracturing of particles and the change of surface area is established as shown in Eqn. (5.19). During a short time, Δt, assume n_w number of particles welded, n_f number of particles fractured, and $n_{\Delta t} = n_w + n_f$ is the total number of particles are involved in fracturing and welding. According to Assumption (v) and as indicated in Fig. 5.3, the change of embedded surface area due to welding is $\Delta A_w(t) = n_w \times A_b(t)$ (Eqn. (5.19a)), and exposed surface area due to fracturing is $\Delta A_f(t) = 2n_f \times A_b(t)$ (Eqn. (5.19b)), where $A_b(t)$ is the average nominal area of single particle.

$$\Delta A_w(t) = n_w \times A_b(t) \tag{5.19a}$$

$$\Delta A_f(t) = 2n_f \times A_b(t) \tag{5.19b}$$

The number of particles involved in fracturing and welding in a short time period Δt is calculated as shown in Eqn. (5.20). The average time interval between effective impacts involving all the particles can be defined as τ (Maurice and Courtney 1995a). Therefore, $1/\tau$ fraction of all the particles will be effectively impacted in a given unit period of time. The total number of particles involved in welding or fracturing can be obtained by Eqn. (5.20a) and τ can be determined according to (Maurice and Courtney 1995a) in Eqn. (5.20b).

$$n_{\Delta t} = \frac{\Delta t n_t}{\tau} \tag{5.20a}$$

$$\tau = \frac{1}{15\sqrt{3}\Gamma}\left(\frac{R_b \rho_b^{\frac{1}{2}} H_v^{\frac{1}{2}}}{\rho_p C R h_c v}\right) \tag{5.20b}$$

where R_b and ρ_b are the radius and density of the milling ball, respectively; ρ_p and H_v are the density and hardness of the powder, respectively; CR is the charge ratio (mass of balls/ mass of powder); h_c is the powder thickness coating the milling balls; v is the ball impacting velocity; $\Gamma = I_b l_e$ is the frequency of effective impaction that can fracture or weld the particle; I_b is the ball impact frequency for the system; and l_e is the effective impaction fraction.

Combining Eqn. (5.19) and (5.20) we have:

$$2\Delta A_w(t) + \Delta A_f(t) = 2\frac{\Delta t}{\tau}\gamma(t)A_s(t) \tag{5.21}$$

where $A_{b,t}(t) = n_t A_b$ and $\gamma(t) = A_{b,t}(t)/A_s(t)$.

Finally, the welded area and fractured area during mechanical alloying was expressed as k and can be solved by combining k can be solved from Eqns. (5.6), (5.12) (5.20) and (5.21):

$$k = \frac{\frac{\gamma}{\tau}\frac{\alpha(t)}{\frac{d\alpha(t)}{dt}} + 1}{\frac{\gamma}{\tau}\frac{\alpha(t)}{\frac{d\alpha(t)}{dt}} - \frac{1}{2}} \tag{5.22}$$

5.5 Results

The results of theoretical analysis are provided in this section. The surface CNT length, length distribution, surface area, nominal area and embedded area were examined. In addition, experimentally measured parameters are presented. CNT dispersion was analyzed through optical image analysis from the fabricated composite.

5.5.1 Surface CNT Length Distribution ($\Phi_s(l,t)$)

The CNTs collected from the particle surface at different mechanical alloying times are shown in Fig. 5.4. The measured CNT length information is summarized in Table 5.2. It was difficult to precisely measure the length of as-received CNTs due to the highly curved nature in 3D space. The measurements are accurate for CNTs mechanically alloyed for 3 minutes, 10 minutes, 30 minutes and 1 hour, since they are laid on an Al foil. The 2D images reflect the correct lengths of the CNTs. As expected, the length of CNTs on the particle surface decreased as the mechanical alloying time increased. The average CNT length decreased from the original length of 4.24 μm to 1.69 μm in the first ten minutes, and then slowly decreased to 0.85 μm after one hour. As shown in Fig. 5.5, as-received CNTs form spherical agglomerates prior to the mechanical alloying process. These CNT spherical structures were crushed into dense CNT layers in the first ten minutes of mechanical alloying, which damaged the CNTs. The sudden change of CNT length in the first 10 minutes indicated that the CNTs were severely damaged when the CNT spherical structures were crushed.

Table 5.2: Experiment results

MA time (t, min)	Number of CNTs measured	Average length (μ, μm)	CNT length variance (σ^2, μm^2)	Agglomeration area fraction (A_a)
0	45	4.24	2.21	N/A
3	62	1.97	1.25	1.625
10	53	1.69	0.91	1.58
20	41	1.36	0.61	1.23
30	49	1.28	0.58	0.55
40	48	1.02	0.66	0.055
60	43	0.85	0.64	0.017

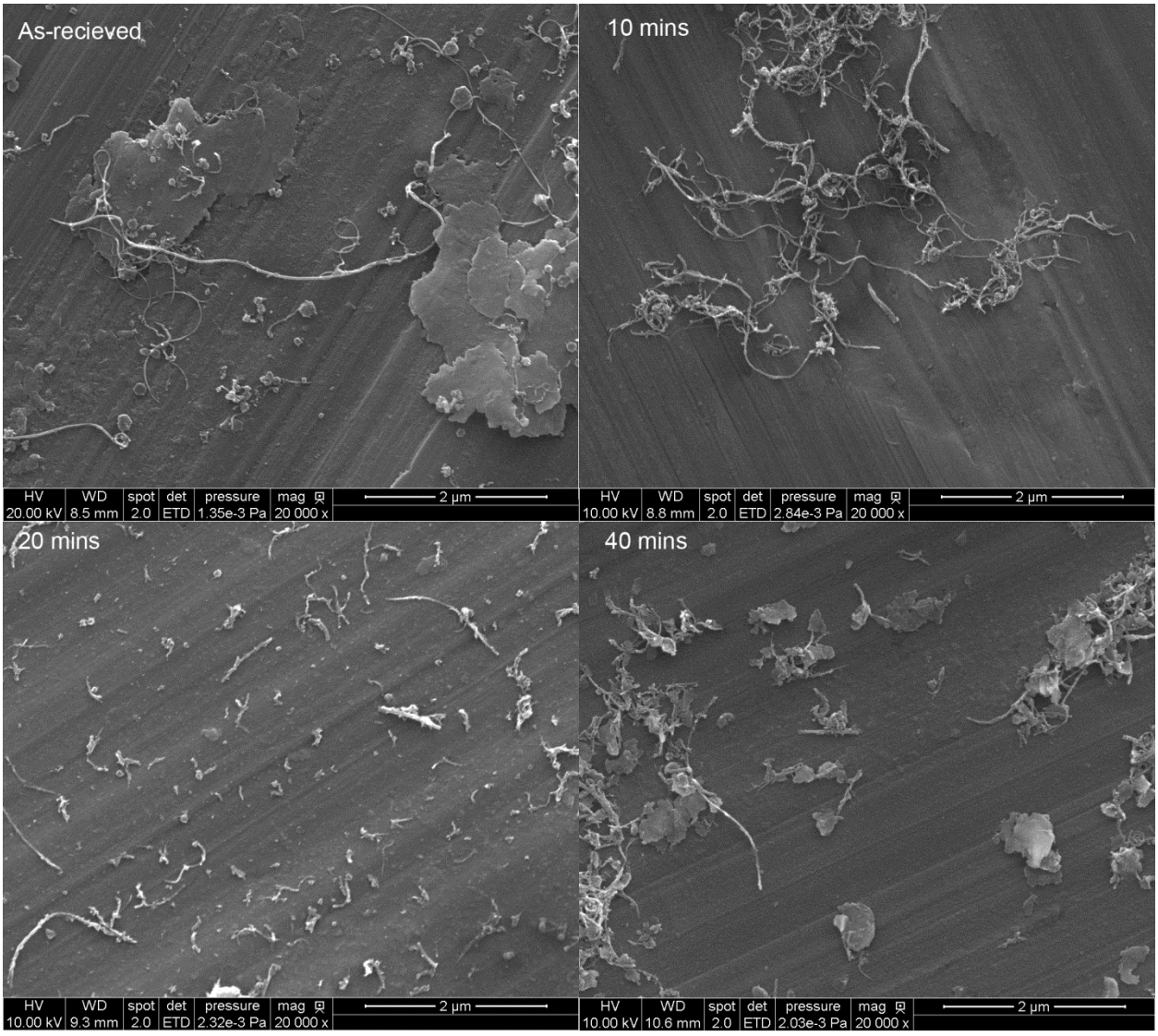

Fig. 5.4: CNT morphology with different mechanical alloying time

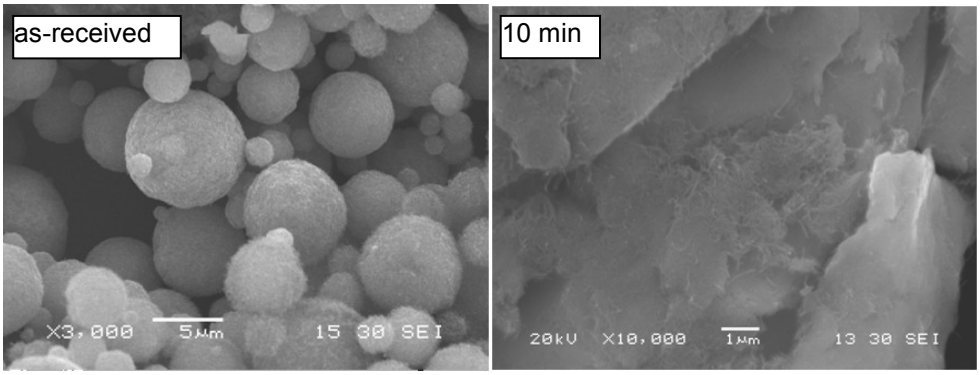

Fig. 5.5: As received CNT and Al6061-CNT powders mechanically alloyed for 10 mins.

As shown in Fig. 5.6(a), a normal distribution was utilized to fit the histogram of the measured CNT lengths. The fitted mean (μ) and variance (σ^2) at different mechanical alloying times are listed in Table 5.2. The surface CNT length distribution, $\phi_s(l)$, may be obtained as:

$$\phi_s(l) = \frac{1}{1 - G(0; \mu, \sigma^2)} g(l; \mu, \sigma^2), l > 0 \tag{5.23}$$

where l is the length of a single CNT, $g(l; \mu, \sigma^2)$ is the fitted normal distribution with mean of μ and variance of σ^2; $G(0; \mu, \sigma^2)$ is the value of cumulative distribution function of normal distribution $g(l; \mu, \sigma^2)$ at $l = 0$. The fitted surface CNT length distributions at different mechanical alloying times are shown in Fig. 5.6(b). As the average length of the CNT length decreased, the CNT length variance also decreased during mechanical alloying.

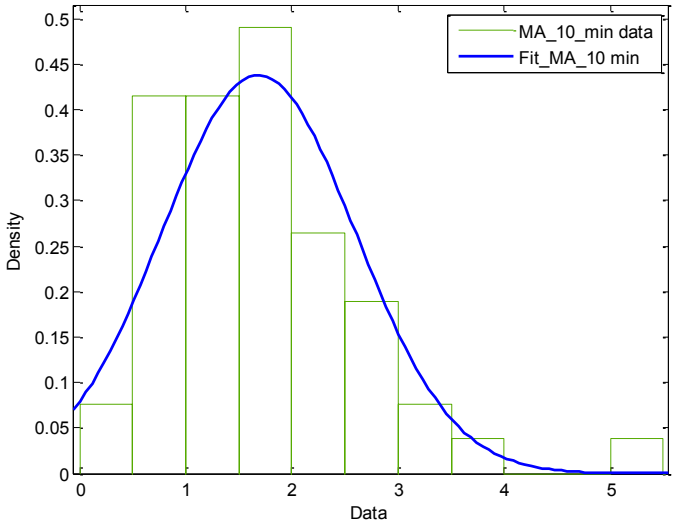

(a)

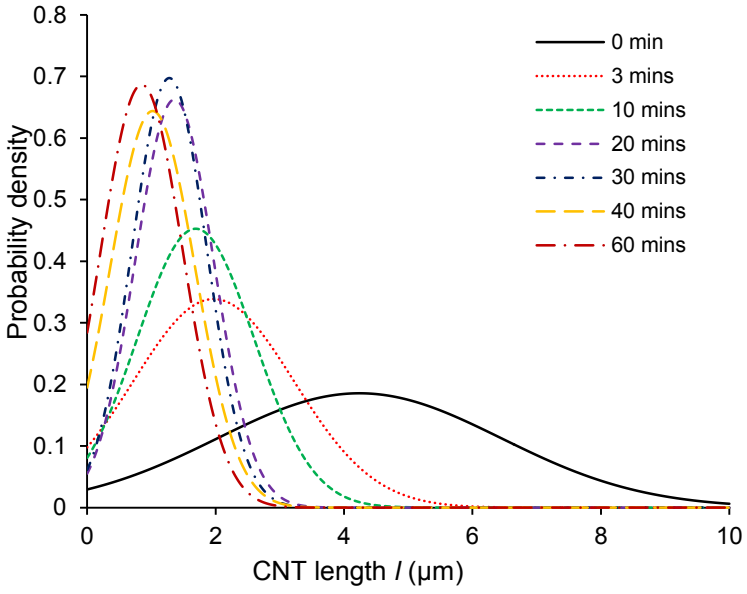

(b)

Fig. 5.6: (a) CNT length distribution at mechanical alloying time 10 mins and (b) the surface CNT length distribution at different mechanical alloying times

5.5.2 CNT Dispersion (*d*)

The SEM images of the fabricated Al6061-CNT samples are shown in Fig. 5.7. The CNT agglomerations were shown as black areas in the SEM. The fraction of CNT agglomeration area over the total image area was measured by software ImageJ and is listed in Table 5.2 as A_a. In the first 10 minutes, the CNT de-clustering was very slow due to rupturing of CNT spherical structure. After the CNT-metal powder was mechanically alloyed for 40 minutes, CNT agglomerated area was rarely observed. Since the agglomerated CNT weight fraction can be obtained from the images ($W_a/W_t = A_a/A_{a,0}$), the dispersion can be written as $d = 1 - A_a/A_{a,0}$, where $A_{a,0}$ is the CNT agglomeration area when no CNT is dispersed. The dispersion, d, can be fitted with the equation shown in Table 5.3, and the result is shown in Fig. 5.8.

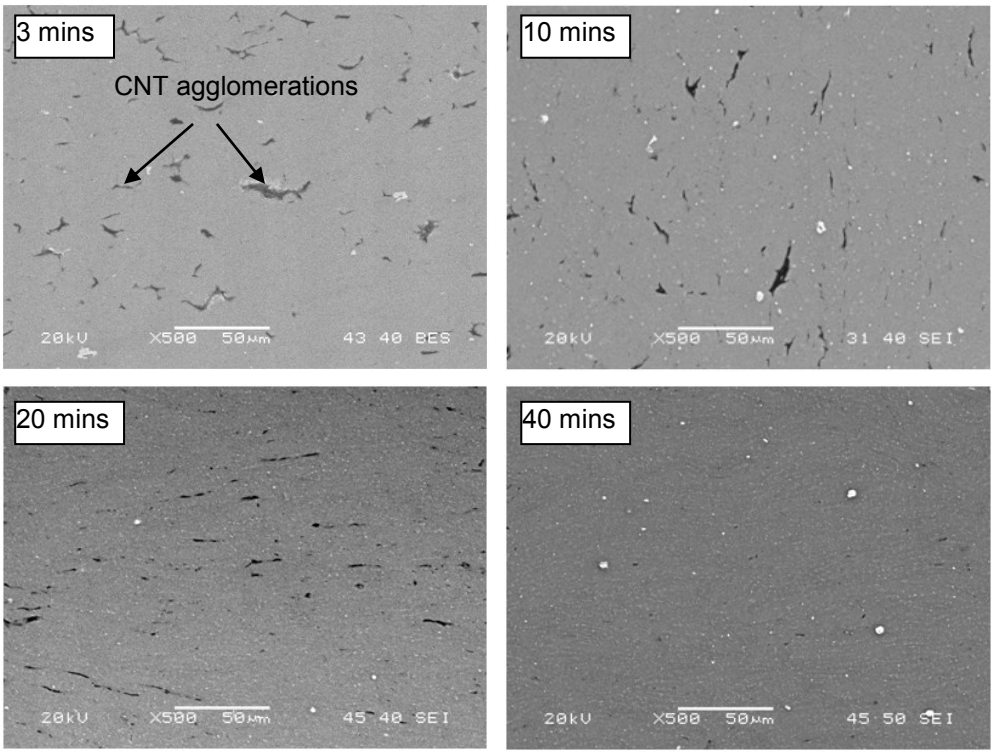

Fig. 5.7: SEM images of the polished surface of the Al6061-CNT samples

Table 5.3: Fitting equations and fitted constant

Parameter	Equation format	Constant value				R^2
		C_1	C_2	C_3	C_4	
d	$d = \frac{1}{C_1 e^{C_2 t} + 1}$	148.6	-0.192			0.9982
α	$\alpha = C_1 e^{C_2 t}$	1.038	-0.059			0.9642
μ	$\mu = C_1 e^{C_2 t} + C_3 e^{C_4 t}$	2.341	-0.914	1.899	-0.014	0.9984
σ	$\sigma = C_1 e^{C_2 t} + C_3 e^{C_4 t}$	1.417	-0.309	0.725	-0.003	0.9828

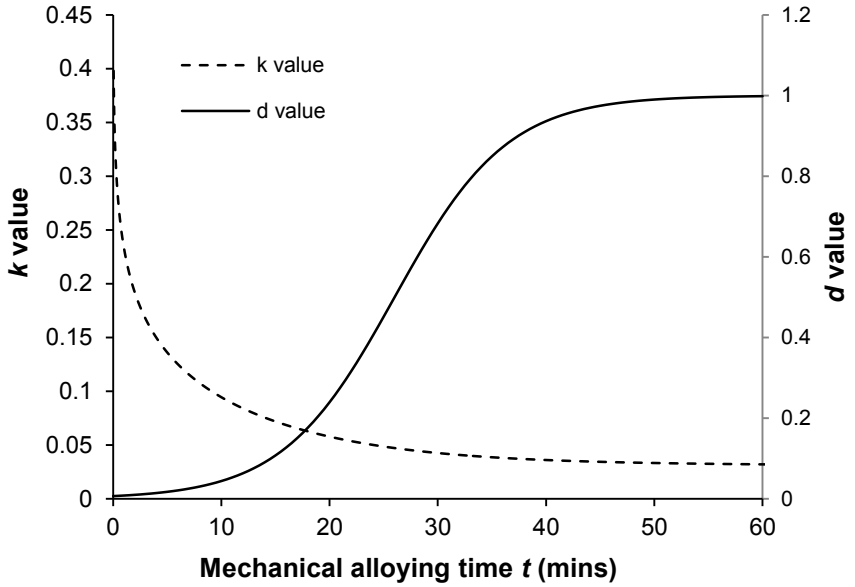

Fig. 5.8: The dispersion *d* and computed *k* value during mechanical alloying

5.5.3 Nominal Area (A_b), Surface Area (A_s) and Embedded Area (A_e)

The SEM images of the particles mechanically alloyed for 30 mins are shown in Fig. 5.9(a). Due to the complexity of the particle shapes, three simplified geometries as shown in Fig. 5.9(b)-(d) were used to approximate the particle shape for the analysis. Only a small amount of spherical particles (Fig. 5.9(d)) were found, and they were as-received particles without any deformation (or with slight deformation). The dimensions, D, H, L and W, can be directly measured from the SEM images. The particle layer thickness, h, was estimated from the optical images of the etched samples, which clearly showed the thickness of the merged layers within each particle (see Fig. 5.9(e)). Therefore, the surface area (A_s) and embedded area (A_e) can be quantified. During mechanical alloying, the deformed particles stack in layers. As shown in Fig. 5.9(a) and (e), the surface area will be exposed or welded in the layers. Therefore, the nominal area

was measured as the surface area of the layers, indicated in Fig. 5.9(a). The α and γ based on the measured data are listed in Table 5.4. In addition, the volume of each particle was estimated, and an equivalent particle diameter was calculated. The overall particle thickness was also measured and the volume average strain of the particles was calculated by Eqn. (5.24) (Wu and Kim 2011a). Both the equivalent particle diameter and strain are listed in Table 5.4.

$$\varepsilon = \frac{-6}{\pi D^3} \int_0^{\sqrt{\frac{D^2-h^2}{4}}} \left[2\pi r \sqrt{D^2 - 4r^2} \ln\left(\frac{h}{\sqrt{D^2 - 4r^2}} \right) \right] dr \tag{5.24}$$

where D is the initial particle diameter; r is integrating parameter.

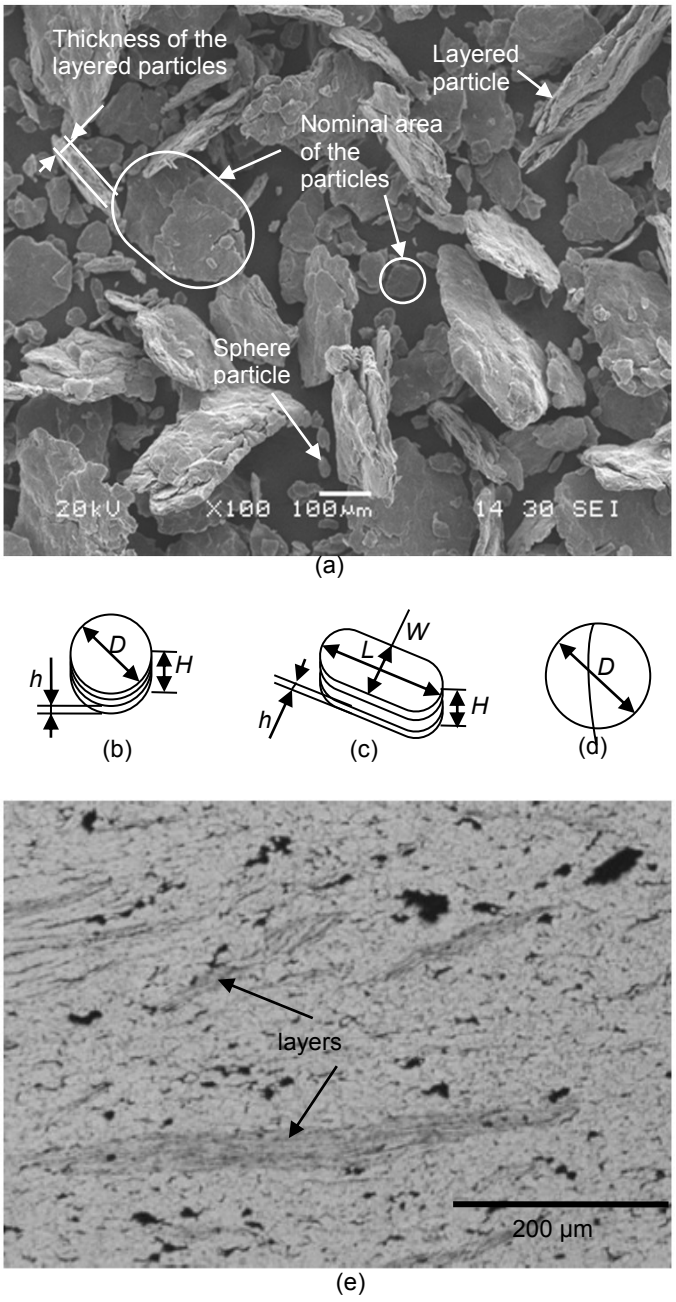

Fig. 5.9: (a) Al6061-CNT powders mechanically alloyed for 30 mins, (b)-(d) three types of the approximation geometries and (e) optical image of Al6061-CNT composite with powders mechanically alloyed for 3 mins

Table 5.4: Experiment results for the particles

MA time (t, min)	Surface area/total area (α)	Nominal area/surface area (γ)	Thickness of layered particles (h, μm)	Thickness of all the particles (μm)	Strain of all the particles	Equivalent particle diameter (μm)
0	1	N/A	N/A	9.38	N/A	13.8
3	N/A	N/A	2.12	8.35	0.02	N/A
10	0.70	0.31	2.93	4.01	0.54	11.0
20	0.23	0.35	1.83	2.94	0.84	27.3
30	0.16	0.38	1.62	1.92	1.25	29.1
40	0.085	0.32	1.85	1.85	1.29	60.9
60	0.028	0.31	1.39	1.39	1.57	130.8

5.5.4 Overall CNT Length Distribution ($\Phi(l,t)$)

Finally, the overall CNT length distribution can be predicted from Eqn. (5.15). k and τ can be calculated from Eqn. (5.22) and (5.20b). The parameters used to calculate τ are listed in Table 5.5. $\phi_s(l,t)$, $\alpha(t)$ and d can be obtained with experimentally measured data. Since γ did not fluctuate much, a mean value of 0.334 was used. The curve-fitting equations and parameter values are listed in Table 5.3. The final results were computed by Matlab with an Euler explicit computational scheme. The flow chart is shown in Fig. 5.10.

Table 5.5: The data used in the calculation of impact frequency

Parameter	Material	Value
R_b	Zirconia	6.35 mm
ρ_b	Zirconia	5680 kg/m^3
ρ_p	Al6061 (T-O)	2700 kg/ m^3
H_{v0}	Al6061 (T-O)	165 MPa
CR		4.06
h_c		120 μm (Maurice and Courtney 1995b)
v	Zirconia	18.7 m/s (Davis, Mcdermott et al. 1988)
I_b		320 (Davis, Mcdermott et al. 1988)
l_e		1.1% (Davis, Mcdermott et al. 1988)

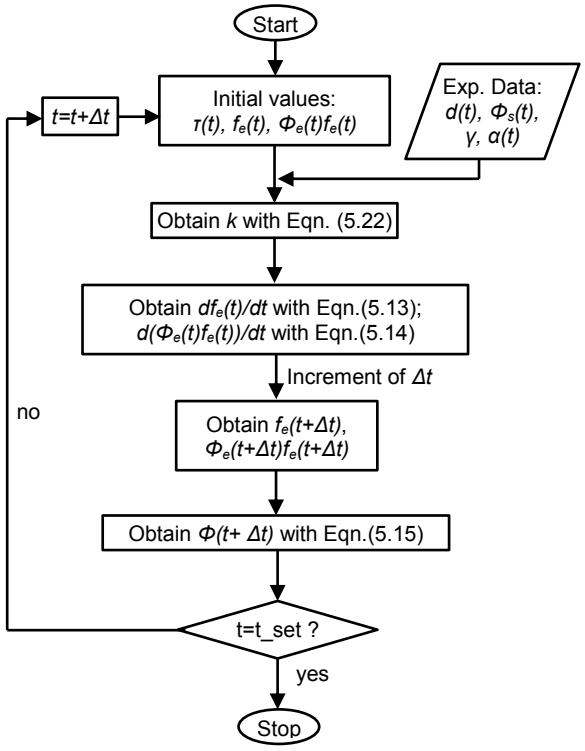

Fig. 5.10: Flow chart of the computing code

The computed *k* value is shown in Fig. 5.8. The *k* value decreased immediately as the mechanical alloying time passed. Initially, the agglomerated CNTs prohibited the welding of particles. The welding mechanism seemed to dominate once the dispersion of CNTs occurred.

The average surface CNT length (μ), average overall CNT length (l_{all}), overall CNT length distribution $\Phi(l,t)$, and weight fraction of the embedded CNTs ($f_e(t)$) are shown in Fig. 5.11. As shown in Fig. 5.11(a), the overall CNT length decreased significantly in the first ten minutes, which was attributed to the crushing of the spherical CNT agglomerates. In Fig. 5.11(b), the average surface CNT length (μ) and overall CNT length (l_{all}) coincided during the first 20 minutes of mechanical alloying. A smaller *k*

value indicates a higher welding rate, providing protection for CNTs from further damage. Initially, the high agglomeration of surface CNTs prevented the embedding of CNTs inside the particles, since the welding rate was not much higher than the fracturing rate indicated by the larger k value shown in Fig. 5.8. Consequently, less than 10% of the CNTs were embedded, and therefore, the surface and overall CNT length were similar. As the mechanical alloying time increased, more CNTs were dispersed and a low k value was obtained, enhancing the welding process. Therefore, the surface CNT length became shorter than the overall CNT length. The overall CNT length distribution and average CNT length does not change after 60 minutes of mechanical alloying because over 85% of the CNTs were embedded inside the particles protecting the CNTs from further damage. Although welding of the particles is regarded as a negative factor for the subsequent sintering process, it can provide protection of CNTs from further damage, especially when long mechanical alloying time is applied.

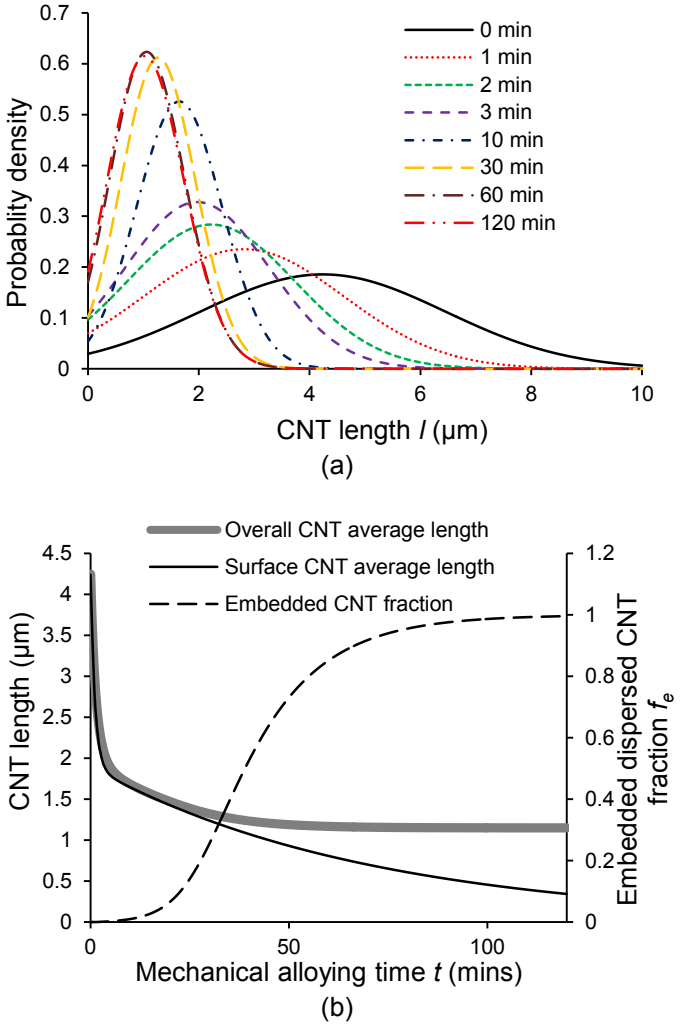

Fig. 5.11: (a) Probability function for overall CNT length distribution at different mechanical alloying time, (b) average overall CNT length, average surface CNT length and embedded CNT fraction

5.6 Conclusion

The overall CNT length and length distribution during mechanical alloying were predicted for the first time, and the effects of welding and fracturing of the CNTs and aluminum particles were better understood. Experiments were conducted to assist the

prediction of overall CNT length. The surface CNTs were successfully collected and analyzed, and the dispersion of CNTs was studied. The CNT length decreased significantly during mechanical alloying. Severe CNT length reduction occurred (from 4.24 μm to 1.69 μm) in the first several minutes due to the crushing of CNT agglomeration balls. After that, the length of CNTs decreased slowly to 1.16 μm, and the CNTs were dispersed in the following one hour. In addition, the welding/fracturing of Al6061 particles and the dispersion of CNTs affected the overall CNT length. The welding of metal particles surrounded the CNT with metal layer and protected CNTs from further contact with the milling media. Therefore, limited CNT length reduction occurred after one hour of mechanical alloying. Once the CNT dispersion took place, the welding mechanism dominated the CNT+Al6061 mechanical alloying process due to the ductile nature of Al6061. The model provided an insight into the breakage of CNTs during the harsh ball milling operation, which has been a challenge for experimental measurement. The work can provide useful information when evaluating the effects of CNTs on mechanical, thermal and electrical properties.

CHAPTER 6 CARBON NANOTUBE REINFORCED ALUMINUM COMPOSITE FABRICATED BY SEMI-SOLID POWDER PROCESSING

6.1 Introduction

Incorporation of CNTs in polymer composites has been widely investigated since the discovery of CNTs by Iijima in 1991 (Iijima 1991). High strength and high thermal and electronic conductivities make CNTs an ideal reinforcing material for composites. In metal composites, however, the progress has been rather slow primarily due to challenges associated with CNT dispersion and high temperature processing used in the synthesis of metal composites. Various fabrication methods, including sintering (Deng, Wang et al. 2007), hot extrusion (Xu, Wei et al. 1999), spark plasma sintering (Kwon, Estili et al. 2009), spark plasma extrusion (Morsi, Esawi et al. 2010), casting (Zhou, Zhang et al. 2007), equal channel angular pressing (Quang, Jeong et al. 2007) and friction stir processing (Lim, Shibayanagi et al. 2009), have been investigated to incorporate CNTs into the Al matrix. Each manufacturing method has its unique characteristics while also having weaknesses.

One of the main challenges in the fabrication of metal-CNT composites is to uniformly disperse the CNTs in the metal matrix (Noguchi, Magario et al. 2004; He, Zhao et al. 2007). For powder-based manufacturing approaches, mechanical alloying has

been widely applied to break down the CNT clusters and homogeneously disperse them in the metal matrix (Liao, Tan et al. ; Esawi and Morsi 2007; Li, Misra et al. 2009; Poirier, Gauvin et al. 2009). Recently, Morsi et al. (Morsi and Esawi 2007) and Wang et al. (Wang, Choi et al. 2009) investigated the effects of mechanical alloying time on the evolution of blended aluminum-CNT composite powder. The size of particles increased, and the dispersion of CNTs was achieved by the mechanical alloying process (Morsi and Esawi 2007). However, no study was found that reported the effects of mechanical alloying time on the microstructure and mechanical properties of the fabricated composites.

In this study, SPP combined with mechanical alloying procedure was employed to fabricate the CNT reinforced Al6061 composites. As shown in Fig. 6.1, SPP expands the traditional semi-solid forming by replacing the bulk materials with powders (Wu, Kim et al. 2010b). The semi-solid bulk forming requires break-down of the dendritic microstructure in the feedstock alloy materials (Steinhoff, Weidig et al. 2004). SPP combines the advantages of powder metallurgy and semi-solid forming. It exploits unique material behavior of solid-liquid slurry, which helps the formation of intricate shapes (Kumar, Martin et al. 1993). It also enables mixing of various particle or fiber elements for improved composite properties and eliminates post-processing steps required in powder metallurgy routes (Wu, Kim et al. 2010a). According to the SPP experiments carried out by Chen and Yang et al. (2005b), four basic steps are generally involved in SPP: powder preparation, powder pre-compaction, heating and semi-solid forming. Previous studies have demonstrated the potential of SPP in fabricating various

metal composites, including Al-SiC (Guo and Tsao 2000), Al-Ti (Yasue 2000) and Al-Mg (Young and Clyne 1986a), and in tailoring the composition of composite materials effectively (Wu, Kim et al. 2010b).

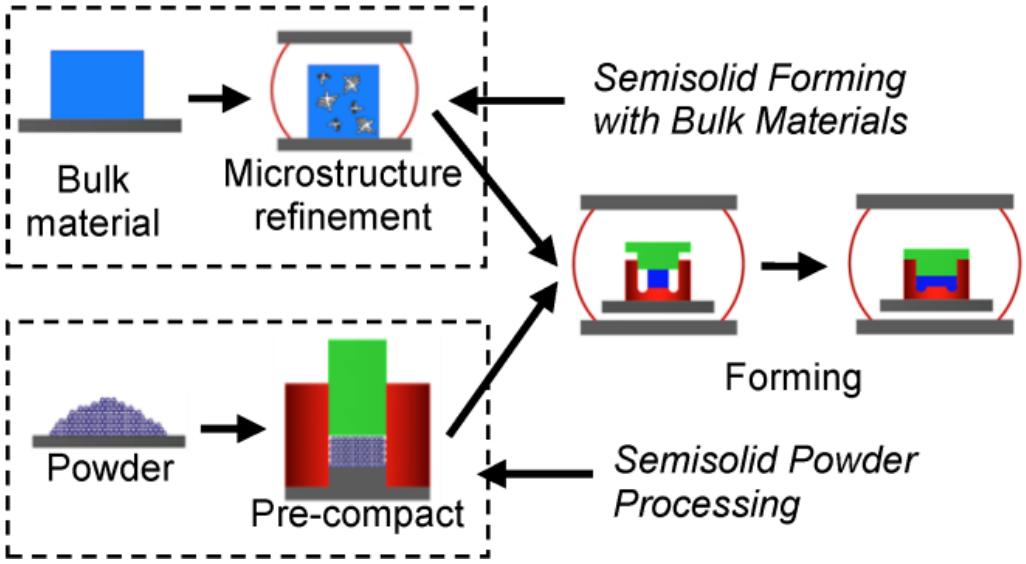

Fig. 6.1: Comparison of conventional semi-solid forming and semi-solid powder processing

This study presents an original work on the synthesis of CNT reinforced metal composite by mechanical alloying followed by SPP. Al6061-CNT composites fabricated using mechanical alloying times and processing temperature were studied. The compaction behavior, microstructure, hardness, fracture surface, and composition of the composites were examined and analyzed.

6.2 Experimental Procedure

Al6061 particles (Valimet Inc.) and multi-walled carbon nanotubes (MWCNTs) (NanoLab Inc.) were used to make Al6061-1.0 wt.% CNT composite samples. The Al6061 particles had mean particle size of 13.8 μm, and MWCNTs were 20–50 nm in diameter and 5–20 μm in length. The chemical composition of Al6061 powders is shown in Table 6.1. Esawi and Morsi (2007) mechanical alloyed the Al powder and CNT mixture and demonstrated its effectiveness in dispersing the CNTs into the metal particles.

Table 6.1: Chemical composition of Al6061 (Valimet, Inc.)

Element	Al	Mg	Si	Cu	Fe	Cr	Zn	Mn	Ti
Amount (%)	Bal.	1.03	0.52	0.28	0.27	0.09	0.06	0.03	0.01

The experimental setup is shown in Fig. 6.2. The die was fabricated from H13 tool steel and was heat treated to Rockwell hardness of HRC 50. The high temperature boron nitride spray (Momentive Performance Materials-Quartz, Inc.) was used to coat and lubricate the die wall to prevent the possible reaction between the Al and die material at elevated temperatures. The powder mixture was pre-compacted under 100 MPa of pressure, which was then heated in a furnace (Applied Test System Inc.). A 50 MPa of pressure was applied near 580°C at which temperature the Al6061 started to melt. The pressure was held constant for 30 minutes while the material was heating up to the control temperature settings. For SPP, the liquid content, which is largely determined by the processing temperature, is one of the most important factors that influence the

composite manufacturability and property. Three temperature settings (600°C, 620°C and 640°C) were used in this study. The compression and heating profiles for the three processing temperatures are shown in Fig. 6.3. The differential scanning calorimetry analysis from Kim and Kang et al. (2007) showed that the liquid fractions of Al6061 at 600°C, 620°C and 640°C were about 7.5%, 12.5% and 30.0%, respectively. Four Al6061-1.0 wt.% CNT powder batches were prepared with mechanical alloying times of 0.5, 1, 2, and 3 hours. The reference samples for each alloying time were prepared under the same conditions using only the Al6061 powder without any CNT. The experimental settings are summarized in Table 6.2. The temperature was fixed at 640°C when studying the effects of mechanical alloying time on the composite, while mechanical alloying time was fixed at 3 hour when temperature was varied. The experiments were carried out under air atmosphere. The surface oxide layers are effectively broken down because of the relative sliding and deformation of the particles by the externally applied pressure during SPP (Xie, Hailat et al. 2007). The presence of liquid-phase helps to fill in pores enabling high density structure. Relatively short exposure time with the assistance of pressure and enclosed-die setup also helps to prevent excessive oxide formation. It has also been reported that the Mg alloy element in Al6061 can eliminate the surface oxides (Fuentes, Rodriguez et al. 2003) and improve the interfacial bonding between Al particles by disrupting the oxide layer (Lumley, Sercombe et al. 1999). Fogagnolo and Robert et al. (2006) and Xie and Hailat et al. (2007) reported that ceramic reinforced Al6061 fabricated with pressure assisted sintering of Al6061 at atmospheric environment obtained strong interfacial bonding between the Al6061 particles and reinforcement phase.

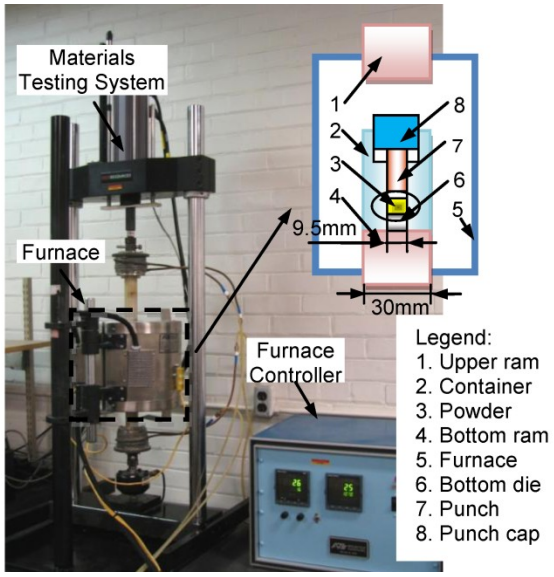

Fig. 6.2: Experiment setup for semi-solid powder processing

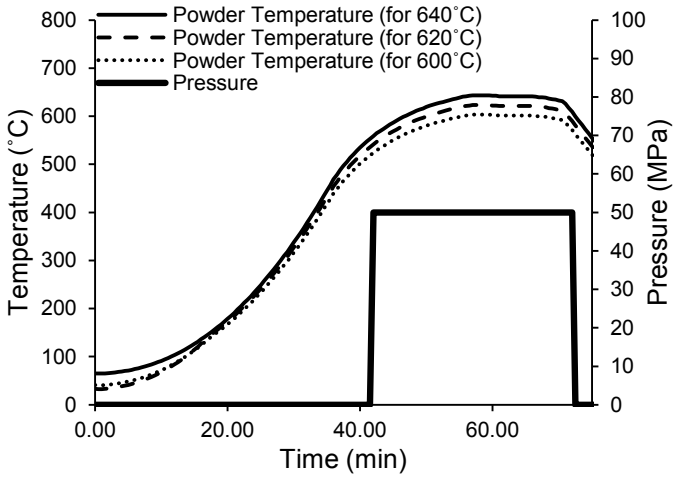

Fig. 6.3: Heating and compression profiles used in the experiment

Table 6.2: Parameter settings for the experiment

Parameter	Settings
Forming Pressure (MPa)	50
Pressure Holding Time (min)	30
CNT Loading (wt.%)	1
Punch Velocity (mm/s)	0.065
Powder Mechanical Alloying Time (h)	0.5, 1, 2, 3
Operating Temperature (°C)	600, 620, 640
Liquid Fraction of Al6061	0.075, 0.125, 0.300

The microstructures of the polished and etched samples were observed with an optical microscope (Zeiss, Axiovert 200M) and scanning electron microscope (JEOL JSM-606LV). Commercial software, ImageJ, was used to determine the relative density of the composite by measuring the black area fraction in the optical image took from the samples. Five images took from different locations were measured to obtain an average relative density for the samples. The hardness of samples was measured by LECO LM247AT Micro Hardness Tester after appropriate polishing procedure. A Siemens D-500 X-ray diffraction system was used to obtain the X-ray diffraction (XRD) pattern of the powder and composite samples. Bend test samples were polished to the dimension of 0.9 mm in thickness and 1.2 mm in width for the Al6061 and Al6061-CNT samples made from different mechanical alloying times. The fracture surfaces were examined by scanning electron microscope.

6.3 Results and Discussion

First, mechanically alloyed Al6061 particles and CNTs were examined. Then compression behaviors of the Al6061-CNT particles during pre-compaction and consolidation stages were analyzed. The microstructure, hardness, fracture surface and the composition analysis were performed to understand the effects of liquid fraction on the composite. Last, the material strength was predicted with a modified shear lag model.

6.3.1 Mechanically Alloyed Powders

SEM images of as-received CNTs and Al6061-CNT powders that were mechanically alloyed for different times are shown in Fig. 6.4. As-received CNTs were strongly entangled in roughly spherical agglomerates with diameters of 1–7 μm (Fig. 6.4(a) and (b)). After 10 minutes of mechanical alloying, the CNT bundles were crushed and attached to the Al6061 particle surface (Fig. 6.4(c)). The original spherical CNT agglomerates was nearly absent in the powder. The dispersion of CNTs improved with increasing mechanical alloying time (Fig. 6.4(d) and (e)), while the visible CNTs on the Al6061 particle surfaces gradually decreased (Fig. 6.4(f)). After three hours of mechanical alloying, CNTs could be rarely found on the surface (Fig. 6.4(g)). The lengths of the CNTs on the surface of Al6061 particles decreased as the mechanical alloying time increased. After one hour of mechanical alloying, the length of the CNTs on the particle surfaces decreased to about 1.2 μm from the original length of over 5 μm. It further decreased to less than 1 μm after three hours of mechanical alloying. This observation was quite different from the work performed by Esawi et al. (Esawi and Morsi 2007), which indicated that there was limited CNT breakage during mechanical

alloying. In their work, initial CNT structure may have been different from the spherical agglomerates seen in this study, so the harsh initial crushing may have been avoided. It was speculated that the severe CNT breakage observed in this study was due to the high-energy mechanical alloying equipment used in this experiment and the initial crushing of the spherical CNT agglomerates.

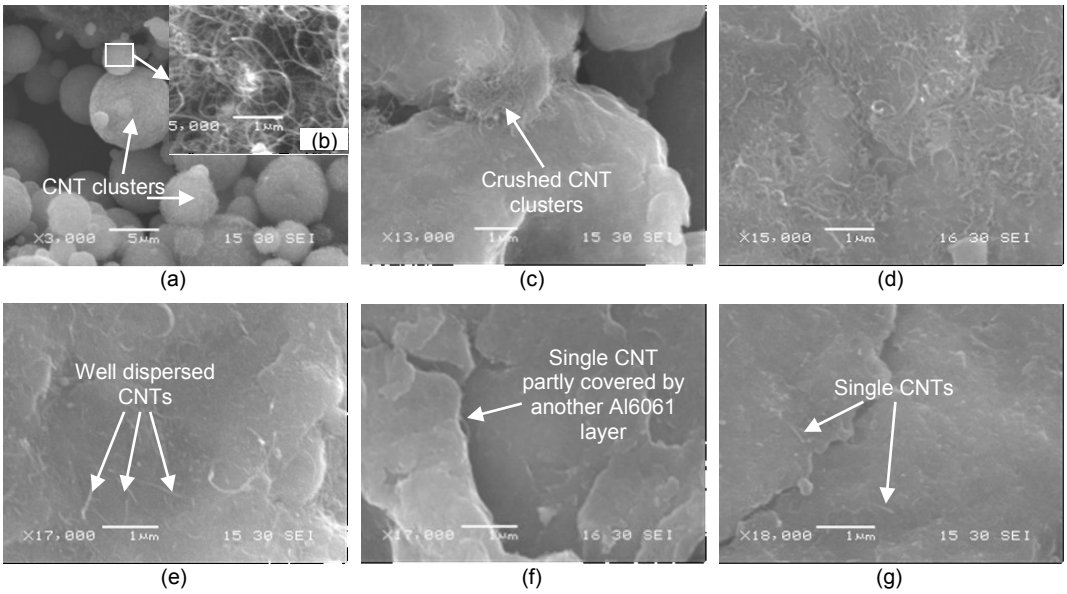

Fig. 6.4: CNTs and mechanically alloyed Al6061 powder and CNTs: (a) and (b) are images of as-received CNTs; (c)−(g) are Al6061 powder and CNTs mechanically alloyed for (c) 10 minutes, (d) 0.5 hr, (e) 1 hr, (f) 2 hrs and (g) 3 hrs, respectively.

From these observations, the mechanical dispersion of CNTs occurred in two stages. First, the spherical agglomerates of as-received CNTs were crushed by colliding with the milling balls. For the condition used in this study, this occurred in the first 30 minutes. Second, the crushed CNT clusters were dispersed into individual CNTs by the shearing action of the Al6061 particles and the milling balls. The CNTs were well dispersed after two hours of mechanical alloying. No agglomeration of CNTs was found

on the surface of Al6061 particles (Fig. 6.4(f)). The clustered CNTs were typically exposed on the surface of particles and prevented the metal particles from bonding to each other. Thus, the CNT dispersion condition on the surface of Al6061 particles reflected the overall dispersion status.

The change of particle size during mechanical alloying of the Al6061 and Al6061+CNT powders was measured. The measurement results are summarized in Table 6.3. It was observed that the size of Al6061 particles increased from 13.8 μm to 620.1 μm during the first hour and then slightly decreased in the following two hours. In mechanical alloying, cold-welding and fracturing are the two competing mechanisms that govern the particle size (Morsi and Esawi 2007). In the beginning of mechanical alloying, cold-welding dominated the process, and the ductile Al6061 particles agglomerated to form larger particles (Fig. 6.5(a)). Similar observation was also reported in (Benjamin 1992). As the mechanical alloying process continued, the Al6061 particles hardened and started to fracture (Benjamin and Volin 1974), which resulted in the decrease of particle size. With further comminution, the surface temperature of the Al6061 particles increased (Koch 1989), and the particle surfaces started to bond, forming a densified structure (Fig. 6.5 (b)).

Table 6.3: Powder particle sizes, grain sizes, and average hardnesses of the composites

Mechanical alloying time (hr)	Average powder size (μm)		Grain size of the Al6061-CNT composites				Average hardness of the composites (HV)		
	Al6061 +CNT	Al6061	W (μm)	L (μm)	L/W	Area (μm^2)	Al6061	Al6061 -CNT	Hardness net percent gain (%)
0.5	8.6	29.1	7.0	10.8	1.6	68.2	48.2	49.3	2.3
1	10.5	620.1	5.2	12.5	2.6	58.6	53.2	60.4	13.5
2	15.9	446.1	4.2	14.2	3.8	62.2	55.5	71.1	28.1
3	44.6	212.8	3.1	18.4	7.4	52.4	61.5	76.5	24.4

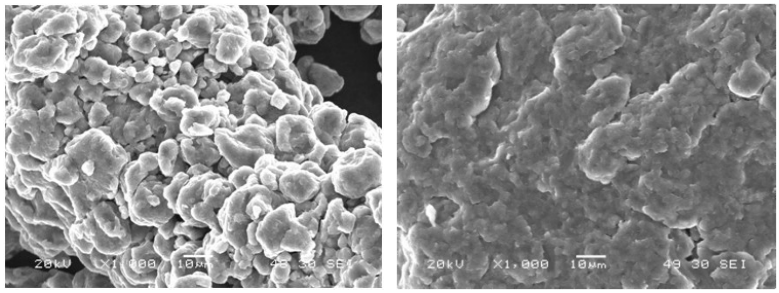

(a) (b)

Fig. 6.5: Al6061 powder mechanical alloyed for: (a) 0.5 hr and (b) 3 hrs.

In contrast to the behavior of the reference Al6061-only powder, the size of Al6061-CNT particles increased continuously as the mechanical alloying time increased (see Table 6.3), which indicated that cold-welding dominated the mechanical alloying of Al6061-CNT powders. It was also noted that the size of the Al6061-CNT particles was much smaller than that of the Al6061-only powder under the same condition. It appears that the CNTs acted as a grinding aid and inhibited the growth of particle size during mechanical alloying (Wang, Choi et al. 2009).

6.3.2 Compression Behavior of Al6061-CNT Powder

Fig. 6.6 shows the pre-compaction curve and the subsequent compression behavior at elevated temperature for Al6061-CNT composite synthesized at 640°C with powder mechanically alloyed for 3 hrs. The relative density of the compact was estimated from the punch displacement and total powder loaded, and is labeled in the figure. During the pre-compaction at room temperature, the Al6061-CNT powder achieved a relative density of 49.9%. The yield strength of the annealed Al6061 is about 55 MPa (Hatch 1984). However, the cold working during mechanical alloying strengthens the material by continuously deforming the particles. The yield strength of the mechanically alloyed particles can be estimated by Eqn. (6.1) (Maurice and Courtney 1994). The schematics of a particle before and after deformation are shown in Fig. 6.7. The minimum volume-averaged plastic strain can be estimated by Eqn. (6.2).

$$\sigma_y = K\varepsilon^n \tag{6.1}$$

$$\varepsilon = \frac{-6}{\pi D^3}\int_0^{\sqrt{\frac{D^2-h^2}{4}}}\left[2\pi r\sqrt{D^2-4r^2}\ln\left(\frac{h}{\sqrt{D^2-4r^2}}\right)\right]dr \tag{6.2}$$

K and n are strength coefficient and strain hardening exponent, respectively; D is the initial particle diameter; and h is the particle thickness after deformation; r is integrating parameter. The values of K and n were 224 MPa and 0.209 for annealed Al6061 (Hatch 1984). The particle diameter at the initial state was 9.4 μm. After three hours of mechanical alloying, the particles were flattened and had an average thickness of 3.1 μm, resulting in particle yield strength of 213 MPa. Therefore, the densification behavior of

mechanically alloyed Al6061-CNT powder during pre-compaction was mostly caused by particle rearrangement than plastic deformation.

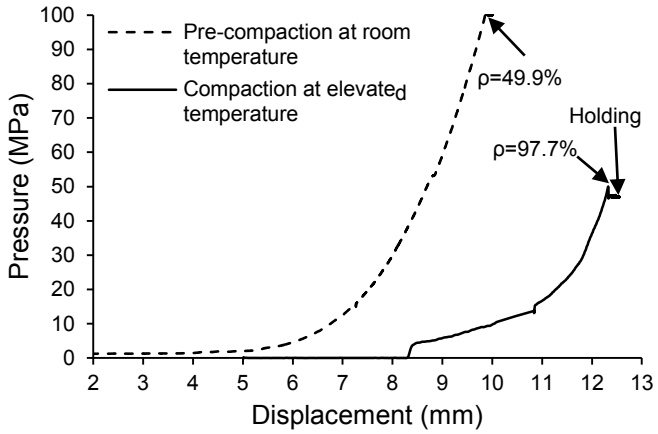

Fig. 6.6: Densification of Al6061-CNT powder during pre-compaction and consolidation at 640°C

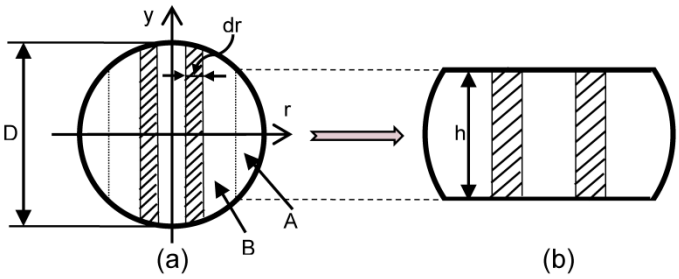

Fig. 6.7: Cross sectional view of (a) the original spherical particle and (b) flattened particle after deformation

As the compact was brought to the processing temperature, thermal expansion of the system occurred and resulted in raising the punch. The punch displacement at the end of the pre-compaction was 9.08 mm, while the initial contact at the elevated temperature occurred at 8.07 mm. The Al6061-CNT powder achieved a relative density of 97.7% at 580°C with 50 MPa of pressure due to the significant softening of the material. While

maintaining the pressure at 50 MPa, more liquid-phase formed as the temperature reached 640°C. This resulted in full densification of the composite with relative density above 99%.

6.3.3 Microstructure

The SEM images of polished and etched microstructures of the Al6061-CNT samples with powders mechanically alloyed for different mechanical alloying time are shown in Fig. 6.8. CNTs that had not been fully dispersed were observed in the Al6061-CNT sample that had been mechanically alloyed for 0.5 hour (Fig. 6.8(a) and (b)). The crushed CNT layers as observed in Fig. 6.8(c) resulted in CNT clustered areas. For the Al6061-CNT composites that had been mechanically alloyed for two and three hours, no obvious CNT agglomerations were observed, as shown in Fig. 6.8(c) and (d). The CNT dispersion condition was also confirmed by the SEM images shown in Fig. 6.9(a)−(d). It clearly showed that CNT clustering decreased with increasing mechanical alloying time. No CNT cluster was observed in the samples that were mechanically alloyed for two and three hours (Fig. 6.9(c)−(d)). In lower magnification SEM images, the CNT agglomerated area and pores both showed up as dark spots. It was difficult to discern whether a given dark spot was a pore or a CNT cluster without examining the higher magnification image. The measured fractions of dark area for both Al6061-CNT and Al6061-only samples are shown in Fig. 6.10. As mechanical alloying time increased to two hours, the dark area of Al6061-CNT composite quickly approached that of the Al6061-only composite. Therefore, the difference between the two curves indicates the change of CNT clustered area fraction. As shown in the figure, the CNT clustered area

decreased significantly in the first two hours to a very low level. After two hours, the agglomeration seemed to be minimal.

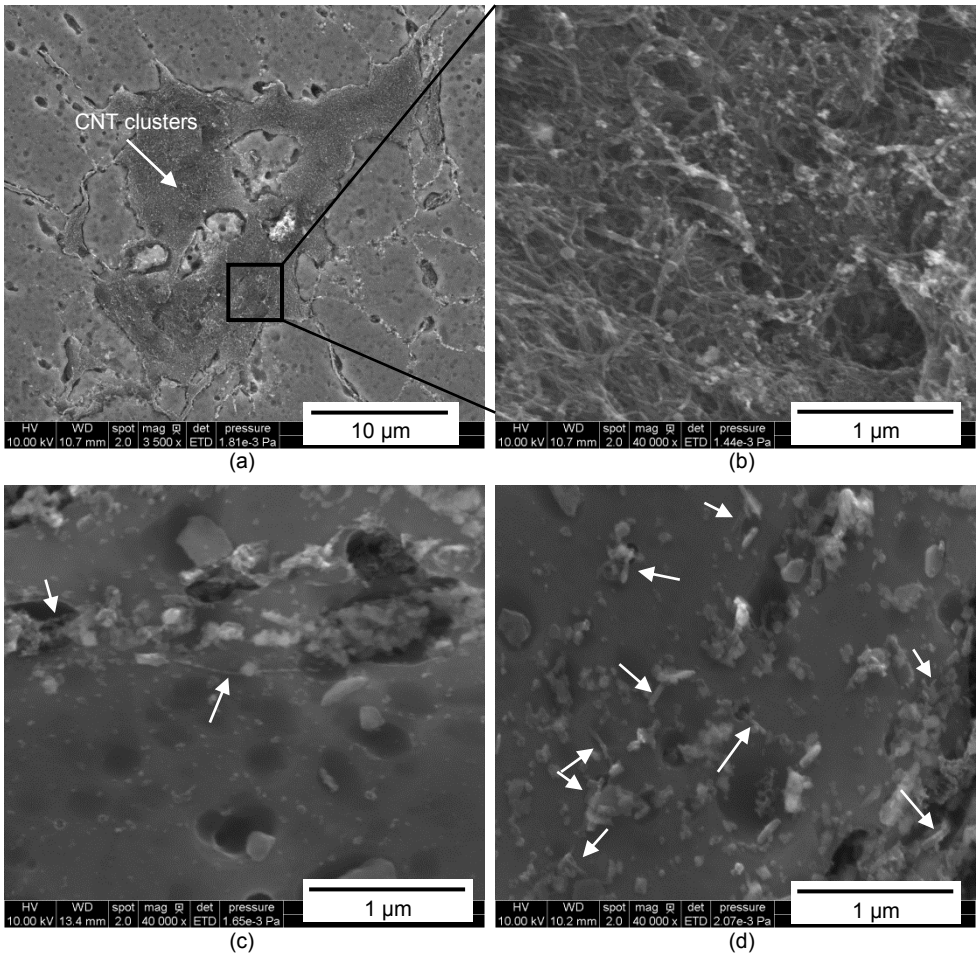

Fig. 6.8: SEM microstructure images (high magnification) of the Al6061-CNT samples with powders mechanically alloyed for (a) and (b) 0.5 hr, (c) 2 hrs and (d) 3 hrs. T=640°C.

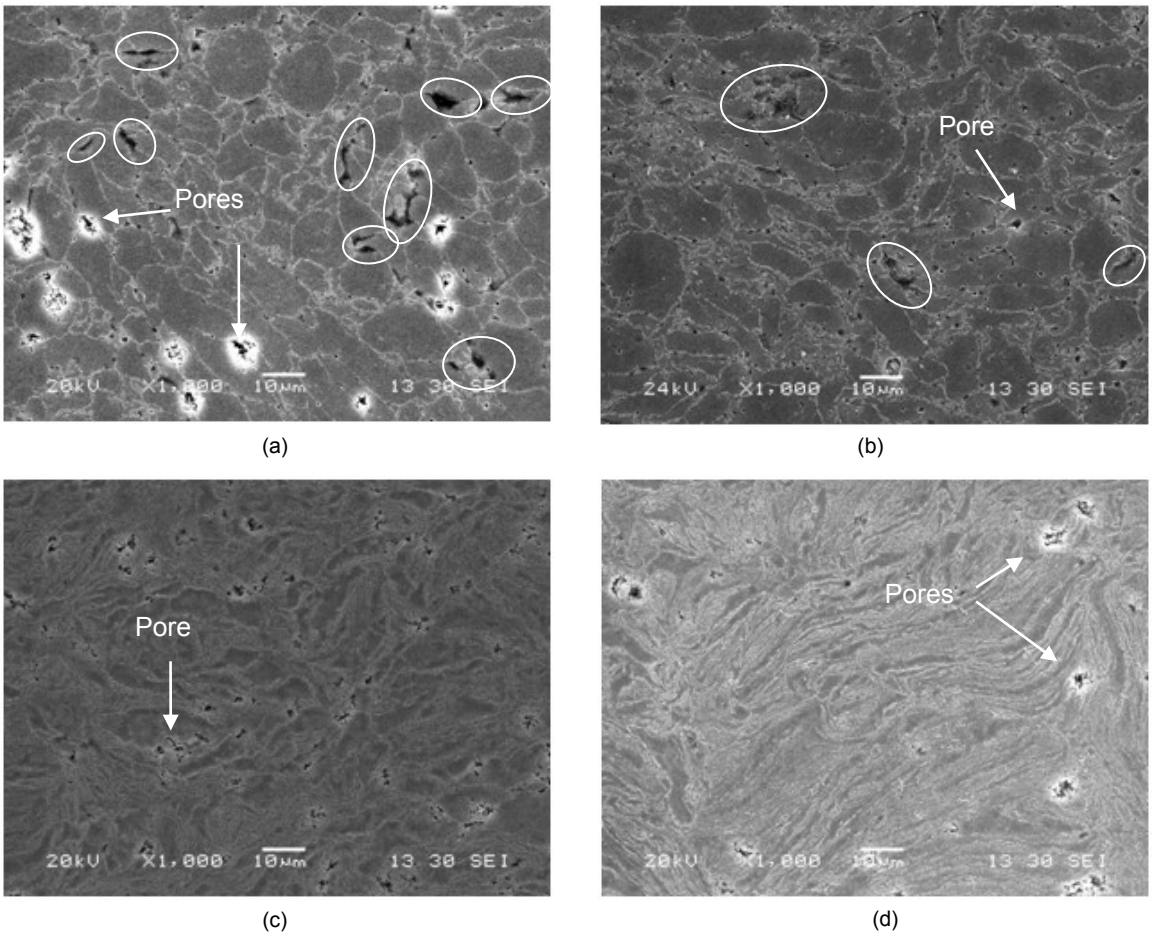

Fig. 6.9: SEM microstructure images (low magnification) of the Al6061-CNT composites with powders mechanically alloyed for (a) 0.5 hr, (b) 1 hr, (c) 2 hrs and (d) 3 hrs, respectively. T=640°C. Circles are CNT clusters, while the pores are revealed by deep etching process.

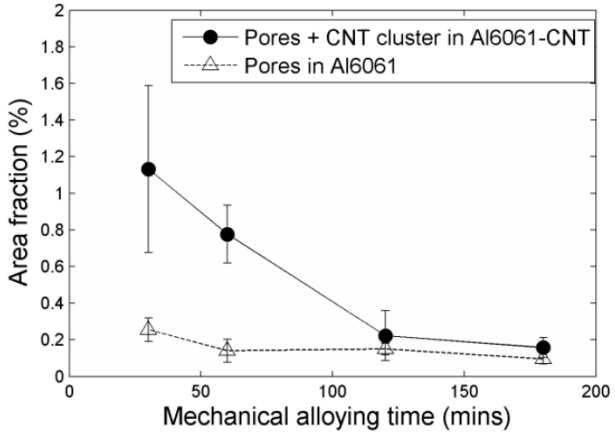

Fig. 6.10: Measured dark area fraction in Al6061-CNT and Al6061 samples at different mechanical alloying time. T=640°C

The microstructure and measured grain size of the samples are shown and summarized in Fig. 6.9 and Table 6.3, respectively. As shown in Fig. 6.9(a)−(d), the grains in the Al6061-CNT composite were severely deformed after three hours of mechanical alloying. The length (L) to width (W) aspect ratio of grains increased from 1.6 to 7.4, while the grain area decreased from 68 μm^2 to 52 μm^2 (see Table 6.3).

The effects of processing temperature on the microstructures of the polished and etched Al6061 and Al6061-CNT samples are shown in Fig. 6.11. Similar microstructures were observed for mechanically alloyed Al6061-CNT composite fabricated at different temperatures (Fig. 6.11).

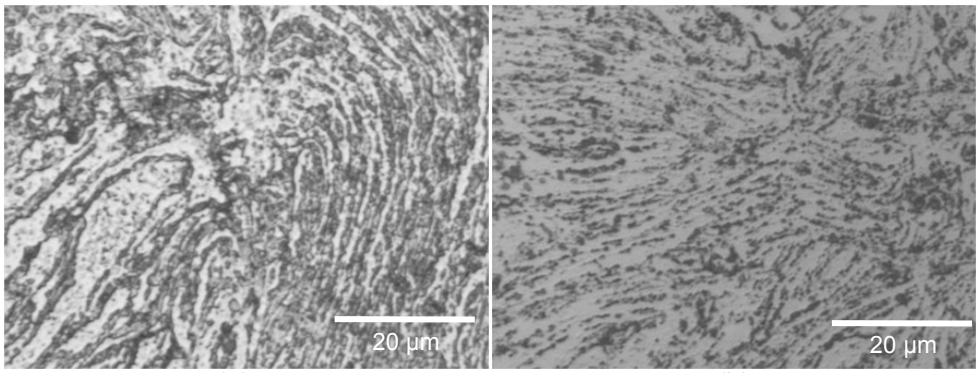

Fig. 6.11: Micrographs of the etched sample: (a) and (b) are optical images of the Al6061-CNT 600°C composite and Al6061-CNT 640°C composite, respectively. Powder mechanical alloying time: 3 hrs.

The measured relative densities of the composites processed with different temperature are listed in Table 6.4. Commercial software, ImageJ, was used to measure the porosity in the SEM images. For the Al6061-CNT composite fabricated at 620°C and 640°C, they achieved relative densities higher than 99.0%. Slightly lower density of 97.4% was obtained for the composite fabricated at 600°C because only a small amount of liquid-phase (7.5%) was available during the consolidation process.

Table 6.4: Measured densities at different consolidation temperatures

Condition	Relative Density (%)
Al6061 mechanically alloyed, 640°C	99.5
Al6061-CNT, 600°C	97.4
Al6061-CNT, 620°C	99.3
Al6061-CNT, 640°C	99.1

6.3.4 Hardness

The measured average hardnesses of the composites with different mechanical alloying time are summarized in Table 6.3. The hardness of the Al6061 and Al6061-CNT composite increased as the mechanical alloying time increased. For the Al6061 sample, the dispersion strengthening may be the main reason for the hardness increase (Benjamin 1980). For the Al6061-CNT composite, improved dispersion of CNTs by the mechanical alloying further increased the hardness. Therefore, the net hardness increase from CNT addition can be extracted by comparing the hardness of Al6061 sample and Al6061-CNT composite samples. The net percent hardness improvement between the two samples increased from 2% to 28% as the mechanical alloying time increased from 0.5 to 2 hours. When the powder was mechanically alloyed for three hours, the hardness net percent gain was 24.4%, which was lower than the sample with two hours of mechanical alloying. This may be due to the limited improvement of CNT dispersion and continuous CNT breakage beyond two hours of mechanical alloying.

The hardness of the fabricated Al6061 and Al6061-CNT composites with different processing temperature are shown in Fig. 6.12. When the operating temperature was 620°C, the hardness improvement of the Al6061-CNT composite over the Al6061 mechanical alloyed sample was the highest at 42.3%. The hardness of the Al6061-CNT composite for 600°C (83.3 HV) was close to that of Al6061-CNT composite synthesized at 620°C (87.5 HV). However, the hardness of Al6061-CNT composite fabricated at 640°C was much lower (76.5 HV). Several factors may have contributed to the lower hardness at 640°C. Higher temperature may result in more formation and precipitation of

oxidation, spinal and Al_4C_3. The prismatic dislocations loops may be punched out (Giannattasio, Senkader et al. 2004), lowing the strength of the composites. Another factor may be excessive formation of Al_4C_3 at elevated temperatures. The presence of a small amount of carbide at the interface of the CNT and matrix can improve the interfacial bonding (Ci, Ryu et al. 2006), but excessive carbide formation can result in overall degradation of the composite strength since the carbides have inferior properties compared with the CNTs.

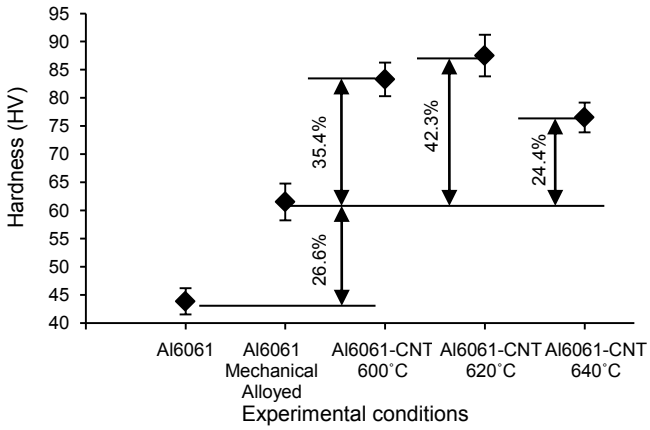

Fig. 6.12: Comparison of fabricated composite hardness with different processing temperature. Powders were mechanically alloyed for 3 hrs.

6.3.5 Bend Test

The flexural strengths and strains from the bend tests were calculated by Eqn. (6.3) and Eqn. (6.4). The bend test results for samples with different mechanical alloying time are shown in Fig. 6.13. The ductility of the Al6061 decreased as the mechanical alloying time increased, while the flexural strength of the Al6061 did not change with increasing mechanical alloying time (Fig. 6.13(a)). As shown in Fig. 6.13(b), the flexural strength

of the Al6061-CNT composite increased as the mechanical alloying time increased due to the improved CNT dispersion. The addition of CNTs also resulted in decrease of the ductility. When the mechanical alloying times were less than one hour, however, the flexural strengths of Al6061-CNT composites were lower than those of the Al6061. The agglomerated CNT network sites became fracture initiation points, which resulted in decrease of the flexural strength.

$$\sigma_f = 3PL/2bd^2 \tag{6.3}$$

$$\epsilon_f = \frac{6Dd}{L^2} \tag{6.4}$$

where σ_f and ϵ_f are the flexural stress (MPa) and flexural strain, respectively; P is the load (N); L is the support span (mm), b and d is the width and depth of the sample (mm), respectively; and D is the deflection of the center of the sample (mm).

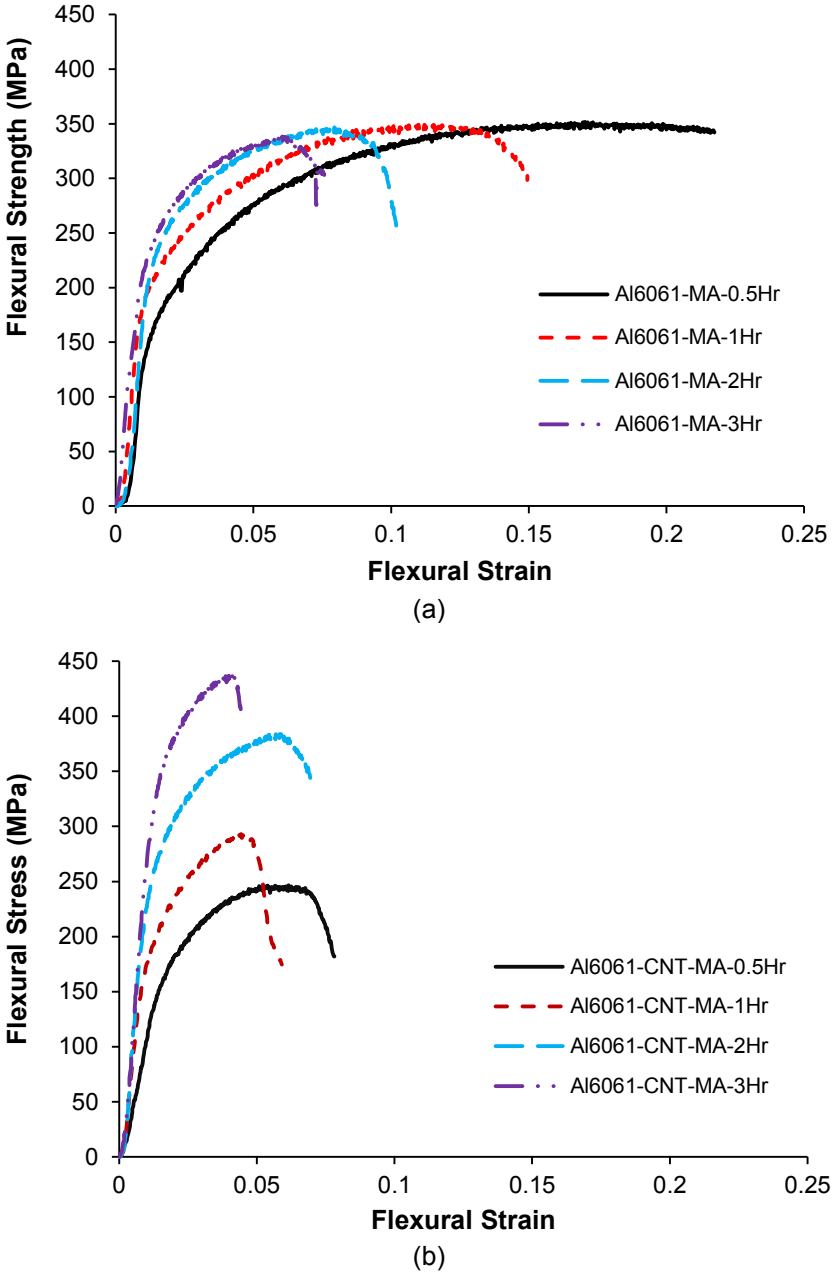

Fig. 6.13: Three point bending test results for the Al6061 and Al6061-CNT composites with different mechanical alloying time.

6.3.6 Fracture Surface

The fracture surfaces of the composites with different mechanical alloying time are shown in Fig. 6.14. The CNT clusters were observed on the fracture surfaces of

Al6061-CNT sample that had been mechanically alloyed for 0.5 hour (Fig. 6.14(b)). After three hours of mechanical alloying, the CNTs were well-dispersed, and single CNTs were found on the fracture surfaces (Fig. 6.14(d)). Ductile fracture surfaces were observed in the Al6061-CNT composite that have been mechanical alloyed for 0.5 hour (Fig. 6.14(a)). However, after three hours of mechanical alloying, fracture surfaces contained numerous flat regions (Fig. 6.14(c)).

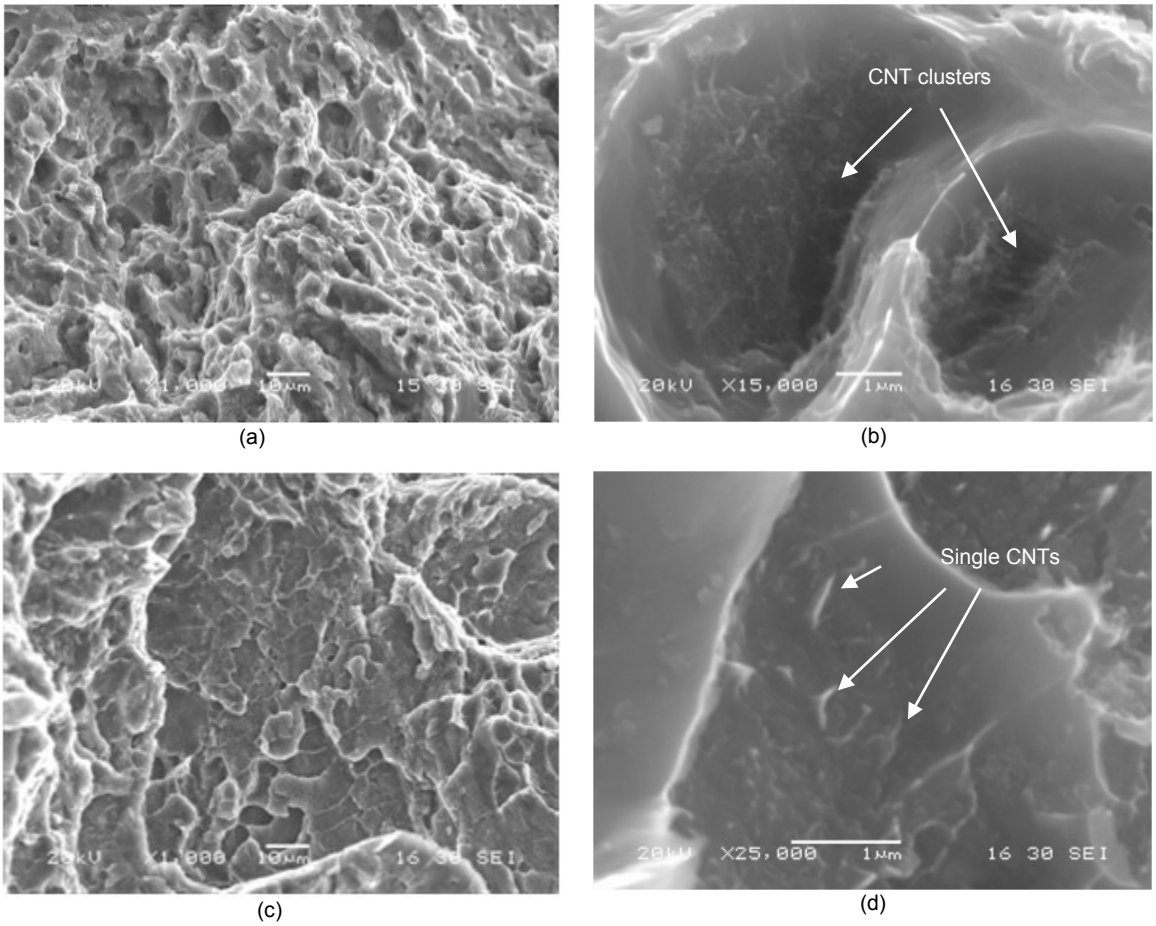

Fig. 6.14: Fracture surfaces of the samples: (a) and (b) are Al6061-CNT composite mechanically alloyed for 0.5 hr; (c) and (d) are Al6061-CNT composite mechanically alloyed for 3 hrs. T=640°C.

As shown in Fig. 6.15, layered fracture surfaces having flat regions were also observed for composite processed with different temperatures. The thicknesses of these regions in Fig. 6.15(a) and (b) were about 10 μm. As shown in Fig. 6.16, the thickness of mechanically alloyed particles, which had flat surfaces, was around 10 μm. This indicated that the observed layer in Fig. 6.15(b) corresponded to the mechanically alloyed Al6061-CNT particles, and the composite fractured through these particle boundaries. The flat areas were observed much more for Al6061-CNT composite processes at 600°C, and dispersed CNTs were found in these areas (see Fig. 6.15(c) and (d)). It confirmed the effectiveness of CNT dispersion by mechanical alloying, but the dispersed CNTs still remained close to the original particle surface rather than penetrating deep into the matrix particle.

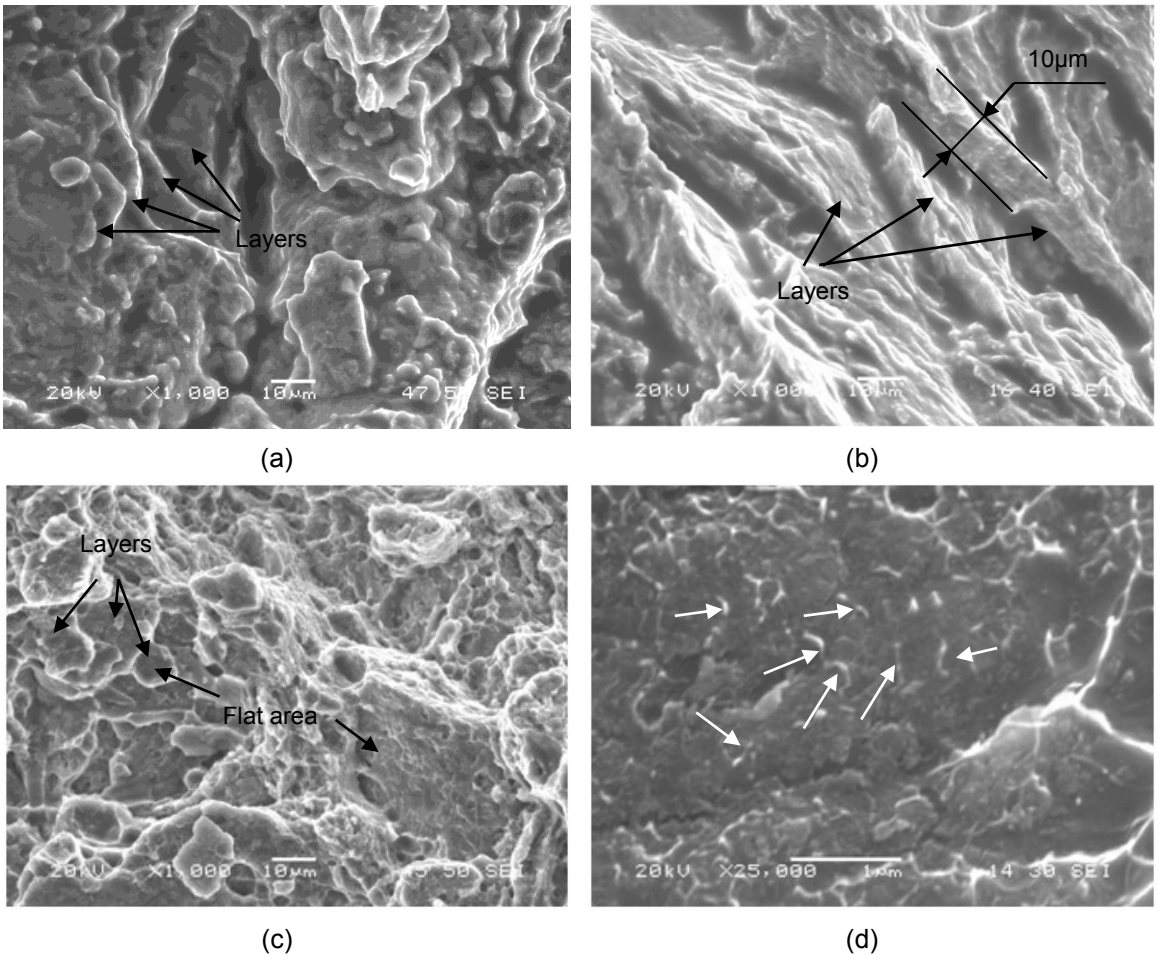

Fig. 6.15: SEM images of the fracture surfaces: (a) and (b) Al6061-CNT 620°C composite; and (c) and (d) Al6061-CNT 600°C composite. Powder mechanical alloying time: 3 hrs.

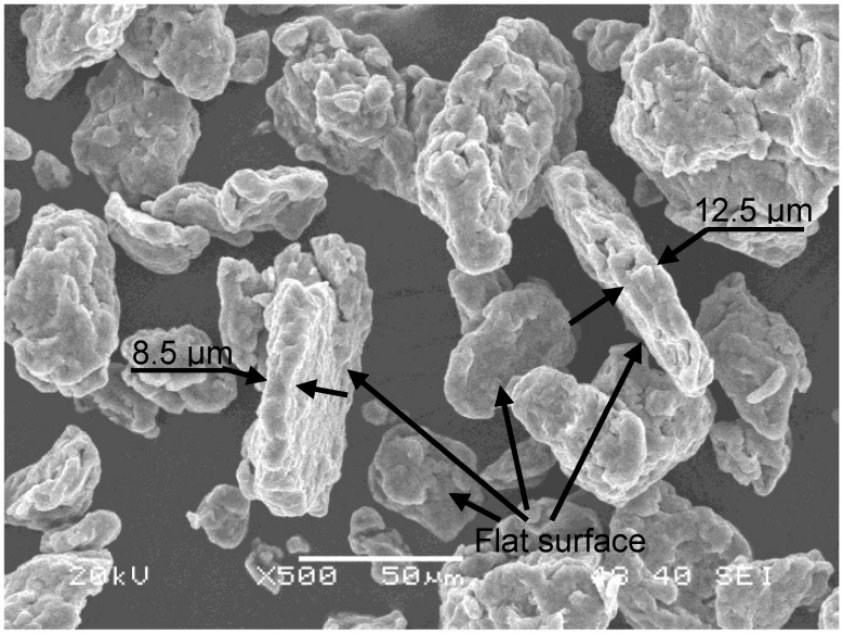

Fig. 6.16: Al6061-CNT powders mechanically alloyed for 3 hours.

6.3.7 Compositional Analysis

As shown in Fig. 6.17, the XRD pattern of Al6061-CNT composite showed the presence of spinel (Al_2MgO_4), aluminum carbide (Al_4C_3), carbon nanotubes, Mg_2Si, and aluminum. Aluminum oxide (Al_2O_3) may be present on the Al6061 particle surface or formed during the heating process. During the synthesis, the surface oxide layer is broken-down by applied pressure, while the Al_2O_3 is reduced by the reaction mechanism in Eqn. (6.5) (Lumley, Sercombe et al. 1999). Sreekumar et al. studied the thermodynamics and kinetics of the formation of Al_2O_3/ $MgAl_2O_4$/MgO in the Al-Mg-Si system (Sreekumar, Ravi et al. 2008). The results showed that for the Mg and Si levels in the Al6061, Al_2MgO_4 was preferred over either Al_2O_3 or MgO. Other studies also showed that at Mg levels less than 4%, the formation of spinel was favored (Mcleod 1990; Mcleod and Gabryel 1992; Lumley, Sercombe et al. 1999), while MgO was likely to

form at higher Mg levels (Levi, Abbaschian et al. 1978). The formation of Al_4C_3 was proved thermodynamically feasible by Bakshi et al. (Bakshi, Keshri et al. 2009). Some researchers indicated that limited formation of Al_4C_3 may improve the interface bonding between aluminum and CNT (Ci, Ryu et al. 2006).

$$4Al_2O_3 + 3Mg \rightarrow 4MgAl_2O_4 + 2Al \tag{6.5}$$

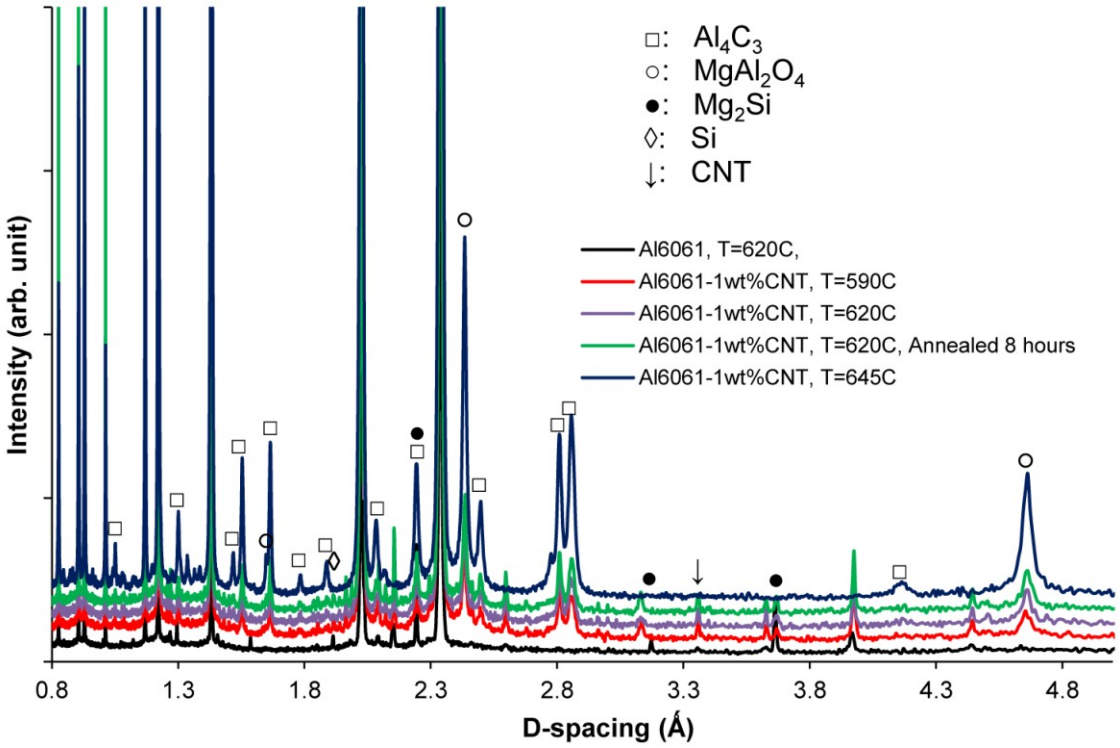

Fig. 6.17: XRD patterns of the Al6061 and Al6061-CNT composites. Data obtained with high energy X-ray diffraction in Argonne National Lab.

As shown in Fig. 6.17, there was limited oxide formation during the mechanical alloying of the Al6061-CNT powders. The formation of Al_4C_3 and spinel increased during the synthesis of Al6061-CNT composite as the temperature increased. At higher

temperature (T=645˚C) the CNT was depleted for the formation of carbides in the composites.

6.3.8 Prediction of the Material Strength

The strength of the material can be estimated with Eqn. (6.6) (Bakshi, Lahiri et al. 2010):

$$\sigma_c = V_f \sigma_f \frac{l}{2l_c} + V_m \sigma_m \tag{6.6}$$

where, V_f and V_m are the volume fractions of the carbon nanotube and matrix, respectively; σ_f and σ_m are strengths of the carbon nanotube and the matrix, respectively; l is the length of the carbon nanotube; and l_c is the critical length for the carbon nanotube. Two underlying assumptions of this equation are that the CNTs are fully dispersed in the composite and the bonding between the CNTs and the matrix is perfect. Thus, this equation will typically over-predict the strength of a composite. In this work, a modified equation was used:

$$\sigma_c = \alpha d V_f \sigma_f \frac{l}{2l_c} + V_m \sigma_m \tag{6.7}$$

where, two new parameters, the interfacial bonding coefficient (α) and the CNT dispersion parameter (d), were introduced. The α parameter is primarily affected by the interfacial bonding and reaction, which is difficult to measure; d ranges between 0 (no dispersion) and 1 (complete dispersion). When CNTs are agglomerated, the fibers add no strength to the overall composite strength. A value for d is estimated from Eqn. (6.8), where the difference of dark area fraction in Al6061-CNT composite and Al6061 without

CNTs is assumed to correlate to the CNT dispersion state in the composite. The following equation was used to predict CNT dispersion, *d*:

$$d = \frac{1}{ae^{-bt} + 1} \tag{6.8}$$

where, t is the mechanical alloying time; *a*=57.9 and *b*=0.054 are fitting parameters. The length of CNT was observed to decrease as mechanical alloying progressed. The CNT lengths were estimated to be 2.1, 1.7, 1.3, and 1.15 μm at mechanical alloying times of 0.5,1, 2, and 3 hours. The CNT lengths were calculated based on the measured surface CNT lengths and CNT dispersion as described in Chapter 5. Assuming that the yield strength (in MPa) of the material is about three times the hardness (in HV), predicted yield strength is shown in Fig. 6.18. The experimental data agreed with the predicted yield strength when an interfacial bonding coefficient of 0.58 was used.

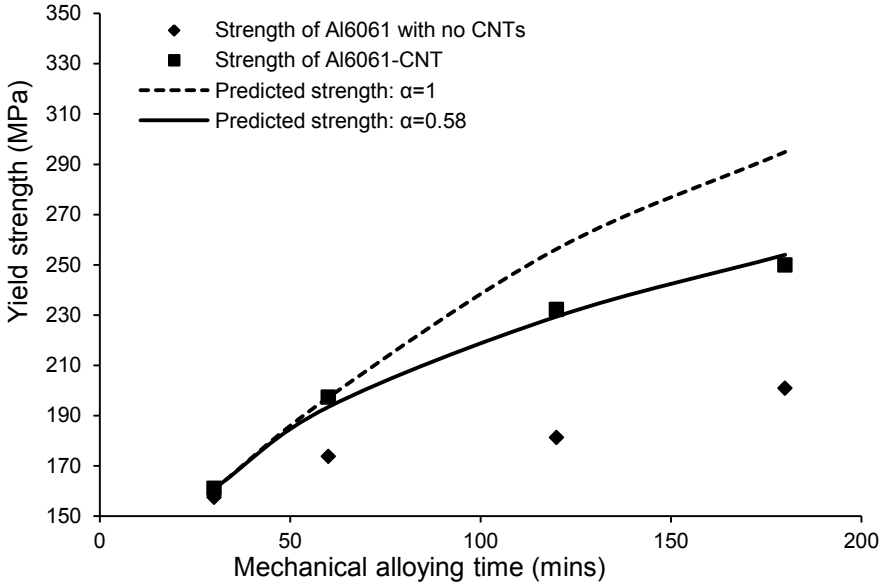

Fig. 6.18: Yield strength obtained with experiments and prediction for Al6061 with no CNT content and Al6061-CNT composite.

6.4 Conclusion

In this study, Al6061-1.0 wt.% CNT composite was successfully fabricated by SPP for the first time. Mechanical alloying was utilized to break down the CNT clusters. The effects of processing temperature during SPP and mechanical alloying time on the microstructure, hardness, fracture surface and the composition of the Al6061-CNT composite were investigated.

The mechanical alloying time determined the dispersion condition of CNTs and significantly affected the microstructures and mechanical properties of the Al6061-CNT composite. The length of CNTs decreased from more than 5 μm to less than 1 μm as the mechanical alloying time increased to three hours due to the high-energy ball mill used in

the experiment. Insufficient mechanical alloying time (0.5 hr) produced agglomerated CNTs on Al6061 particles. This resulted in non-uniform composite microstructure and inferior composite strength. As the mechanical alloying time increased (1 hr to 2 hrs), the CNT dispersion improved, and the resulting composite hardness increased. Adding 1.0 wt.% CNT increased the hardness by 28% when compared with the Al6061 composite without CNTs fabricated under the same condition. Most of the CNT agglomerations were broken down in the first 2 hours; longer mechanical alloying time (at 3 hrs) did not improve CNT dispersion and did not contribute to any further hardness improvement. The resultant grain structure showed severe deformation from the mechanical alloying process. Nevertheless, an improved dispersion of CNTs and continuous CNT breakage provided more reaction sites between the CNTs and liquidus matrix phase, forming Al_4C_3 and SiC during semi-solid powder processing. The ductility of the composite also decreased as the mechanical alloying time increased. Moreover, a modified shear lag model, which included the effects of interfacial bonding and CNT dispersion, predicted the overall Al6061-CNT composite strength accurately.

Due to cold working from mechanical alloying, pre-compaction of Al6061-CNT powder at 100 MPa resulted in the rearrangement of particles with relative density of 49.9%. Consolidation with liquid-phase existence at elevated temperatures yielded high relative density composites above 99%. The highest hardness of 87.5 HV was obtained from the Al6061-CNT composite consolidated at 620°C. At lower temperature of 600°C, relatively lower density and weaker bonding between the matrix phase and CNTs were obtained because of limited amount of the liquid-phase. The processing temperature also

influenced the fracture behavior of the composite. At 640°C, ductile fracture surfaces with dimples were observed; however, at lower temperatures fracture propagation was more prominent through the original particle boundaries.

The Al6061-CNT specimens were harder than the Al6061 reference samples; however, it is difficult to know how much of the additional hardness is attributable to the reinforcing effect of the CNTs and how much may result from the presence of Al_4C_3, SiC, spinel, and FeO. There are indications that an appreciable portion of the hardening effect may have resulted from the presence of the CNTs: (i) the SEM photos show abundant CNTs on the fracture surfaces, (ii) the aspect ratio of a CNT shortened to about 1 μm is still 20 to 50, which is presumably large enough to achieve the critical fiber length for optimal composite strengthening effect, and (iii) the large difference in coefficients of thermal expansion between CNTs and the Al6061 combined with the SSP would be expected to produce substantial concentrations of punch-out dislocations in the vicinity of the CNTs. All three of these factors would promote CNT strengthening in the composite.

CHAPTER 7 SUMMARY AND CONTRIBUTIONS

In this section, the conclusions and contributions of the work carried out were summarized. The major conclusions from each individual work were first introduced in section 7.1 and the contributions were discussed in section 7.2.

7.1 Summary

In this work, the deformation mechanism of the powders in the semi-solid state was understood and the potential of SPP on the synthesis of particle and fiber (nanotube) reinforced MMCs were investigated. The compaction behavior of powder compact with liquid-phase was analyzed, and the relative density during the compaction process was modeled. Densification behavior of Al6061-SiC powder mixture in the semi-solid state was investigated and effects of the SiC volume fraction and Al liquid fraction on the consolidation behavior were understood. Parametric study was carried out to investigate the particle reinforcement loading limit by SPP and to understand the compaction behavior of the ceramic particle-metal powder compact in the semi-solid state. In order to reveal the change of morphologies of CNTs during mechanical alloying, a mathematical model was developed to study the effects of welding and fracturing and CNT dispersion on the length change of CNTs. A set of experiments were performed to investigate the processing temperature and mechanical alloying time on the synthesis of CNT reinforced MMCs by SPP. The microstructures, mechanical properties, and compositions of the Al6061-CNT composites were examined and discussed.

The conclusions of individual section are summarized as the following:

7.1.1 Modeling of Semi-solid Powder Processing for a Closed-die Compaction

In this work, the compaction behavior of metallic powders in the semi-solid state was studied. The SPP at between 550°C and 630°C was modeled by Shima-Oyane model when liquid fraction is relative low (<20%). In the model, friction effects during the compaction process were considered. The relative density and the density distribution in the axial direction were modeled and verified with experimental results. The following conclusions can be drawn:

1. The relative density and density distribution in the axial direction during SPP were can be successfully modeled when liquid fraction was low (<20%) and the model matched the experimental results well.
2. Liquid fraction was able to affect the Poisson's ratio and therefore the parameters for the model have to be modified at different temperature.
3. When liquid fraction was high (>20%), the Shima-Oyane model was not applicable. Four stages during SPP with high liquid fraction, i.e., liquid material squeezing out, deforming of irregular solid arms, rupturing of trapped liquid and densification, were identified and discussed.
4. The normalized pressure-relative density curves for temperature between 550°C and 630°C merged into a single one because the major supporting phase is the solid and the deformation behavior of the solid-phase did not change significantly.

7.1.2 Densification behavior of Al6061 and SiC binary powder mixture in semi-solid state

The compaction behavior of Al6061-SiC powder mixture with 0-60 vol.% SiC reinforcement at elevated temperatures involving liquid-phase were investigated. The temperature ranged from 550°C to 660°C where the liquid fraction of Al6061 ranged from 0 to 100%. The reinforcement factor K_R and liquid factor K_L was studied and the following conclusions can be drawn:

1. The reinforcement factor K_R was significantly affected by the Al6061 liquid fraction and the SiC volume fraction. When the SiC volume fraction is low (<30%), the reinforcement factor K_R was similar across all liquid fraction range, while K_R was higher when f_L>10% was greater than 10%.
2. When the SiC volume fraction was high (>30%), the Al6061 liquid fraction determined the starting value of K_R.
3. The temperature factor K_T decreased as the liquid fraction of Al6061 increased and it is only dependent on the liquid fraction of Al6061 (temperature).

7.1.3 Fabrication of Al6061 Composite with High SiC Particle Loading by Semi-solid Powder Processing

In this work, high volume fraction SiC reinforced Al6061 composites were fabricated with SPP. The compaction mechanism of the Al6061-SiC composite was discussed and the SiC loading limit was also analyzed. The effects of the reinforcement particle size, matrix particle size, reinforcement loading volume and pressure on the

microstructure and mechanical properties were investigated. Based on the result of the parametric study, the following conclusions can be drawn.

1. SiC was the major phase that takes the compaction pressure. Al6061 phase was pressed to fill in the pores created by the SiC structure.
2. The maximum SiC loading in Al6061 can be estimated with data from SiC-only compaction tests. Higher SiC loading limit was obtained for larger SiC particles and higher compaction pressure.
3. The relative size of the initial Al6061 and SiC particles had significant effect on the microstructure, hardness and fracture surface of the composite. Non-uniform microstructure was obtained when the reinforcement particles were smaller than those of the matrix phase. This resulted in local variations in hardness and fracture surfaces. On the other hand, dense composite with smaller SiC particles resulted in higher hardness and uniform microstructures free of micro-cracks.

7.1.4 Mechanical Alloying of Carbon Nanotube and Al6061 Powder for Metal-CNT Composite

A mathematical model was developed to predict the overall CNT length and length distribution during mechanical alloying for the first time, while experiments were conducted to assist the prediction of overall CNT length. The effects of welding and fracturing of the CNTs and aluminum particles were better understood. The findings of this work can be concluded as the following:

1. The CNT length decreased significantly during mechanical alloying. Severe CNT length reduction occurred (from 4.24 μm to 1.69 μm) in the first several minutes due to the crushing of CNT agglomeration balls. After that, the length of CNTs decreased slowly to 1.16 μm.
2. The welding and fracturing of Al6061 particles and the dispersion of CNTs affected the overall CNT length. The model predicted that no further change occurred in the overall CNT length during time greater than one hour of mechanical alloying because most of the CNTs had already become embedded within the particles and were thus protected from further milling media impacts. A faster dispersion of CNTs and lower particle fracturing rate may help preserve the original CNTs.

7.1.5 Carbon Nanotube Reinforced Aluminum Composite Fabricated by Semi-solid Powder Processing

Al6061-1.0 wt.% CNT composite was fabricated by SPP in this work. Mechanical alloying was utilized to break down the CNT clusters. The effects of processing temperature during SPP and mechanical alloying time on the microstructure, hardness, fracture surface and the composition of the Al6061-CNT composite were investigated. Based on the parametric experimental work, we can draw the following conclusions:

1. The mechanical alloying time determined the dispersion condition of CNTs and significantly affected the microstructures and mechanical properties of the Al6061-CNT composite. Longer mechanical alloying time produced better

CNT dispersion and hence a more uniform composite microstructure and preferred composite strength.

2. The CNT agglomerates were mostly broken down in the first 2 hours and longer mechanical alloying time (at 3 hrs) did not improve CNT dispersion and did not contribute to any further hardness improvement. The resultant grain structure showed severe deformation from the mechanical alloying process.
3. An improved dispersion of CNTs and continuous CNT breakage provided more reaction sites between the CNTs and liquidus matrix phase, forming Al_4C_3 and SiC during semi-solid powder processing. The ductility of the composite also decreased as the mechanical alloying time increased.
4. A modified shear lag model, which included the effects of interfacial bonding and CNT dispersion, predicted the overall Al6061-CNT composite strength accurately.
5. The highest hardness of 87.5 HV was obtained from the Al6061-CNT composite consolidated at 620°C. At 600°C, relatively lower density and weaker bonding was observed between the matrix phase and CNTs, and the fracture propagation was more prominent through the original particle boundaries.

7.2 Scientific Contributions

Major scientific contributions of the dissertation may be summarized as the following:

1. The compaction behavior of metallic powder containing both solid and liquid-phases was modeled for the first time. The model was able to effectively capture the yielding of the semi-solid powder compact and accurately predict the relative density change during the compaction process with relatively low liquid fraction (<20%). The deformation mechanism of metal powder compact during SPP with high liquid fraction (>20%) was understood.
2. The densification behaviors of SiC reinforced Al6061 powder compact in semi-solid state was understood. The effects of volume fraction of SiC and Al6061 liquid fraction on the densification behavior were revealed.
3. The reinforcement loading limit of the Al6061-SiC composite was identified. High density composite with high SiC loading was successfully fabricated by SPP, and the effects of experimental parameters on the samples were revealed.
4. A mathematical model was developed to predict the overall CNT length during mechanical alloying and to understand the effects of welding and fraction and CNT dispersion on the morphologies of the CNTs.
5. CNT reinforced Al6061 composites were successfully fabricated with SPP. The effects of temperature and mechanical alloying time on the fabrication process as well as the final composite were studied. The mechanical property (hardness) of the composite was able to be predicted with a shear lag model.

7.3 Acknowledgements

I greatly appreciate the financial supports from National Science Foundation under grant number CMMI-1030120 and from Ames Laboratory of US Department of Energy under contract number DE-AC02-07CH11358.

BIBLIOGRAPHY

Backman, D. G. (1977). "Die thermal behavior in machine casting of partially solid high temperature alloys." *Metallurgical transactions. B, Process metallurgy*, **8**(3), pp. 471-477.

Bakshi, S. R., A. K. Keshri, et al. (2009). "Interface in carbon nanotube reinforced aluminum silicon composites: Thermodynamic analysis and experimental verification." *Journal of Alloys and Compounds*, **481**(1-2), pp. 207-213.

Bakshi, S. R., D. Lahiri, et al. (2010). "Carbon nanotube reinforced metal matrix composites - a review." *International Materials Reviews*, **55**(1), pp. 41-64.

BCC_Research (2009). *Metal matrix composites: the global market*.

Benjamin, J. S. (1980). "Mechanical Alloying." *Powder Metallurgy International*, **12**(1), pp. 43-43.

Benjamin, J. S. (1992). "Fundamentals of Mechanical Alloying." *Mechanical Alloying*, **88**, pp. 1-17.

Benjamin, J. S. and T. E. Volin (1974). "Mechanism of Mechanical Alloying." *Metallurgical Transactions*, **5**(8), pp. 1929-1934.

Bouvard, D. (1993). "Modelling the densification of powder composites by power law creep." *Acta Metallurgica Et Materialia*, **41**(5), pp. 1413-1420.

Brewin, P. R., O. Coube, et al. (2008). *Modelling of powder die compaction*. London, Springer.

Candan, E., H. Ahlatci, et al. (2001). "Abrasive wear behaviour of Al–SiC composites produced by pressure infiltration technique." *Wear*, **247**(2), pp. 133-138.

Cerit, A. A., M. B. Karamis, et al. (2008). "Effect of Reinforcement Particle Size and Volume Fraction on Wear Behaviour of Metal Matrix Composites." *Journal of the Balkan Tribological Association*, **14**(4), pp. 482-489.

Chawla, N., J. Jones, et al. (1998). "Effect of SiC volume fraction and particle size on the fatigue resistance of a 2080 Al/SiC p composite." *Metallurgical and Materials Transactions A*, **29**(11), pp. 2843-2854.

Chen, C. M., C. C. Yang, et al. (2004). "Thixocasting of hypereutectic Al-25Si-2.5Cu-1Mg-0.5Mn alloys using densified powder compacts." *Materials Science and Engineering A*, **366**(1), pp. 183-194.

Chen, C. M., C. C. Yang, et al. (2005a). "Dry sliding wear behaviors of Al-25Si-2.5Cu-1Mg alloys prepared by powder thixocasting." *Materials Science and Engineering A*, **397**(1-2), pp. 178-189.

Chen, C. M., C. C. Yang, et al. (2005b). "A novel method for net-shape forming of hypereutectic Al-Si alloys by thixocasting with powder preforms." *Journal of Materials Processing Technology*, **167**(1), pp. 103-109.

Cho, K.-M., I.-D. Choi, et al. (2004). "Thermal properties and fracture behavior of compositionally graded Al-SiCp composites." *Materials Science Forum*, **449-452**(1), pp. 621-624.

Ci, L. J., Z. Y. Ryu, et al. (2006). "Investigation of the interfacial reaction between multi-walled carbon nanotubes and aluminum." *Acta Materialia*, **54**(20), pp. 5367-5375.

Cooper, A. R. and L. E. Eaton (1962). "Compaction Behavior of Several Ceramic Powders." *Journal of the American Ceramic Society*, **45**(3), pp. 97-101.

Corbin, S. F. (1999). "Functionally graded metal/ceramic composites by tape casting, lamination and infiltration." *Materials science & engineering. A, Structural materials*, **262**(1), pp. 192-203.

Davis, R. M., B. Mcdermott, et al. (1988). "Mechanical Alloying of Brittle Materials." *Metallurgical Transactions a-Physical Metallurgy and Materials Science*, **19**(12), pp. 2867-2874.

Deng, C. F., D. Z. Wang, et al. (2007). "Processing and properties of carbon nanotubes reinforced aluminum composites." *Materials Science and Engineering a-Structural Materials Properties Microstructure and Processing*, **444**(1-2), pp. 138-145.

Deng, C. F., X. X. Zhang, et al. (2007). "Preparation and characterization of carbon nanotubes/aluminum matrix composites." *Materials Letters*, **61**(8-9), pp. 1725-1728.

Denny, P. J. (2002). "Compaction equations: a comparison of the Heckel and Kawakita equations." *Powder Technology*, **127**(2), pp. 162-172.

El Wakil, S. D. (1992). "Extrusion of P/M composites in the semi-solid state." *International Journal of Powder Metallurgy*, **28**(2), pp. 175-182.

Esawi, A. and K. Morsi (2007). "Dispersion of carbon nanotubes (CNTs) in aluminum powder." *Composites Part A Applied Science and Manufacturing*, **38**(2), pp. 646-650.

Everitt, B. and D. J. Hand (1981). *Finite mixture distributions*, Chapman and Hall.

Fan, T. (1998). "The interfacial reaction characteristics in SiC/Al composite above liquidus during remelting." *Materials science and engineering B*, **257**(2), pp. 281.

Fleck, N. A., L. T. Kuhn, et al. (1992). "Yielding of Metal-Powder Bonded by Isolated Contacts." *Journal of the Mechanics and Physics of Solids*, **40**(5), pp. 1139-1162.

Fogagnolo, J. B., M. H. Robert, et al. (2006). "Mechanically alloyed AlN particle-reinforced Al-6061 matrix composites: Powder processing, consolidation and mechanical strength and hardness of the as-extruded materials." *Materials Science and Engineering a-Structural Materials Properties Microstructure and Processing*, **426**(1-2), pp. 85-94.

Fuentes, J. J., J. A. Rodriguez, et al. (2003). "Effect of Mg as sintering additive on the consolidation of mechanically alloyed Al powder." *Thermec'2003, Pts 1-5*, **426-4**, pp. 4331-4336.

Giannattasio, A., S. Senkader, et al. (2004). "The role of prismatic dislocation loops in the generation of glide dislocations in Cz-silicon." *Computational Materials Science*, **30**(1-2), pp. 131-136.

Gunasekera, J. S. (1993). "Development of a Constitutive Model for Mushy (Semisolid) Materials." *Proceedings of the Second International Conference on the Semi-Solid Processing of Alloys and Composites*, pp. 211-222.

Gunasekera, J. S. and Z. Z. Zhou (1997). "Mechanics of semi-solid material." *Epd Congress 1997*, pp. 733-743.

Guo, M. L. T. and C. Y. A. Tsao (2000). "Tribological behavior of self-lubricating aluminium/SiC/graphite hybrid composites synthesized by the semi-solid powder-densification method." *Composites Science and Technology*, **60**(1), pp. 65-74.

Hafizpour, H. R. (2008). "Investigation on compressibility of Al-SiC composite powders." *Powder Metallurgy*, **51**(3), pp. 217-223.

Hamilton, R. W., Z. Zhu, et al. (2003). "Direct semi-solid forming of a powder SiC-A1 PMMC: Flow analysis." *Composites Part A: Applied Science and Manufacturing*, **34**(4), pp. 333-339.

Hatch, J. E. (1984). *Aluminum: Properties and physical metallurgy*. Metals Park, Ohio, American Society for Metals.

He, C. N., N. Q. Zhao, et al. (2007). "An approach to obtaining homogeneously dispersed carbon nanotubes in Al powders for preparing reinforced Al-matrix composites." *Advanced Materials*, **19**(8), pp. 1128-1132.

Ibrahim, I. A., F. A. Mohamed, et al. (1991). "Particulate reinforced metal matrix composites — a review." *Journal of Materials Science*, **26**(5), pp. 1137-1156.

Iijima, S. (1991). "Helical microtubules of graphitic carbon." *Nature*, **354**(6348), pp. 56-56.

Ilegbusi, O. J. and M. W. Ballas (1999). "A hybrid constitutive model for semi-solid alloy slurries." *Journal of Materials Processing & Manufacturing Science*, **8**(1), pp. 18-33.

Jeng, S.-C. and S.-W. Chen (1997). "The solidification characteristics of 6061 and A356 aluminum alloys and their ceramic particle-reinforced composites." *Acta Materialia*, **45**(12), pp. 4887-4899.

Jeong, Y. G., M. H. Seo, et al. (2005). "Mechanical modelling of carbon nanotube reinforced metal matrix composites." *Metastable, Mechanically Alloyed and Nanocrystalline Materials*, **24-25**, pp. 383-386.

Kaczmar, J. W., K. Pietrzak, et al. (2000). "The production and application of metal matrix composite materials." *Journal of Materials Processing Technology*, **106**(1-3), pp. 58-67.

Kainer, K. U., Ed. (2006). *Metal Matrix Composites. Custom-made Materials for Automotive and Aerospace Engineering*. Weinheim, WILEY.

Kang, C. G. and H. K. Jung (1999). "Finite element analysis with deformation behavior modeling of globular microstructure in forming process of semi-solid materials." *International Journal of Mechanical Sciences*, **41**(12), pp. 1423-1445.

Kawasaki, A. (1997). "Concept and P/M fabrication of functionally gradient materials." *Ceramics international*, **23**(1), pp. 73-83.

Kim, G.-Y., M. Koc, et al. (2007). "Modeling of the semi-solid material behavior and analysis of micro-/mesoscale feature forming." *Journal of Manufacturing Science and Engineering, Transactions of the ASME*, **129**(2), pp. 237-245.

Kim, G.-Y., J. Ni, et al. (2007). "An experimental investigation on semi-solid forming of micro/meso-scale features." *Journal of Manufacturing Science and Engineering, Transactions of the ASME*, **129**(2), pp. 246-251.

Kim, K. T., J. H. Cho, et al. (2000). "Cold Compaction of Composite Powders." *Journal of Engineering Materials and Technology*, **122**(1), pp. 119-128.

Kim, W. Y., C. G. Kang, et al. (2007). "The effect of the solid fraction on rheological behavior of wrought aluminum alloys in incremental compression experiments with a closed die." *Materials Science and Engineering: A*, **447**(1-2), pp. 1-10.

Koch, C. C. (1989). "Materials Synthesis by Mechanical Alloying." *Annual Review of Materials Science*, **19**(1), pp. 121-143.

Kouzeli, M., L. Weber, et al. (2001). "Influence of damage on the tensile behaviour of pure aluminium reinforced with ⩾ 40 vol. pct alumina particles." *Acta Materialia*, **49**(18), pp. 3699-3709.

Kumar, P., C. Martin, et al. (1993). "Shear rate thickening flow behavior of semisolid slurries." *Metallurgical and Materials Transactions A*, **24**(5), pp. 1107-1116.

Kumar, P., C. L. Martin, et al. (1994). "Constitutive Modeling and Characterization of the Flow Behavior of Semisolid Metal Alloy Slurries .1. The Flow Response." *Acta Metallurgica Et Materialia*, **42**(11), pp. 3595-3602.

Kwon, H., M. Estili, et al. (2009). "Combination of hot extrusion and spark plasma sintering for producing carbon nanotube reinforced aluminum matrix composites." *Carbon*, **47**(3), pp. 570-577.

Lange, F. F., L. Atteraas, et al. (1991). "Deformation consolidation of metal powders containing steel inclusions." *Acta Metallurgica Et Materialia*, **39**(2), pp. 209-219.

Lee, H. S. and S. H. Hong (2003). "Pressure infiltration casting process and thermophysical properties of high volume fraction SiC p / Al metal matrix composites." *Materials Science and Technology*, **19**(8), pp. 1057-1064.

Lee, H. S., K. Y. Jeon, et al. (2000). "Fabrication process and thermal properties of SiCp/Al metal matrix composites for electronic packaging applications." *Journal of Materials Science*, **35**(24), pp. 6231-6236.

Lee, J. C. (1997). "Effect of various processing methods on the interfacial reactions in SiCp/2024 Al composites." *Acta Materialia*, **45**(12), pp. 5303.

Lee, S. C. and K. T. Kim (2002). "Densification behavior of aluminum alloy powder under cold compaction." *International Journal of Mechanical Sciences*, **44**(7), pp. 1295-1308.

Levi, C. G., G. J. Abbaschian, et al. (1978). "Interface Interactions during Fabrication of Aluminum Alloy-Alumina Fiber Composites." *Metallurgical Transactions a-Physical Metallurgy and Materials Science*, **9**(5), pp. 697-711.

Li, H. Q., A. Misra, et al. (2009). "Processing and characterization of nanostructured Cu-carbon nanotube composites." *Materials Science and Engineering a-Structural Materials Properties Microstructure and Processing*, **523**(1-2), pp. 60-64.

Liao, J.-z., M.-J. Tan, et al. "Spark plasma sintered multi-wall carbon nanotube reinforced aluminum matrix composites." *Materials & Design*, **In Press, Corrected Proof**.

Lim, D. K., T. Shibayanagi, et al. (2009). "Synthesis of multi-walled CNT reinforced aluminium alloy composite via friction stir processing." *Materials Science and Engineering A*, **507**(1-2), pp. 194-199.

Lin, C. Y. (1999). "Production of silicon carbide Al 2124 alloy functionally graded materials by mechanical powder metallurgy technique." *Powder metallurgy*, **42**(1), pp. 29-33.

Lindroos, V. K. and M. J. Talvitie (1995). "Recent advances in metal matrix composites." *Journal of Materials Processing Technology*, **53**(1-2), pp. 273-284.

Lou, B. Y., J. C. Huang, et al. (2002). "Flow behaviour of aluminium-based materials at ultrahigh temperatures in the presence of a liquid phase." *Materials Transactions*, **43**(3), pp. 501-509.

Lumley, R., T. Sercombe, et al. (1999). "Surface oxide and the role of magnesium during the sintering of aluminum." *Metallurgical and Materials Transactions A*, **30**(2), pp. 457-463.

Luo, S.-J., Y.-S. Cheng, et al. (2006). "Pseudo-semi-solid thixoforging of cup shell with Al/Al2O3." *Transactions of Nonferrous Metals Society of China (English Edition)*, **16**(4), pp. 772-775.

Luo, S., Y. Cheng, et al. (2005). "Ceramics matrix composites thixoforming in pseudo-semi-solid state and the preliminary experimental study." *Chinese Journal of Materials Research*, **19**(1), pp. 107-112.

Martin, C. L., O. Lame, et al. (2000). "Cohesion and dilatation of powder compacts containing hard phase particles under highly deviatoric stress states." *Mechanics of Materials*, **32**(7), pp. 405-421.

Maurice, D. and T. H. Courtney (1994). "Modeling of Mechanical Alloying .1. Deformation, Coalescence, and Fragmentation Mechanisms." *Metallurgical and Materials Transactions a-Physical Metallurgy and Materials Science*, **25**(1), pp. 147-158.

Maurice, D. and T. H. Courtney (1995a). "Modeling of Mechanical Alloying .2. Development of Computational Modeling Programs." *Metallurgical and Materials Transactions a-Physical Metallurgy and Materials Science*, **26**(9), pp. 2431-2435.

Maurice, D. and T. H. Courtney (1995b). "Modeling of Mechanical Alloying .3. Applications of Computational Programs." *Metallurgical and Materials Transactions a-Physical Metallurgy and Materials Science*, **26**(9), pp. 2437-2444.

Mcleod, A. D. (1990). "Kinetics of the Growth of Spinel, Mgal2o4, in Alumina-Containing Aluminum-Magnesium Alloy Matrix Composites." *Fabrication of Particulates Reinforced Metal Composites*, pp. 17-21.

Mcleod, A. D. and C. M. Gabryel (1992). "Kinetics of the Growth of Spinel, Mgal2o4, on Alumina Particulate in Aluminum-Alloys Containing Magnesium." *Metallurgical Transactions a-Physical Metallurgy and Materials Science*, **23**(4), pp. 1279-1283.

Miserez, A., R. Muller, et al. (2004). "Particle reinforced metals of high ceramic content." *Materials Science and Engineering a-Structural Materials Properties Microstructure and Processing*, **387-89**, pp. 822-831.

Montanari, R., V. Tagliaferri, et al. (2009). *Metal matrix composite: structure and technologies*.

Morsi, K. and A. Esawi (2007). "Effect of mechanical alloying time and carbon nanotube (CNT) content on the evolution of aluminum (Al)–CNT composite powders." *Journal of Materials Science*, **42**(13), pp. 4954-4959.

Morsi, K., A. M. K. Esawi, et al. (2010). "Spark plasma extrusion (SPE) of ball-milled aluminum and carbon nanotube reinforced aluminum composite powders." *Composites Part a-Applied Science and Manufacturing*, **41**(2), pp. 322-326.

Noguchi, T., A. Magario, et al. (2004). "Carbon nanotube/aluminium composites with uniform dispersion." *Materials Transactions*, **45**(2), pp. 602-604.

Panelli, R. and F. Ambrozio Filho (2001). "A study of a new phenomenological compacting equation." *Powder Technology*, **114**(1-3), pp. 255-261.

Pech-Canul, M. I. (2002). "Effect of processing parameters on the production of bilayer-graded Al/SiC_p composites by pressureless infiltration." *Materials letters*, **56**(4), pp. 460-464.

Pech-Canul, M. I., E. E. Parras-Medecigo, et al. (2002). *Effect of processing parameters on the formation of composite-composite interfaces in bilayer Al/SiCp composites*. Conference Proceedings from Materials Solutions 2002**:** 203-208.

Perez-Bustamante, R., C. D. Gomez-Esparz, et al. (2009). "Microstructural and mechanical characterization of Al-MWCNT composites produced by mechanical milling." *Materials Science and Engineering a-Structural Materials Properties Microstructure and Processing*, **502**(1-2), pp. 159-163.

Pham, Q., S. C. Yoon, et al. (2007). "Multi-scale modelling scheme for carbon nanotube reinforced metal matrix composites." *Mechanical Behavior of Materials X, Pts 1and 2*, **345-346**, pp. 1261-1264.

Poirier, D., R. Gauvin, et al. (2009). "Structural characterization of a mechanically milled carbon nanotube/aluminum mixture." *Composites Part a-Applied Science and Manufacturing*, **40**(9), pp. 1482-1489.

Prater, W. L. (2006). "Comparison of ceramic material effects on the flexural Weibull statistics and fracture of high volume fraction particle reinforced aluminum." *Materials Science and Engineering a-Structural Materials Properties Microstructure and Processing*, **420**(1-2), pp. 187-198.

Qin, S., C. Chen, et al. (1999). "The effect of particle shape on ductility of SiCp reinforced 6061 Al matrix composites." *Materials Science and Engineering A*, **272**, pp. 363-370.

Quang, P., Y. G. Jeong, et al. (2007). "Consolidation of 1 vol. % carbon nanotube reinforced metal matrix nanocomposites via equal channel angular pressing." *Journal of Materials Processing Technology*, **187**, pp. 318-320.

Ramakrishnan, N. (1996). "An analytical study on strengthening of particulate reinforced metal matrix composites." *Acta Materialia*, **44**(1), pp. 69-77.

Shima, S. and M. Oyane (1976). "Plasticity Theory for Porous Metals." *International Journal of Mechanical Sciences*, **18**(6), pp. 285-291.

Song, D. H., Y. H. Park, et al. (2007). "Thermomechanical properties of functionally graded Al-SiCp composites." *Materials Science Forum*, **534-536**, pp. 1565-1568.

Spencer, D., R. Mehrabian, et al. (1972). "Rheological behavior of Sn-15 pct Pb in the crystallization range." *Metallurgical and Materials Transactions B*, **3**(7), pp. 1925-1932.

Sreekumar, V. M., K. R. Ravi, et al. (2008). "Thermodynamics and kinetics of the formation of Al2O3/MgAl2O4/MgO in al-silica metal matrix composite." *Metallurgical and Materials Transactions a-Physical Metallurgy and Materials Science*, **39A**(4), pp. 919-933.

Sridhar, I. and N. A. Fleck (2000). "Yield behaviour of cold compacted composite powders." *Acta Materialia*, **48**(13), pp. 3341-3352.

Steinhoff, K., U. Weidig, et al. (2004). "Micro semi-solid manufacturing - A new technological approach towards miniaturisation." *Steel Research International*, **75**(8-9), pp. 611-619.

Storåkers, B., N. A. Fleck, et al. (1999). "The viscoplastic compaction of composite powders." *Journal of the Mechanics and Physics of Solids*, **47**(4), pp. 785-815.

Svoboda, J., H. Riedel, et al. (1996). "A model for liquid phase sintering." *Acta Materialia*, **44**(8), pp. 3215-3226.

Tham, L. M., M. Gupta, et al. (2001). "Effect of limited matrix-reinforcement interfacial reaction on enhancing the mechanical properties of aluminium-silicon carbide composites." *Acta Materialia*, **49**(16), pp. 3243-3253.

Wang, L., H. Choi, et al. (2009). "Mechanical alloying of multi-walled carbon nanotubes and aluminium powders for the preparation of carbon/metal composites." *Carbon*, **47**(15), pp. 3427-3433.

Watari, F. (1997). "Fabrication and properties of functionally graded dental implant." *Composites. Part B, Engineering*, **28**(1), pp. 5-11.

Wen, C. E. (2001). "Fabrication of TiAl by blended elemental powder semisolid forming." *Journal of Materials Science*, **36**(7), pp. 1741-1745.

Wildgoose, G. G., C. E. Banks, et al. (2006). "Chemically Modified Carbon Nanotubes for Use in Electroanalysis." *Microchimica Acta*, **152**(3), pp. 187-214.

Wu, Y. (2009). Fabrication of graded structures in SiC-reinforced metal matrix by semisolid powder processing. *Proceedings of the ASME International Manufacturing Science and Engineering Conference 2009*.

Wu, Y. and G.-Y. Kim (2011a). "Carbon nanotube reinforced aluminum composite fabricated by semi-solid powder processing." *Journal of Materials Processing Technology*, **211**(8), pp. 1341-1347.

Wu, Y. and G.-Y. Kim (2011b). "Compaction behavior of Al6061 powder in the semi-solid state." *Powder Technology*, **214**(2), pp. 252-258.

Wu, Y., G.-Y. Kim, et al. (2010a). "Fabrication of Al6061 composite with high SiC particle loading by semi-solid powder processing." *Acta Materialia*, **58**(13), pp. 4389-4405.

Wu, Y., G.-Y. Kim, et al. (2010b). "Experimental Study on Viscosity and Phase Segregation of Al--Si Powders in Microsemisolid Powder Forming." *Journal of Manufacturing Science and Engineering, Transactions of the ASME*, **132**(1), pp. 011003-011007.

Wu, Y., G.-Y. Kim, et al. (2011). "Effects of mechanical alloying on the Al6061-CNT composite fabricated by semi-solid powder processing." *Materials Science and Engineering A*, **Submitted**.

Xie, C. L., M. Hailat, et al. (2007). "Development of short fiber-reinforced NiTi/Al6061 composite." *Journal of Engineering Materials and Technology-Transactions of the Asme*, **129**(1), pp. 69-76.

Xu, C. L., B. Q. Wei, et al. (1999). "Fabrication of aluminum-carbon nanotube composites and their electrical properties." *Carbon*, **37**(5), pp. 855-858.

Yasue, K. (2000). "Elemental blended powders semisolid forming of Ti-Al based alloys." *Journal of Materials Science*, **35**(23), pp. 5927-5932.

Young, R. M. K. and T. W. Clyne (1986a). "A powder-based approach to semisolid processing of metals for fabrication of die-castings and composites." *Journal of Materials Science*, **21**(3), pp. 1057-1069.

Young, R. M. K. and T. W. Clyne (1986b). "A powder mixing and preheating route to slurry production for semisolid diecasting." *Powder metallurgy*, **29**(3), pp. 195-199.

Zhang, L., X. H. Qu, et al. (2008). "Thermo-physical and mechanical properties of high volume fraction SiCp/Cu composites prepared by pressureless infiltration." *Materials Science and Engineering a-Structural Materials Properties Microstructure and Processing*, **489**(1-2), pp. 285-293.

Zhong, R., H. Cong, et al. (2003). "Fabrication of nano-Al based composites reinforced by single-walled carbon nanotubes." *Carbon*, **41**(4), pp. 848-851.

Zhou, S. M., X. B. Zhang, et al. (2007). "Fabrication and tribological properties of carbon nanotubes reinforced Al composites prepared by pressureless infiltration technique." *Composites Part a-Applied Science and Manufacturing*, **38**(2), pp. 301-306.

Zu, L. and S. Luo (2001). "Study on the powder mixing and semi-solid extrusion forming process of SiCp/2024Al composites." *Journal of Materials Processing Technology*, **114**(3), pp. 189-193.